Role of channels in the O_2 permeability of murine red blood cells
I. Stopped-flow and hematological studies

Pan Zhao[1]
Fraser J. Moss[1‡]
Rossana Occhipinti[1‡]
R. Ryan Geyer[1‡]
Dale E. Huffman[1]
Howard J Meyerson[2]
Walter F Boron[1,3]

[1]Department of Physiology & Biophysics and [2]Department of Pathology
Case Western Reserve University School of Medicine
Cleveland, OH 44106
[3]Department of Medicine and Department of Biochemistry
Case Western Reserve University School of Medicine

[‡]These three authors made equal contributions to the work

Journal: *Journal of Physiology, Cell physiology*

Running title: *RBC O_2 permeability: Physiology*

Keywords: *Aquaporin 1, Rhesus (Rh) complex, genetic deletion, pCMBS (p-chloromercuribenzenesulfonate), DIDS (4,4'-diisothiocyanatostilbene-2,2'-disulfonate)*

Correspondence and proofs:

Pan Zhao MD, PhD
Department of Physiology & Biophysics
Case Western Reserve University
School of Medicine
10900 Euclid Avenue
Cleveland, OH 44106-4970
Phone: (216) 368 3400
Fax: (219) 368 5586
E-mail: pan.zhao2@case.edu

Walter F Boron, MD, PhD
Department of Physiology and Biophysics
Case Western Reserve University
School of Medicine
10900 Euclid Avenue
Cleveland, OH 44106-4970
Phone: (216) 368 3400
Fax: (216) 368 5586
E-mail Walter.Boron@case.edu

Key Points

- Some have held that red-blood-cell (RBC) membranes have a finite O_2 permeability, governed by O_2 solubility in membrane lipids; others, that membranes offer no resistance whatsoever to O_2 diffusion.
- The present interdisciplinary study comprises three papers. This first paper describes stopped-flow absorbance spectroscopy in which we examine the rate constant of O_2 offloading from intact RBCs (k_{HbO_2}) from wild-type (WT) mice or those lacking AQP1 and/or RhAG, sometimes treated with p-chloromercuribenzenesulfonate (pCMBS) or 4,4'-diisothiocyanatostilbene-2,2'-disulfonate (DIDS).
- The second paper describes RBC morphometry and membrane proteomics. The third introduces a mathematical reaction-diffusion model that generates simulations comporting with physiological data.
- This first paper shows that pCMBS or DIDS treatments, or deletion of AQP1 and/or RhAG, or combinations thereof, substantially reduce k_{HbO_2}.
- The three papers show that WT RBC membranes offer considerable resistance to O_2 diffusion. AQP1 (~22%), Rh (~36%), and an unknown pCMBS-sensitive protein account for ~91% of membrane O_2 permeability.

Abstract

Many have believed that oxygen (O_2) crosses red blood cell (RBC) membranes by dissolving in lipids that offer a finite resistance to diffusion or, alternatively, no resistance at all. In this first in a series of three interrelated papers, we examine these idea in murine RBCs. In this first paper, analyses of hemoglobin (Hb) absorbance spectra during O_2 off-loading from mouse RBCs indicate that RBC membranes do indeed offer resistance to O_2 diffusion, and that the resistance would be far higher if not for the presence of O_2-permeable channels. Two agents—both excluded from the RBC interior—markedly reduce the rate constant for O_2 off-loading (k_{HbO2}): p-chloromercuribenzenesulfonate (pCMBS) reduces membrane O_2 permeability (P_{M,O_2} by ~82% (computed from k_{HbO2} in paper #3), and 4,4'-diisothiocyanatostilbene-2,2'-disulfonate (DIDS) by ~56%. Because neither likely produces these effects via membrane lipids, we examined RBCs from mice genetically deficient in aquaporin-1 (AQP1), the Rh complex (Rh_{Cx} = Rhesus blood group-associated A glycoprotein, RhAG + Rhesus blood group D antigen, RhD), or both. The double knockout (dKO) reduces P_{M,O_2} by ~55%, and pCMBS+dKO, by ~91%. Proteomic analyses of RBC membranes, flow cytometry, hematology (see paper #2), and mathematical simulations (paper #3) rule out meaningful contributions from other membrane proteins, RBC geometry, or extracellular unconvected fluid (EUF). Our work represents a paradigm shift for O_2 physiology by identifying the first two animal O_2 channels, and points to the existence of at least a third, all of which could be subject to physiological regulation and pharmacological intervention.

Introduction

Central to human life is the inhalation of oxygen (O_2), its diffusion across the alveolar wall to pulmonary capillary blood plasma, O_2 diffusion inward across the red blood cell (RBC) membrane and transfer to hemoglobin (Hb; $Hb + O_2 \rightarrow HbO_2$),[1] distribution of RBCs by blood flow throughout the body, O_2 offloading from Hb, and finally O_2 diffusion outward across the RBC membrane and other barriers to support oxidative metabolism. Critical to understanding this journey of O_2 from air to mitochondria is the diffusion of O_2 across various membranes, particularly that of the RBC.

Since the early 1800s, the mechanisms by which gases move across natural and artificial barriers have been the focus of numerous investigations (Graham, 1829, 1833; Mitchell, 1830, 1831*a*, 1831*b*, 1833; Fick, 1855; Overton, 1895; see review by Stannett, 1978). For example, Mitchell was the first to recognize that the "facility of transmission" (i.e., permeability) of gases through (primarily synthetic) membranes depends on their "power of infiltration" (i.e., solubility) in the organic molecular barrier (Mitchell, 1831*a*, 1831*b*). This was the first statement of "solubility theory" (see Stannett, 1978). Subsequently, Graham, who gave us Graham's law, hypothesized that gas permeation across barriers depends not only on the ability of the gas to dissolve in the barrier but also to diffuse through it—the first statement of solubility-diffusion theory. In 1879, Wroblewski combined Mitchell's and Graham's observations with Henry's law of gas solubility in liquids (Henry, 1803) and Fick's law of diffusion (Fick, 1855*b*, 1855*a*) to produce our current, simplified mathematical description of the solubility-diffusion theory

[1] We use HbO_2 to represent the generic oxygenated hemoglobin (i.e., oxyhemoglobin), measured in terms of mass concentration (e.g., g/dl). Of course, the Hb molecule is a tetramer. Under physiological conditions at sea level with the subject at rest, this tetramer enters the mammalian lung with 3 O_2 bound on average, $Hb(O_2)_3$, and exits the lung with 4 bound on average, $Hb(O_2)_4$.

(Wroblewski, 1879; for reviews, see Stannett, 1978; Cooper *et al.*, 2015; Michenkova *et al.*, 2021). In the late 1890s, Overton—whose aim was to determine whether biological membranes have a lipoid component—showed that membrane permeability is proportional to the lipophilicity (i.e., the lipid-water partition coefficient) of the permeating molecule (Overton, 1895, 1899). Although Overton's experiments were far more elegant than those of Mitchell, his conclusion was a restatement of Mitchell's solubility theory. Over the years, biologists—like Overton, apparently unaware of the work of Mitchell—began to refer to Overton's observations as "Overton's rule", even though Mitchell's solubility theory predated Overton by more than 60 years, and the "rule" altogether ignores Graham's more inclusive solubility-diffusion theory that predated Overton by three decades.

Thus, in the early 20th century, many biologists believed that the resistance that membranes offer to the diffusion of gases depends only on the solubility of the gas in the lipid phase of the membrane. Later work on the diffusion of carbon dioxide (CO_2) through artificial lipid membranes by (Blank & Roughton, 1960), (Gutknecht *et al.*, 1977), and (Simon & Gutknecht, 1980) showed that the diffusion component of solubility-diffusion theory is quantitatively far more important than the solubility component (see review by Boron, 2010). Nevertheless, the concept that gases cross membranes merely by dissolving in the lipid phase of the membrane—Overton's rule—became dogma, at least for most physiologists.

Interestingly, with a smaller group of 20th-century physiologists—influenced by the pioneering work of Krogh on O_2 offloading from RBCs and delivery to the tissues (Krogh, 1919)—a very different dogma evolved. Krogh's mathematical analysis of the "Krogh cylinder" required the implicit, simplifying assumption (see Kreuzer, 1982) that the various cell membranes, including the RBC membrane, offer no resistance to O_2 diffusion. Although some notable physiologists argued otherwise (Hartridge & Roughton, 1927; Forster, 1964), Krogh's implicit assumption became engrained in the literature, and many came to believe that O_2 crosses RBC membranes simply by dissolving in lipids that offer no resistance whatsoever to diffusion.

Calling the above prevailing views into question were two discoveries, namely, the identification of: (1) membranes with no detectable CO_2 permeability (Waisbren *et al.*, 1994), specifically the apical (i.e., lumen-side membranes) of chief and parietal cells of gastric-glands; and (2) a membrane protein (i.e., aquaporin-1, AQP1; (Preston & Agre, 1991; Preston *et al.*, 1992) with an additional role as a CO_2 channel (Nakhoul *et al.*, 1998; Cooper & Boron, 1998). The reagent p-chloromercuribenzenesulfonate (pCMBS), which reacts with the –SH of Cys-189 in the extracellular vestibule of the AQP1 monomeric pore, not only inhibits H_2O movement through AQP1 (Preston *et al.*, 1993), but also blocks a component of CO_2 traffic through AQP1 (Cooper & Boron, 1998). Moreover, various AQPs exhibit CO_2 vs. NH_3 selectivity (Musa-Aziz *et al.*, 2009; Geyer *et al.*, 2013*b*). Other work suggested that rhesus (Rh) proteins also can conduct CO_2 (Endeward *et al.*, 2008). These observations revealed that gas transport across membranes must involve more than that predicted by solubility-diffusion theory: the solvation into the lipid bilayer, diffusion through the bilayer, and the desolvation at the opposite side of the bilayer. Work on human RBCs genetically deficient in AQP1 (Endeward *et al.*, 2006) or the Rhesus blood group-associated A glycoprotein RhAG (Endeward *et al.*, 2008) established that AQP1 and perhaps the Rh complex (Rh_{Cx}= RhAG + RhD) as well—if human Rh-null RBCs are indeed biconcave disks—together account for >90% of CO_2 permeability of RBCs. Moreover, that work established that 4,4'-diisothiocyanatostilbene-2,2'-disulfonate (DIDS), which binds to and can react with the $-NH_3^+/NH_2$ moiety of Lys residues, blocks a component of CO_2 traffic through AQP1 and perhaps also Rh_{Cx}. Although neither pCMBS nor DIDS is specific, both are valuable tools because (as we show in the present paper) they do not enter RBCs, and they have minimal presence in the lipid phase of the plasma membrane (Vansteveninck *et al.*, 1965; Rothstein *et al.*, 1973; Cabantchik & Rothstein, 1974). Thus, we hypothesize that—like CO_2—O_2 crosses RBC membranes mainly via channels, and that pCMBS or DIDS would block these hypothetical O_2 channels.

The present study comprises three tightly interwoven papers that aim to determine the extent to which AQP1, Rh_{Cx}, and potentially other RBC membrane proteins contribute to the O_2 permeability of the RBC membrane (P_{M,O_2}).

In this first (the present) paper, we use stopped-flow (SF) absorbance spectroscopy to determine the rate constant for Hb deoxygenation (k_{HbO2}) as we mix oxygenated murine RBCs with a solution containing the O_2 scavenger sodium dithionite (NDT). This first paper also examines the channel inhibitors pCMBS and DIDS in wild-type (WT) mice, and also RBCs from mice genetically deficient in AQP1, RhAG, or both (i.e., double knockouts, dKO). Recognizing that differences in k_{HbO2} associated with drugs or knockouts (KOs) could reflect changes in parameters other than P_{M,O_2}, we also examine the kinetics of the reaction $HbO_2 \rightarrow Hb + O_2$ in free solution as well as hematological parameters, including mean corpuscular volume (MCV) and mean corpuscular hemoglobin (MCH). This first paper also serves as the overall summary of the three-paper project by briefly summarizing, in context, key elements of the other two papers, and providing references to specific locations in those papers.

The second paper (i.e., paper #2; (Moss *et al.*, 2025) complements the first by examining RBC morphology at a microscopic scale, including measurements of RBC major diameter ($Ø_{Major}$; i.e., maximum dimension) using imaging flow cytometry (IFC). These data, together with MCV data from the present paper, allow us (in paper #3) to estimate RBC thickness. These IFC data also show that, although nearly all RBCs under control conditions (Ctrl; i.e., no drug treatments) are biconcave disks (BCDs), some are non-biconcave disks (nBCDs); IFC determines nBCD prevalence. In addition, paper #2 includes a proteomic analysis that confirms that the RBC membranes of genetically deficient mice lack only the intended proteins among the 100 proteins with the greatest inferred abundance.

In the third paper (i.e., paper #3; (Occhipinti *et al.*, 2025) we report the development of a novel mathematical reaction-diffusion model for O_2 offloading from an RBC, based on first

principles, in which we treat the RBC as a sphere with a diameter that reflects the computed RBC thickness. Together with physical constants, parameter values from the literature, and data from the first two papers, this model generates simulations that are in good agreement with the physiological data, allowing us to extract P_{M,O_2} values from k_{HbO2} and other wet-lab data. Our graphical user interface (Huffman *et al.*, 2025) expands the power of the model, especially for non-experts.

The overall conclusion of the three papers is that, contrary to the implicit assumption of Krogh, RBC membranes of WT mice under control conditions—that is, WT/Ctrl—offer considerable resistance to O_2 diffusion, with a computed permeability ~150 greater than an equivalent layer of water. AQP1 (~22%) and Rh_{Cx} (~36%) account for ~55% of the usual P_{M,O_2}. Moreover, at least one other pCMBS-sensitive protein is responsible for an additional ~36%, so that that total protein-mediated component of P_{M,O_2} is at least ~91%. Thus, the work presented in the present three papers changes the way we think of RBC O_2 handling, and raises the prospect of treating human disease by modulating P_{M,O_2} by manipulating membrane proteins[2].

[2] This manuscript was first published as a preprint: Zhao P, Moss FJ, Occhipinti R, Geyer RR, Huffman DE, Meyerson HJ & Boron W F (2025). Role of channels in the O_2 permeability of murine red blood cells. I. Stopped-flow and hematological studies. bioRxiv. https://doi.org/10.1101/2025.03.05.639948

Methods

Ethical approval and animal procedures

The Institutional Animal Care and Use Committee (IACUC) at Case Western Reserve University (CWRU) reviewed and approved all animal procedures.

Mice

We originally obtained as *Aqp1*+/– mice—with a targeted disruption (replacement of the last 24 bp of exon 1 and 1.3 kb of intron 1 by the 1.8-kb PolII-neo selectable marker) of the *Aqp1* gene (Ma *et al.*, 1998)—on a "C57BL/6" background (Kelmenson, 2016), as a generous gift of Alan Verkman. The *Aqp1*+/+ mice obtained from the initial crosses were backcrossed for >20 generations by our laboratory to define our lab-standard WT strain, C57BL/6_{Case}.

We backcrossed *Aqp1*+/– mice into our C57BL/6_{Case} WT mice for >18 generations, and confirmed genotypes. Similarly, we backcrossed *Rhag*+/– mice (provided by Jean-Pierre Cartron as *Rhag*+/– mice on a "C57BL/6" background), with a targeted disruption of *Rhag* (Goossens *et al.*, 2010), with C57BL/6_{Case} mice and backcrossed into C57BL/6_{Case} mice for at least 7 generations. From *Aqp1*–/– and *Rhag*–/– mice, we generated dKO (i.e., *Aqp1*–/–*Rhag*–/–) mice, and confirmed genotypes as described below. All three KO strains we routinely confirmed by genotyping (see Genotyping).

We contracted with TransnetYX, Inc. (Cordova, TN) to perform Genetic Background analysis on our four mouse strains, all on a C57BL/6_{Case} background. TransnetYX examined all ~10,000 single-nucleotide polymorphisms (SNPs) in their catalog, SNPs from >200 strains of mice. These included 156 SNPs specific for C57BL/6J (from Jackson Laboratory), 31 SNPs for C57BL/6N (from the National Institutes of Health), and 21 SNPs for C57BL/6Group (characteristic of other C57BL/6 strains). Table 1 summarizes the results of this analysis, which

shows that our C57BL/6_{Case} mice are on average ~19.6% C57BL/6J, ~20.6% C57BL/6N, ~25.6% C57BL/6Group, for a total BL/6 character of ~65.8%.

Mice were allowed access to food and water ad libitum. In experiments, we used mice of both sexes (8 to 19 weeks old). Not shown are data indicating that no changes in kinetic or hematological parameters occur up to 6 months of age for all genotypes.

Genotyping

WT vs. *Aqp1*+/– vs. *Aqp1*–/– are genotyped by real-time PCR (performed by TransnetYX, Inc.). For detecting the *Aqp1*– allele, the forward primer is 5′-CAC CTC GGT AGC AAC TCG AA-3′, the reporter primer 1 is 5′-CTC CTC GAA GGA ATT C-3′, and the reverse primer is 5′-GGG CTC GAG ATC CAC TAG ACT-3′. For detecting WT, the forward primer is 5′-CTT AGG CTT AGG GTG TCT GTA GGA-3′, the reporter primer 1 is 5′-CTG GCT CCA TTT GCC-3′, and the reverse primer is 5′-CTT CAT CCT TCT CTC TGT TCT TCA GT-3′.

WT vs. *Rhag*+/– vs. *Rhag*–/– mice are genotyped by real-time PCR (performed by TransnetYX, Inc.) to determine the presence of a *Rhag*–allele. For detecting the KO allele, the forward primer is 5′-TGC TGC TAT GAC CAT TGG AA-3′, and the reverse primer is 5′-ATT GCA TCG CAT TGT CTG AG-3′. The KO PCR results 196-bp band.

If we detect a KO allele in a mouse, we must differentiate between a *Rhag*+/– and *Rhag*–/– mouse by attempting to detect the WT allele. We perform this assay in house because the PCR product is long (~8 kb). We prepare highly purified genomic DNA from tail tissue using the DNeasy Blood and Tissue Kit (Qiagen, Germantown, MD), and perform *Rhag*-WT genotyping. Primer "*Rhag*-WT 3F" (5′-TGA AAT GTT TAA TGC TCA TCG ACC AC-3′) is designed to anneal to the end of Intron 1–2 of *Rhag*, and Primer "*Rhag*-WT 3R" (5′-GAG TGA CTT CA CCT TCT TAT CTT CTA AG-3′), to the middle of intron 6–7. The *Rhag*-WT PCR product is ~8 kb, as noted above, using the Qiagen Long Range (LR) PCR Kit. Presence of the WT-PCR product

confirms a *Rhag*+/– genotype for any mouse reported to be positive for *Rhag*–/– by TransnetYX. Absence of a WT-PCR product confirms the *Rhag*–/– genotype.

Physiological solutions

Table 2 shows the compositions of all solutions used in the present study. We made pH measurements—either at room temperature (RT) or at 10°C—using a portable pH meter (model A121 Orion Star, Thermo Fischer Scientific (TFS), Waltham, MA) fitted with a pH electrode (Ross Sure-Flow combination pH Electrode, TFS). Beakers containing pH calibration buffers (pH at 6, 8 and 10; TFS), physiological solutions to be titrated, and the pH electrode in its storage solution (Beckman Coulter, Inc. Brea, CA) were equilibrated at either RT or 10°C, as appropriate. For work at 10°C, we used a refrigerated, constant-temperature, shaker water bath (model RWB 3220, TFS) and submersible Telesystem magnetic stirrers (TFS). We adjusted pH with NaOH (5 M) or HCl (5 M). Osmolality was measured using a vapor pressure osmometer (Vapro 5520; Wescor, Inc., Logan, UT) and, as necessary, adjusted upward by addition of NaCl.

Inhibitors

Stock solutions of 2 mM pCMBS (catalog no. C367750; Toronto Research Chemicals, Toronto, ON, Canada) and 2 mM DIDS (catalog no. 1226913; Invitrogen, Eugene, OR) were freshly prepared (generally 1–2 h before experiments) by dissolving the agents directly into either our "Oxygenated solution" or solution "$\mathcal{A}$" (see Table 2), taking care to shield the solutions from light.

Preparation of RBCs

Collection of blood from mice. We collected fresh blood from WT or KO mice for seven assays: (1) SF, (2) still microphotography, (3) microvideography, (4) flow cytometry, (5) automated hematology, (6) blood smears, and (7) proteomics/mass spectrometry. Early on (only for SF studies), we collected blood using the cardiac-puncture method (Parasuraman *et al.*, 2010).

Later (for the remaining SF and all other studies), so that we could return to the same mouse for more than one sample of blood, we used the submandibular-bleed method (Golde *et al.*, 2005). For cardiac puncture, we used a 1-ml syringe (Becton, Dickinson and Co., Franklin Lakes, New Jersey) and attached 23-gauge PrecisionGlide needle (Becton, Dickinson and Co). For bleeds of the submandibular vein, we used a 3-, 4-, or 5-mm point-length sterile animal lancet (MEDIpoint, Inc., Mineola, NY), and took blood samples (~200 μl) from the same mouse no sooner than 72 h from a previous blood sample, and on the contralateral side.

Processing of RBCs for assays 1–4. For the first four assays (SF, still microphotography, microvideography, flow cytometry), we collected the blood into 1.7-ml microcentrifuge tubes (Laboratory Products Sales Inc. Rochester, N.Y.) that we had previously rinsed with 0.1% sodium heparin (H4784, Sigma-Aldrich, St. Louis, MO). We then centrifuged in a Microfuge 16 Microcentrifuge (Beckman Coulter, Inc.) at 600 × g for 10 min, and aspirated and discarded the resulting supernatant and buffy coat. To remove residual extracellular Hb, we resuspended the pelleted RBCs in our oxygenated solution (see Table 2) to a hematocrit (Hct) of 5% to 10%, centrifuged at 600 × g for 5 min. After 4 such washes, we resuspended RBCs in our oxygenated solution to a final Hct of 25% to 30%, and maintained on ice (for that day) for experiments. At this point, we continued with the processing of RBCs for SF studies (the present paper; see below[3]) or for the three studies in paper #2, namely, still microphotography, microvideography, or flow-cytometry[4].

---

[3] See Methods>Preparation of RBCs>Processing of RBCs for stopped-flow studies. The ">" symbol separates heading levels. It is understood that the reference is to a location in the present paper unless "See" is followed by "Paper #2" or "Paper #3".

[4] See Paper #2>Methods>Preparation of RBCs>First four assays

Processing of RBCs for automated hematology. For automated hematological studies (see below[5]), we collected whole blood into 20-µl plastic Boule MPA Micro pipettes (EDTA-K2, Boule Medical AB, Stockholm, Sweden).

Processing of RBCs for blood smears. For blood smears[6], we collected whole blood into 2-ml K2E K2EDTA VACUETTE® tubes (Grelner Bio-One North America Inc, Monroe, NC).

Processing of RBCs for proteomics. For Proteomic analysis[7], we collected whole blood into 1.7-ml heparinized microcentrifuge tubes (see above[8]).

Processing of RBCs for stopped-flow studies. For SF studies, after collection of the blood (see above[9]), we computed [Hb] in a suspension of intact RBCs from the Hb absorbance measured on a UV/Vis spectrophotometer (model 730 Life Science, Beckman Coulter, Inc.), using an equation described previously (Zhao *et al.*, 2017).

As necessary, we produced an RBC lysate by osmotic lysis of 20 µl of freshly prepared, packed mouse RBCs in a 1:8~1:10 dilution of Milli-Q H_2O (Milli-Q® Integral Water Purification System, EMD Millipore Corporation, Billerica, MA), followed by centrifugation at 15000 × g for 5 min in a Microfuge 16 Microcentrifuge, at RT. We transferred the supernatant to a clean 1.7-ml

---

[5] See Methods>Automated hematological analyses (workflow #7-9)

[6] See Paper #2>Methods>Blood smears

[7] See Paper #2>Methods>Proteomic analysis

[8] See Methods>Preparation of RBCs>Processing of RBCs for assays 1–4

[9] See Methods>Preparation of RBCs>Collection of blood from mice

microcentrifuge tube for a spectroscopic determination of free [Hb], as described previously (Zhao *et al.*, 2017).

For all stopped-flow experiments—on intact RBCs or lysates or mixtures thereof—we dilute the material to a [Hb] of 5 μM before introduction into the SF device. After mixing in the SF reaction cell, [Hb] falls to a final values of 2.5 μM. In the case of deoxygenation assays (e.g., in Results, see Figure 3 and Figure 4), the diluent was our oxygenated solution (see Table 2). In the case of carbonic-anhydrase assays (e.g., in Results, see summary in Figure 6; see Zhao *et al.*, 2017), the diluent was solution "$\mathcal{A}$" (see Table 2), which is also oxygenated.

Use of inhibitors in stopped-flow studies. In all inhibitor studies, except those in which we studied short-term exposures to DIDS (introduced next), we pre-incubated samples (either ostensibly intact RBCs or a hemolysate) with the drug before introduction into the SF device:

(1) pCMBS (1 mM): 15-min preincubation. For:

(a) ostensibly intact RBCs, see Figure 3*C* and *D*, as well as filled bars in Figure 3*E* and *F*;

(b) hemolysate, see open bars in Figure 3*F*.

(2) DIDS (200 μM): 60-min preincubation. For:

(a) ostensibly intact RBCs, see Figure 4*C* and *D* as well as filled bars in Figure 4*E* and *F*;

(b) hemolysate, see open bars in Figure 4*F* as well as filled gray-blue bar in Figure 8*A*).

The next step, for both drugs, was to dilute the material in our oxygenated solution (see Table 2) to achieve a [Hb] of 5 μM plus either 1 mM pCMBS or 200 μM DIDS, added from a stock solution (see "Inhibitors", above[10]). Finally, we performed stopped-flow studies by mixing the aforementioned oxygenated solution with the deoxygenated solution (see Table 2) to obtain k_{HbO_2}.

In a few studies, we assessed the effect of millisecond-to-second DIDS exposures on Hb absorbance spectra of hemolysates (e.g., in Results, see Figure 8*B*, gray-blue open bar). Here, we did not preincubated the hemolysate in DIDS. Rather, we placed (1) the lysate in the oxygenated solution and (2) the DIDS in the deoxygenated solution (see Table 2). Thus, the DIDS did not contact the Hb in the lysate until reaching the SF reaction cell as we determined k_{HbO_2}.

Stopped-flow absorbance spectroscopy (workflow #1)

The flow chart in Figure 1 describes the series of steps—starting with the time course of RBC absorbance spectra (workflow: step #1) introduced in this section—to arrive at refined estimates for k_{HbO_2} and the associated P_{M,O_2}.

We use an SX-20 stopped-flow apparatus (Applied Photophysics, Leatherhead, UK) in absorbance spectroscopy mode to determine the rate constant of hemoglobin deoxygenation. We load RBCs or RBC/ hemolysate mixtures or pure hemolysate ([Hb] = 5 μM, Hct ≅ 0.37%), suspended in our oxygenated solution (see Table 2), into one syringe of the SF apparatus. We load the deoxygenated solution containing the O_2 scavenger NDT (50 mM; SIGMA-ALDRICH, Co, St, Louis, MO) into the other syringe. We record absorbance (*A*) in a 20-μl SF reaction cell (2-mm path length) at 10°C, over the portion of the Hb spectrum with highest Signal/Noise (wavelength

[10] See Methods>Inhibitors

[λ]: 410–450 nm, at 5 nm intervals), sampling at 10-ms intervals for 4000 ms. For each new set of loaded samples, we begin by performing ≥6 "shots" to ensure that the new solutions are loaded into the SF reaction cell, and then sequentially acquire $A\lambda$ vs. time during 9 separate shots at λ = 410, 415 … 450 nm—this constitutes one data set. We compile such data set into 3-D graphs (e.g., in Results, see $A\lambda$ vs. λ vs. time plots in Figure 3*A* and *C* as well as Figure 4*A* and *C*). We obtain at least 1 such data set (see criteria in next section)—but typically 2 to 4—for each set of experimental conditions, and then average these k_{HbO_2} values to obtain the raw-k_{HbO_2} value used in further analyses.

The above sequence is step #1 in Figure 1.

Calculation of time course of HbO_2 desaturation (workflow #2)

The time course of the decay $HbO_2 \rightarrow Hb + O_2$ does not follow a perfect exponential function—nor should it according to our mathematical modeling (e.g., see figure 4 in paper #3). We therefore developed an unbiased approach[11] for computing the quasi-rate constant k_{HbO_2}, based on the time (t_{37}) required for O_2 saturation of Hb (HbSat) to fall to 1/e of its initial value. We proceed in the following sequence:

Preprocess data. Eliminate noisy absorbance data—which we standardize as the first 9 points (0.010 – 0.090 s)—and translate the time axis so that raw data at absolute times 0.100 – 4.000 s now covers the relative time range 0.000 – 3.900 s. We also eliminate data at 3 wavelengths (420, 445, 450 nm) that are near isosbestic points of the Hb/HbO_2 absorbance spectra because, at these wavelengths, absorbance values do not change consistently during an experiment. The result

[11] The "Pro-KIV" software supplied by Applied Photophysics assumes that the absorbances at all wavelengths decay as a perfect exponential, and fits them all simultaneously, producing a single time constant/rate. Because this approach could introduce a bias into the analysis, we developed the method described here. Nevertheless, the two approaches produce numerical results that differ only slightly, and do not affect the conclusions that we draw.

is a data set describing A_λ vs. relative time (from 0.000 to 3.900 s) at each of 6 wavelengths (λ = 410, 415, 425, 430, 435, and 440 nm). We accept a data set only if each of the 6 records of A_λ vs. time approaches an asymptote.

Obtain data parameters. For each of 6 plots of A_λ vs. time, obtain the minimum ($A_{\lambda,\mathrm{min}}$) and maximum values ($A_{\lambda,\mathrm{max}}$), as well as the difference $\Delta A_\lambda = A_{\lambda,\mathrm{max}} - A_{\lambda,\mathrm{min}}$ (i.e,. magnitude of the absorbance change). The 6 values of ΔA_λ become weighting factors, applied two paragraphs below.

Normalize. Perform a vertical flip of plots of A_λ vs. time that were originally concave downwards (these are λ = 425, 430, 435, 440 nm), so that all plots are now concave upwards. Vertically translate each plot of A_λ vs. time so that the minimum value is zero. Normalize each plot of A_λ vs. time so that $A_{\lambda,\mathrm{max}}$ is now unity.

Apply weighting factors. Normalize the 6 weighting factors (i.e., ΔA_λ) so that they sum to unity. Multiply each plot of A_λ vs. time by its weighting factor. At each time point, sum the 6 weighted A_λ values to obtain relative HbSat. The resulting plot of relative HbSat thus falls from unity to zero as relative time increases from 0.000 s to 3.900 s. Note that—because the RBCs or Hb are equilibrated in room air before being loaded into the SF device—the actual HbSat falls from a value of ~98% when the RBCs first enter the SF reaction cell at absolute time 0.000 s, and has already fallen to some extent by the time of our first accepted sample at absolute time 0.100 s, and then continues to fall to zero during the remaining 3.900 s of the "shot."

The above sequence is step #2 in Figure 1.

In Results, Figure 3*D*, Figure 4*D*, as well as Figure 5*A, C,* and *E* show examples of the final product of such analyses, that is, plots of HbSat vs. time.

Calculation of raw-k_{HbO2} (workflow #3)

Examining the plot of relative HbSat vs. relative time data (see above[12]), we estimate t_{37}. We then identify the 5 relative HbSat points to the left[13] and the 5 points to the right of the estimated t_{37}, and fit the 11 points with a polynomial of degree 2, and solve the best-fit polynomial for the actual relative t_{37}, and compute the raw-k_{HbO_2} as $1/t_{37}$.

The above sequence is step #3 in Figure 1.

Quantitation of hemolysis in SF reaction cell (workflow #4)

We have developed a novel assay (not depicted here; see Zhao *et al.*, 2017), based on the activity of carbonic anhydrase (CA), for determining the degree of RBC hemolysis in the SF reaction cell in a time domain similar to that of our O_2-efflux experiments (e.g., in Results, see Figure 3*A* and *C*). We use the SF apparatus to mix solutions $\mathcal{A}$ and $\mathcal{B}$ (see Table 2) in the SF reaction cell, and create an out-of-equilibrium (OOE) CO_2/HCO_3^-/pH state, chosen such that the pH at the instant of mixing is too low for equilibrium (in Results, see Figure 6*A*). The OOE solution then re-equilibrates according to the reaction $HCO_3^- + H^+ \rightarrow CO_2 + H_2O$ (i.e., raising pH), catalyzed by CA released from hemolyzed RBCs (in Results, see Figure 6*B*–*D*).

Solution $\mathcal{A}$ contains HEPES/pH 7.03 + RBCs or hemolysate. Solution $\mathcal{B}$ contains ~1% CO_2/44 mM HCO_3^-/pH 8.41 + the fluorescent pH-sensitive dye pyranine (catalog no. H348, Invitrogen), which reports extracellular pH (pH_o). We excite the dye at 460 nm or 415 nm, while monitoring total fluorescence emission using a 488-nm long-pass filter. Immediately upon mixing of $\mathcal{A}$ and $\mathcal{B}$, the solution in the SF reaction cell (10°C) has the composition ~0.5% CO_2/22

---

[12] See Methods>Calculation of time course of HbO_2 desaturation>Apply weighting factors

[13] In some cases, HbSat fell so rapidly that we were forced to use < 5 points to the left.

HCO_3^-/pH ~7.25, which is out of equilibrium. The pH_o rises exponentially (rate constant, $k_{\Delta pH}$, computed as described previously (Zhao *et al.*, 2017)) to ~7.50.

We calculate the actual percent hemolysis (*Act%H*) of ostensibly 100% intact RBCs (i.e., apparent percent hemolysis, *App%H*, is 0%) during a SF experiment, as described previously (Zhao *et al.*, 2017), using a procedure that requires three rate constants: k_{uncat}, $k_{RBC,Lysate}$, and $k_{RBC,OstInt}$. (1) k_{uncat} is the uncatalyzed $k_{\Delta pH}$ (without CA). (2) $k_{RBC,Lysate}$ is $k_{\Delta pH}$ in the presence of fully lysed RBCs. Finally, (3) $k_{RBC,OstInt}$ is $k_{\Delta pH}$ in the presence of ostensibly 100% intact RBCs. From these, we compute $k_{cat,min} = k_{RBC,OstInt} - k_{uncat}$ and $k_{cat,max} = k_{RBC,Lysate} - k_{uncat}$. Finally,

$$Act\%H_{\mathrm{App}\%H=0\%} = \frac{k_{\mathrm{cat,min}}}{k_{\mathrm{cat,max}}}.$$

The above equation yields the actual percent hemolysis at a time when the apparent % hemolysis is 0%.

The above sequence is step #4 in Figure 1.

Accommodation for hemolysis (workflow #5)

Control and pCMBS-treated RBCs. Because (1) the RBC membrane has a much higher resistance to O_2 permeation than does an equivalent thickness of water and (2) NDT can approach HbO_2 more closely in free solution, Hb released into free solution deoxygenates faster than Hb inside RBCs. We correct raw-k_{HbO_2} values (step #3 in Figure 1), based on actual % hemolysis values (step #4 in Figure 1). For each mouse, we generate simulated hemolysis samples for apparent hemolysis levels of 0% (i.e., ostensibly 100% intact RBCs), 2.5%, 5%, 10% and 25% by mixing ostensibly 100% intact RBCs (at relative levels of 100%, 97.5%, 95%, 90%, and 75%) with hemolysate (at relative levels of 0%, 2.5%, 5%, 10%, and 25%)—keeping total [Hb] constant

at 5 μM. We determine raw-k_{HbO_2} (see above[14]) for each of these simulated hemolysis samples, and—using an algebraic scaling and translation of the x-axis—convert a plot of k_{HbO_2} vs. *App%H* (e.g., in Results, see blue axes in Figure 7*A* and *B*) to a plot of k_{HbO_2} vs. *Act%H* (see green axes). Extrapolating k_{HbO_2} back to 0% actual hemolysis yields an estimate of the actual k_{HbO_2} for 1 mouse. We used this approach for all experiments for RBCs treated with pCMBS or no drug.

The above sequence—for RBCs exposed to no drug or to pCMBS—is step #5 in Figure 1.

DIDS-treated RBCs. For RBCs treated with DIDS, we modified the above[15] approach because DIDS decreases the k_{HbO_2} of free Hb, so that the actual slope of the k_{HbO_2} vs. *Act%H* regression line ($Slope_{DIDS,Act}$) is less than the control value ($Slope_{Ctrl,Act}$). Two factors are at work. (1) During the 1-h pretreatment of RBCs with DIDS, the drug produces a substantial reduction in k_{HbO_2} (in Results, see Figure 8*A*), although this affects only a minute fraction of RBCs that have hemolyzed before entry into the SF device (see Zhao *et al.*, 2017). (2) During the actual SF experiment, DIDS produces a small reduction in k_{HbO_2} (in Results, see Figure 8*B*) for a larger fraction of Hb newly released in the SF reaction cell over a millisecond/second time frame. For Figure 8*A* and *B*, we obtained free Hb (from hemolysates) and exposed it to DIDS as described in the figure legends.

In a DIDS experiment, the actual slope of the regression line becomes

---

[14] See Methods>Calculation of raw-k_{HbO_2} (workflow #3)

[15] See Methods>Accommodation for hemolysis (workflow #5)>Control and pCMBS-treated RBCs

$$Slope_{\mathrm{DIDS,Act}} = Slope_{\mathrm{Ctrl,Act}} \left[\underbrace{\underbrace{\frac{k_{\mathrm{HbO_2DIDS,1\text{-}h}}}{k_{\mathrm{HbO_2Ctrl}}}}_{\substack{\text{\% remaining after}\\ \text{1-h DIDS}}} \cdot \underbrace{\frac{\%H_{\mathrm{RBCs,Washed}}}{\%H_{\mathrm{RBCs,RxCell}}}}_{\substack{\text{\% [Hb]}_{\mathrm{o}}\text{ exposed}\\ \text{to DIDS} \times \text{1 h}}}}_{\substack{\text{\% } k_{\mathrm{HbO_2}} \text{ that remains for the free Hb exposed}\\ \text{to DIDS for 1h in tube before SF}}} + \underbrace{\underbrace{\frac{k_{\mathrm{HbO_2DIDS,ms/s}}}{k_{\mathrm{HbO_2Ctrl}}}}_{\substack{\text{\% remaining after}\\ \text{ms/s DIDS}}} \cdot \underbrace{\frac{\%H_{\mathrm{RBCs,RxCell}} - \%H_{\mathrm{RBCs,Washed}}}{\%H_{\mathrm{RBCs,RxCell}}}}_{\substack{\text{\% [Hb]}_{\mathrm{o}}\text{ exposed}\\ \text{to DIDS} \times \text{ms/s}}}}_{\substack{\text{\% } k_{\mathrm{HbO_2}} \text{ that remains for the free Hb exposed}\\ \text{to DIDS for ms/s in SF reaction cell}}} \right]$$

(1)

Thus, knowing the $k_{\mathrm{HbO_2}}$ measured in ostensibly 100% intact RBCs ($k_{\mathrm{HbO_2DIDS,OstInt}}$), we can estimate the actual $k_{\mathrm{HbO_2}}$ for DIDS-treated RBCs as

$$k_{\mathrm{HbO_2DIDS,Act}} = k_{\mathrm{HbO_2DIDS,OstInt}} - Slope_{\mathrm{DIDS,Act}} \cdot \left(Act\%H \right).$$

The above sequence—for DIDS-treated cells—is step #5 in Figure 1.

Measurement of major cell diameter (workflow #6 & #6′)

As described in paper #2[16], we use imaging flow cytometry to measure the major diameter ($Ø_{\mathrm{Major}}$) of cells shaped as biconcave disks or non-biconcave disks. The determination of $Ø_{\mathrm{Major}}$ for BCDs is step #6 in Figure 1, whereas the determination of the counterpart $Ø_{\mathrm{Major}}$ for nBCDs (assumed in our analysis to be spheres) is step #6′.

Automated hematological analyses (workflow #7 – #9)

Assays on normal whole blood. We collect fresh whole blood into special pipettes (see above[17]), which we insert into a Heska HemaTrue® Veterinary Hematology Analyzer (Heska corporation, Loveland, CO) according to the manufacturer's protocol. The HemaTrue® analysis

[16] See Paper #2>Methods>Flow cytometry>Imaging flow cytometry

[17] See Methods>Preparation of RBCs>Processing of RBCs for automated hematology (workflow #7 – #9)

yields a wide variety of parameters (introduced below in Table 4), including those related to white and red blood cells and platelets; Hct; MCH (step #7 in the flowchart, Figure 1); MCV (step #8); and MCHC (computed from MCH and MCV in step #9).

Use of inhibitors in automated hematological studies. After collecting fresh whole blood from WT or dKO mice, we processed the cells as in "first four assays" (see above[18]), except that—after centrifugation and removal of the buffy coat—we performed only 2 washes (rather than 4) to remove residual extracellular Hb. We then resuspended RBCs in our oxygenated solution (see Table 2), alternatively, (1) without any drug, (2) with pCMBS (1 mM × 15 min), or (3) with DIDS (200 μM × 1 h), to a final Hct of 25%. After centrifuging RBCs at 600 × g for 5 min, we aspirated and discarded the resulting supernatant to remove inhibitors. We then resuspended RBCs in our oxygenated solution to an Hct of 5% to 10%, centrifuged at 600 × g for 5 min, and performed 1 last wash. Finally, we either resuspended packed RBCs at ostensibly 50% Hct for automated hematological assays, or directed the RBCs to studies of flow-cytometry[19].

The above sequence is step #7–#9 in Figure 1.

Estimation of thickness of biconcave disks (workflow #10)

As described in paper #3[20], we generate a torus that has a major outer diameter that matches the measured mean $Ø_{RBC,major}$ of the RBC population (see above[21]), and has a volume that matches

---

[18] See Methods>Preparation of RBCs>Processing of RBCs for assays 1–4

[19] See Paper #2>Methods>Flow cytometry>Use of inhibitors in imaging flow cytometry

[20] Paper #3>Methods>Mathematical modeling and simulations>Calculation of RBC thickness based on the geometry of a torus

[21] See Methods>Measurement of major cell diameter (workflow #6 & 6′)

the measured mean MCV (see above[22]). We take the RBC thickness as the minor diameter of the torus.

The above sequence is step #10 in Figure 1.

Determination of rate constant $k_{HbO2 \rightarrow Hb+O2}$ (workflow #11)

We ascertain the rate constant of the reaction $HbO_2 \rightarrow Hb + O_2$ in 100% hemolyzed RBCs—or mixtures of hemolysate and ostensibly intact RBCs—as described above[23] for 100% ostensibly intact RBCs. Above[24], we also describe the preparation of the lysate.

Construction of "sigmoid curves" (workflow #12 & #12′)

Introduced below[25] for BCDs (step #12) and nBCDs (step #12′).

Estimation of provisional P_{M,O_2} (workflow #13)

Introduced below[26].

---

[22] See Methods>Automated hematological analyses (workflow #7 – #9)

[23] See Methods>Calculation of raw-k_{HbO_2} (workflow #3)

[24] See Methods>Preparation of RBCs>Processing of RBCs for stopped-flow studies>"osmotic lysis" in text

[25] See Methods> Macroscopic Mathematical Modeling (MMM) and simulation of HbO_2-deoxygenation time courses, yielding the "sigmoidal curves" (workflow #12 & #12′)

[26] See Methods>Accommodation for nBCDs>Assignment of Provisional P_{M,O_2} (workflow #13)

Simulations (workflow #14 & #14′)

Introduced below[27] for BCDs (step #14) and nBCDs (step #14′).

Determination of prevalence of BCDs and nBCDs (workflow #15 & #15′)

As described in paper #2[28], we use imaging flow cytometry to determine the fraction of a cell population in our samples represented by various cell types, including BCDs vs. nBCDs.

These estimations are steps #15 and #15′ in Figure 1.

Macroscopic Mathematical Modeling (MMM) and simulation of HbO_2-deoxygenation time courses, yielding the "sigmoidal curves" (workflow #12 & #12′)

The details on the macroscopic[29] mathematical modeling and simulations are in paper #3[30]. In brief, we use a reaction-diffusion model—based on an approach originally developed for CO_2 fluxes across the membranes of *Xenopus* oocytes by Somersalo *et al.* (2012)—to represent O_2 efflux from an RBC that we model as a sphere with spherical-radial symmetry. Others have previously modeled RBCs as spheres (Vandegriff & Olson, 1984*a*; Williams & Kutchai, 1986; Deonikar & Kavdia, 2013; Deonikar *et al.*, 2014). These earlier workers took the sphere diameter

---

[27] See Methods>Accommodation for nBCDs>Simulations (workflow #14 & #14′)

[28] See Paper #2>Methods>Flow cytometry>Imaging flow cytometry (workflow #15 & #15′)

[29] We term this "macroscopic" to distinguish the present simulations at the cellular scale from mesoscopic modeling at the supramolecular scale and molecular-dynamics (MD) simulations at the atomic scale.

[30] See Paper #3>Methods>Mathematical modeling and simulations

to be the RBC major diameter, $Ø_{Major}$. In contrast, the value that we assign to the sphere diameter ($Ø_{Sphere}$) is the computed RBC thickness (see above[31]).

As illustrated in Figure 2, the model system comprises (1) a spherical RBC, (2) a plasma membrane that encompasses (3) intracellular fluid (ICF), (4) Hb and HbO_2 within the ICF, (5) a thin layer of extracellular unconvected fluid (EUF), and (6) an infinite reservoir of bulk extracellular fluid (bECF) that surrounds the EUF, and (7) O_2 throughout the system. Reactions among O_2, Hb and HbO_2 occur only in the ICF. We model the reaction term as the simple, one-step reversible reaction

$$HbO_2 \underset{k'}{\overset{k}{\rightleftharpoons}} Hb + O_2,$$

combined with an adaptation (see paper #3[32]) of the "variable rate coefficient" model proposed by Moll (1968), which guarantees that the hemoglobin-O_2 saturation curve is sigmoidal. All three solutes (i.e., O_2, Hb and HbO_2) diffuse within the cytosol. O_2 is the only solute that can move—via diffusion—through the plasma membrane, within the EUF and between EUF and bECF. Inputs to the simulations include (1) MCV and (2) MCH from automated hematological analyses (see above[33]), (3) the mean major diameter $Ø_{Major}$ of the BCDs (or non-BCDs) from imaging flow cytometry (see paper #2[34]), and (4) the rate constant of HbO_2 dissociation in an RBC lysate ($k_{HbO_2 \rightarrow Hb+O_2}$), which is equivalent to k in the above equation. Paper #3 contains details on the

[31] See Methods>Estimation of thickness of biconcave disks (workflow #10)

[32] See Paper #3>Methods>Mathematical modeling and simulations>Kinetics of the oxygen-hemoglobin reaction

[33] Methods>Automated hematological analyses (workflow #7 – #9)

[34] See Paper #2>Methods>Flow cytometry>Imaging flow cytometry

computational model[35], parameter values[36], and the simulation[37] of the time course of deoxygenation of HbO_2.

Using the MMM together with a set of parameter values—including physical constants, literature values, experimentally determined values (see paper #3[38]), some of which are specific for a particular group of RBCs (e.g., WT controls; see paper #3[39])—we can insert an assumed P_{M,O_2} value into the model and thereby predict the time course of HbSat (result of the reaction $HbO_2 \rightarrow Hb + O_2$). For each input P_{M,O_2} value, this exercise yields a corresponding MMM-k_{HbO2} value. Sweeping through a large number of P_{M,O_2} values, we construct the MMM-k_{HbO2} vs. $\log(P_{M,O_2})$ curves—the "sigmoid curves"—illustrated as steps #12 for BCDs and #12′ for nBCDs in Figure 1.

Accommodation for nBCDs (workflow #13, #14 & #14′, #16 – #22)

According to (1) our microvideography studies of RBCs on a coverslip, as visualized using a DIC microscopy (see paper #2[40]), and (2) imaging flow cytometry (see paper #2[41]), virtually all RBC samples comprise predominantly biconcave disks, but also some nBCDs. Although a nBCD

---

[35] Paper #3>Methods>Mathematical modeling and simulations>Computational model

[36] Paper #3>Methods>Mathematical modeling and simulations>Parameter values

[37] Paper #3>Methods>Mathematical modeling and simulations>Simulation of time course of HbO_2 deoxygenation, and estimation of k_{HbO_2}

[38] Paper #3>table 1

[39] Paper #3>table 2

[40] See Paper #2>Methods>Flow cytometry>Still microphotography and microvideography of living RBCs

[41] See Paper #2>Methods>Flow cytometry>Imaging flow cytometry (IFC)

ought to have the same intracellular total Hb content as a BCD, the intracellular diffusion distances are greater for nBCDs, resulting in a lower rate of O_2 offloading (see Figure 2). Thus, a mixture of BCDs and nBCDs will have an aggregate k_{HbO2} that is lower than the true k_{HbO2} of BCDs alone.

To arrive at the true k_{HbO2} for BCDs and extract the P_{M,O_2}, we accommodate for the presence of nBCDs using the novel algorithm comprising steps #13, #14, and #16 through #22 in Figure 1. The principle is straightforward: The time course of HbO_2 deoxygenation for a mixture of BCDs and nBCDs is the linear combination of the separate deoxygenation time courses of BCDs and nBCDs, each weighted for their relative numbers, as provided by imaging flow cytometry (see workflow #15 & #15′, above and in paper #2[42]). Our goal is to extract the contribution of BCDs from the mixture, as described in paper #3[43]. The following is a brief summary:

Assignment of Provisional P_{M,O_2} (workflow #13). For our initial estimate of P_{M,O_2}, we assume that the membrane permeability for O_2 in mouse RBCs has the same value as the CO_2 permeability (P_{M,CO_2}) of human RBCs, 0.15 cm s^{-1}, measured by Endeward *et al.* (2006).

Simulations (workflow #14 & #14′). Using the P_{M,O_2} of 0.15 cm s^{-1} from step #13, we ascertain from the sigmoid curve for BCDs in step #12 that the corresponding MMM-k_{HbO2} value is 3.99 s^{-1} for BCDs (upward and rightward arrows in step #12 of Figure 1). From this MMM-k_{HbO2}, we generate a plot of HbSat vs. time for BCDs. In parallel, we generate a second sigmoid curve, but for nBCDs[44] in step #12′ to ascertain that, for the same P_{M,O_2} of 0.15 cm s^{-1}, the MMM-

[42] See Paper #2>Methods>Flow cytometry>Imaging flow cytometry

[43] Paper #3>Results>Accommodation for non-BCDs

[44] Because the intracellular diffusion distances are greater for nBCDs than for BCDs, the O_2-offloading rates are all lower for nBCDs, so that the sigmoid curve is flatter.

k_{HbO2} of nBCDs is only 1.83 s^{-1}. From this second k_{HbO2} values, we generate a comparable plot—but with a much slower time course—of HbSat vs. time for nBCDs.

First linear combination (workflow #16). A first linear combination of the simulated BCD and nBCD time courses yields an initial estimate of the time course—and k_{HbO2}—of the BCD-nBCD mixture.

Various algebraic manipulations (workflow #17 – #22). A series of steps involving rebalancing (#17 & #17′); a second linear combination (#18); generation of an inverted sigmoid plot (#19), which we use to compute a shape-corrected (SC) P_{M,O_2} of BCDs and nBCDs (#20); calculation of a shape-correction factor (#21) for each of eight individual physiological experimental protocols—WT/control, AQP1-KO/Ctrl, RhAG-KO/Ctrl, dKO/Ctrl, WT/pCMBS, WT/DIDS, dKO/pCMBS, and dKO/DIDS—to obtain an improved (i.e., shape-corrected) estimate of the true k_{HbO2} of BCDs (#22) as well as an estimate for P_{M,O_2}. We can apply the appropriate shape-correction factor to individual experiment of protocol (e.g., WT/Ctrl).

Statistical analysis

We report results as mean ± SD. In each relevant figure legend, we report which statistical tests we performed, from among the following, to generate unadjusted *P*-values: (1) paired two-tailed t-test, or (2) one-way analysis of variance (ANOVA). For comparisons of 2 means, we performed #1. For comparisons among >2 means, we performed #2 and then, to control for type I errors across multiple means comparisons, we applied the Holm-Bonferroni correction (Holm, 1979), setting the familywise error rate (FWER) to $\alpha = 0.05$. Briefly, we order the unadjusted *P*-values for all N comparisons in each dataset from lowest to highest. For the first test, we compare the lowest unadjusted *P*-value to the first adjusted α value, α/N. If the null hypothesis is rejected, then we compare the second-lowest *P*-value to the second adjusted α value, α/(N–1), and so on. If, at any point, the unadjusted *P*-value is ≥ the adjusted α, the null hypothesis is accepted and all subsequent hypotheses in the test group are considered null.

Data availability

The data supporting the findings of this study are available within the paper. Any further relevant data are available from the corresponding author upon reasonable request.

Results

In the present study, we use stopped-flow absorbance spectroscopy to monitor Hb deoxygenation as we mix oxygenated RBCs with a solution containing the O_2 scavenger sodium dithionite (final concentration, 25 mM). This NDT protocol virtually eliminates the effect of the EUF on O_2 efflux (Coin & Olson, 1979; Vandegriff & Olson, 1984*b*; Holland *et al.*, 1985). We started by investigating the hypothesis that two small-molecule inhibitors (i.e., pCMBS, DIDS) block hypothetical O_2 channels. After evaluating the effects of genetic deletions of two major membrane proteins (i.e, AQP1, RhAG) on O_2 offloading from RBCs as part of this paper #1, we tested the hypotheses that observed effects on O_2 offloading could reflect changes of RBC geometry or changes in the abundance of major RBC membrane proteins as part of paper #2. Finally, the mathematical simulations in paper #3 provide a quantitative basis for interpreting the data in papers #1 and #2, elucidate the dependence of Hb deoxygenation on membrane O_2 permeability, and support the conclusion that two identified channel proteins as well as a third as-yet-unidentified protein account for nearly all of the O_2 permeability of murine RBCs.

Effect of pCMBS or DIDS on O_2 offloading from RBCs

Stopped-flow approach. As detailed in Methods, our general approach is to mix, in the reaction cell of the SF device, (1) RBCs (Hct ≅ 0.37%) suspended in our oxygenated solution (see Table 2) with (2) a deoxygenated solution containing sodium dithionite at a nominal concentration of 50 mM. In the reaction cell, the NDT, now at a nominal concentration of 25 mM, annihilates the extracellular O_2 in the reaction

$$\underbrace{2Na^+ + S_2O_4^=}_{\text{NDT}} + H_2O + O_2 \rightarrow 2Na^+ + HSO_4^- + HSO_3^- \ .$$

The effect of this level of NDT in eliminating extracellular O_2 is so powerful that it is presumed to virtually eliminate the effect of the EUF ("unstirred layer") on O_2 efflux because $[O_2]_{EUF} \cong 0$ and thus extracellular O_2 has a negligible effect in slowing the net efflux of O_2 from the RBC (Coin

& Olson, 1979; Vandegriff & Olson, 1984*b*; Holland *et al.*, 1985). The transmembrane O_2 gradient now strongly favors O_2 efflux from the RBC (see Figure 2), which in turn leads to the diffusion of free O_2 from the bulk intracellular fluid to the inner face of the membrane. Throughout the cell, the decrease in $[O_2]_i$ promotes the net reaction $HbO_2 \rightarrow Hb + O_2$, which we assess by monitoring the absorbance spectrum of Hb. In parallel, HbO_2 tends to diffuse toward the membrane, and free Hb tends to diffuse in the opposite direction. These processes proceed until no O_2 remains in the cell and all hemoglobin is in the form of free Hb.

Effect of pCMBS on O_2 offloading from RBCs. The 3D graph in Figure 3*A* shows an example of the time course of Hb absorbance spectra (see Methods[45]) of ostensibly intact, control RBCs harvested from WT mice. We refer to these cells as "ostensibly" intact because, although we take care to load into the SF device only what appear to be intact RBCs (*Act%H* ≅ 0.37%; Zhao *et al.*, 2017), we will see that some fraction is lysed in the SF reaction cell; we introduce the accommodation for hemolysis in the next two paragraphs. These are "control" cells because we have not treated them with drugs. In parallel, we pretreat some cells with pCMBS (Figure 3*B*), a sulfhydryl reagent known to inhibit CO_2 diffusion through AQP1, either with AQP1 expressed *Xenopus* oocytes (Cooper & Boron, 1998), or with native AQP1 in human RBCs (Endeward *et al.*, 2006). Figure 3*C* shows a 3D graph for RBCs treated with pCMBS. From the data in Figure 3*A* and *C*, we compute the time courses of relative HbO_2 saturation (see Methods[46]). The records in Figure 3*D* show that pCMBS markedly slows the deoxygenation of Hb within ostensibly intact RBCs. From each such HbSat-vs.-time record, we obtain a "raw" k_{HbO_2} value (see Methods[47]). In the first data row of the blue columns in Table 3*A*, we summarize data for a larger

---

[45] See Methods>Stopped-flow absorbance spectroscopy (workflow #1)

[46] See Methods>Calculation of time course of HbO_2 desaturation (workflow #2)

[47] See Methods>Calculation of raw -k_{HbO_2} (workflow #3)

number of such experiments for paired control vs. pCMBS-treated RBCs. Based on raw values, pCMBS reduces k_{HbO_2} by 57.7%. The associated *P*-value indicates that the effect of pCMBS is statistically significant.

As detailed below[48], we accommodate each raw-k_{HbO_2} value for the small amount of HbO_2 released into the bulk ECF by RBCs that lyse within the SF reaction cell. Because the released HbO_2 deoxygenates more rapidly than HbO_2 surrounded by the RBC membrane, it leads to an overestimate of k_{HbO_2}. Thus, as summarized for ±pCMBS in the second data row of the blue columns in Table 3*A*, both hemolysis-corrected (HC) k_{HbO_2} values are lower than the corresponding raw values. Because the HC-k_{HbO_2} falls more for +pCMBS than for –pCMBS, the % inhibition by pCMBS rises somewhat to 63.2%.

Also as summarized below[49] —and as detailed in paper #3[50] —we additionally accommodate for the appearance of non-biconcave disks, which are rare among control cells but more common with pCMBS-treated and especially DIDS-treated cells. Because the mean diffusion distance is greater (slowing deoxygenation) in nBCDs than in BCDs, the shape-corrected values—summarized in the third data row of the blue columns in Table 3*A*—modestly exceed the corresponding HC-k_{HbO_2} values.

After accommodating for hemolysis and nBCDs, we conclude that pCMBS decreases k_{HbO_2} of intact BCDs by ~61% (Figure 3*E*).

---

[48] See Results>Accommodation for Hemolysis

[49] See Results>Accommodation for nBCDs

[50] See Paper #3>Results>Accommodation for nBCDs

Although pCMBS, with its sulfonate group, was designed to be membrane impermeant, a trivial explanation for the drug effects in Figure 3*D* and *E* is that pCMBS somehow gains entry into the RBC and, directly or indirectly, slows the reaction $HbO_2 \rightarrow Hb + O_2$. To determine whether pCMBS does indeed access the RBC cytosol, we use the RBC's endogenous, cytosolic carbonic anhydrase as a sentinel. Our CA assay is the same one we use for assessing hemolysis (see Methods[51]), namely, mixing two dissimilar CO_2/HCO_3^- solutions (see Table 2) in the SF reaction cell to create an out-of-equilibrium state that favors the reaction: $HCO_3^- + H^+ \rightarrow CO_2 + H_2O$ (↑pH), which is governed by the rate constant $k_{\Delta pH}$. The first bar in Figure 3*F* represents the $k_{\Delta pH}$ of the untreated RBC lysate. The second bar shows that incubating the hemolysate with pCMBS for 15 minutes markedly reduces lysate CA activity. The last two bars show that treating intact RBCs with pCMBS, and then washing, does not significantly affect the $k_{\Delta pH}$ of the subsequent lysate (Figure 3*F*). Thus, we conclude that pCMBS—under the conditions of our experiments—does not significantly cross RBC membranes. Therefore, the ability of pCMBS to decrease k_{HbO2} must reflect the action of the chemical from the extracellular side of the membrane.

Effect of DIDS on O_2 offloading from RBCs. Figure 4*A* shows a representative time courses of Hb absorbance spectra of untreated RBCs, panel *B* shows the structure of DIDS, and panel *C* shows a representative time course of Hb absorbance spectra of DIDS-treated RBCs from WT mice. Figure 4*D* shows time courses of relative HbSat in these experiments, and reveals that DIDS markedly slows O_2 offloading (though not by as much with pCMBS). The first data row of the peach-colored columns of Table 3*A* summarizes paired raw-k_{HbO2} values for a larger number of trials, and shows that DIDS lowers raw-k_{HbO2} by ~33%. The difference is statistically significant.

[51] See Methods>Quantitation of hemolysis in SF reaction cell (workflow #4)

We accommodate these raw-k_{HbO2} values for the Hb released into the bulk ECF by RBCs lysed within the SF reaction cell, using an approach (see below[52]) that is a modification of the one that we employ for control and pCMBS-treated cells. We summarize these HC-k_{HbO2} values in the second data row of peach-colored columns in Table 3*A*. Although hemolysis correction lowers both k_{HbO2} values, it lowers the DIDS HC-k_{HbO2} to a greater extent, so that the DIDS inhibition rises to ~49%.

Finally, after accommodation for nBCDs, we see in the third data row of peach-colored columns in Table 3*A* that SC-k_{HbO2} rises slightly for the control cells but—because DIDS leads to more nBCDs formation—k_{HbO2} rises more substantially for DIDS-treated cells. After accounting for hemolysis and nBCDs, we conclude that DIDS reduces the SC-k_{HbO_2} by ~31% (Figure 4*E*).

To determine whether DIDS accesses RBC cytosol—and because DIDS (unlike pCMBS in Figure 3*F*) has little effect on CA activity (not shown)—we use cytosolic Hb as a sentinel. The left pair of bars in Figure 4*F* shows that incubating an RBC lysate with DIDS substantially reduces k_{HbO_2} of the lysate. However, the right pair of bars reveals no significant effect on k_{HbO_2} if we treat ostensibly intact RBCs with DIDS, then wash off the DIDS and, finally, form the lysate in the absence of DIDS. Thus, DIDS does not significantly cross RBC membranes. We conclude (as we did for pCMBS) that the ability of DIDS to decrease k_{HbO2} is a consequence of an action of the chemical on the extracellular side of the membrane.

Effect of genetic deletions on O_2 offloading from RBCs

Because our data reveal that neither pCMBS nor DIDS crosses RBC membranes to enter the cytosol (Figure 3*F* and Figure 4*F*), and because we are unaware of evidence that either pCMBS

[52] See Results>Accommodation of raw-k_{HbO2} for hemolysis>DIDS-treated RBCs

(Vansteveninck *et al.*, 1965; Rothstein *et al.*, 1973) or DIDS interacts with the lipid component of RBC membranes (Cabantchik & Rothstein, 1974; Moriyama *et al.*, 2015), we reason that pCMBS and DIDS must reduce k_{HbO_2} by inhibiting membrane proteins that conduct O_2.

Effects of single and double knockouts. We begin our search for such proteins by examining the time course of HbSat of RBCs from mice genetically deficient in AQP1 or RhAG, proteins with established roles as major CO_2 channels in human RBCs (Endeward *et al.*, 2006, 2008). Data from representative experiments show that the speed of O_2 offloading from Hb gradually decreases in the order WT > AQP1-KO > RhAG-KO > dKO (Figure 5*A*).

The four colored columns of Table 3*B* summarize raw-k_{HbO_2}, HC-k_{HbO_2}, and SC-k_{HbO_2}—under control conditions (i.e., absence of drugs)—for a larger number of mice, for each of the four genotypes. The magnitudes of the differences from row to row—raw- to HC- to SC-k_{HbO_2}—are rather small because both hemolysis and nBCDs prevalence are rather small. The bar-graph summary in Figure 5*B* shows that the genetic deletion of AQP1 reduces SC-k_{HbO_2} by ~9%. The knockout of RhAG produces a decrease of ~17%, and the double knockout of AQP1 and RhAG lowers SC-k_{HbO_2} by ~30%. Our analysis shows that all six possible comparisons of bars in Figure 5*B* yield statistically significant differences. As summarized below below[53] and detailed in paper #3, our mathematical simulations show that—because RBC dimensions, Hb content and concentrations, and Hb kinetics vary little among the four genotypes—the percent decreases in k_{HbO_2} correspond to far larger decreases in P_{M,O_2}, ~55% in the case of comparing RBCs from WT vs. dKO mice.

[53] See Results> Mathematical simulations

As described in paper #2[54], our proteomic analysis of RBC ghosts, which covers >1100 proteins, shows that the two single knockouts and the double knockout appropriately deplete the membranes of AQP1 and/or RhAG and Rhesus blood group D antigen (RhD). However, the two KOs or the dKO do not significantly affect the inferred abundance of any other RBC proteins among the top-ranked 100. Indeed, only 27 proteins (out of the >1100) exhibit a significant change in one of the KOs or the dKO, and these are proteins with relatively low inferred abundance, often originating from cells other than RBCs per se. Of plasma-membrane–associated (PMA) proteins, the one with the highest inferred abundance to exhibit a significant change is the integrin ITGA2A, which ranked[55] #136 overall and #48 among PMA proteins. Of non-PMA proteins, the highest ranking[56] one with a significant change was PSMA4 (#101 overall). These two proteins had baseline inferred abundances <1% of the top-ranked protein, AE1 (i.e., SLC4A1). We conclude that it is highly unlikely that a change in the expression level of an off-target protein could account for our SC-k_{HbO_2} data.

Combined effects of dKO and pCMBS. We also examined the effect of pCMBS or DIDS on k_{HbO_2} in RBCs isolated from dKO mice. Figure 5*C* contains representative time courses of HbO_2 desaturation for RBCs from a dKO mouse, both under control conditions and after pre-treatment with pCMBS. It shows that O_2 offloading—already lower in RBCs from dKO vs. WT mice—slows even further after pCMBS treatment.

The blue columns of Table 3*C* summarize paired raw-k_{HbO_2}, HC-k_{HbO_2}, and SC-k_{HbO_2} for RBCs from dKO mice, under control vs. pCMBS conditions. The differences are all statistically

---

[54] See Paper #2>Results>Proteomics

[55] See Paper #2>table 10

[56] See Paper #2>table 9

significant. Figure 5*D* shows that, on a dKO background, pCMBS reduces SC-k_{HbO_2} by a further ~68%. Because the dKO by itself produced a ~30% decrease, this additional decrease caused by pCMBS corresponds to a ~78% overall decrease in SC-k_{HbO_2}. Our mathematical simulations below[57] indicate that this ~78% decrease in SC-k_{HbO_2} corresponds to a ~91% decrease in P_{M,O_2}.

Combined effects of dKO and DIDS. As illustrated in Figure 5*E* for representative paired experiments on a dKO background, DIDS slows the time course of HbO_2 desaturation, though not by as much as pCMBS.

The peach-colored columns of Table 3*C* summarize paired raw-k_{HbO_2}, HC-k_{HbO_2}, and SC-k_{HbO_2} for RBCs from dKO mice, under control vs. DIDS conditions. Figure 5*F* shows that, on a dKO background—which by itself reduces SC-k_{HbO_2} by ~30% decrease—DIDS reduces SC-k_{HbO_2} by a further ~32%. This additional decrease caused by DIDS corresponds to a ~53% overall decrease in SC-k_{HbO_2}. Our mathematical simulations below[57] indicate that this ~53% decrease in SC-k_{HbO_2} corresponds to a ~76% decrease in P_{M,O_2}.

Accommodation for Hemolysis

In a previous study in which we used the same methods as in the present one, the fraction of RBCs hemolyzed was ~0.37% before they enter the SF device, but ~5% while the cells were in the SF reaction cell (Zhao *et al.*, 2017). This increase presumably reflects the susceptibility of a subfraction of RBCs to the stress of the SF procedure, resulting in cell lysis and the release of Hb and HbO_2 into the bECF. We hypothesize that this released HbO_2 (because the RBC membrane does not separate it from the NDT): (1) deoxygenates faster than the HbO_2 within intact RBCs, leading to (2) an overestimate of k_{HbO_2}. If RBCs treated with inhibitors or isolated from KO mice

[57] See Results> Mathematical simulations

have an increased degree of hemolysis, we would underestimate the degree of inhibition. Therefore, for each RBC preparation from each mouse, we assay hemolysis as outlined in Methods[58].

Hemolysis measurements

Effect of drug treatments on hemolysis. Figure 6*A* schematically illustrates our approach for assessing hemolysis within the SF reaction cell (Zhao *et al.*, 2017). Figure 6*B* schematizes this approach to control cells (i.e., no drugs); Figure 6*C*, to pCMBS-treated cells (i.e., pCMBS); and Figure 6*D*, to DIDS-treated cells (i.e., DIDS). Our analysis of hemolysis shows that, compared to WT/Ctrl RBCs (~5.2% hemolysis), those pretreated with pCMBS (~8.2%) or DIDS (~13.4%) exhibited a significant increase (Figure 6*E*). Note that we accommodate for hemolysis, as described below[59].

Effect of channel knockouts on hemolysis. Our analysis of the two KO sub-strains and the dKO reveal no significant difference in hemolysis compared to the WT (Figure 6*F*). These results are consistent with the report that deletion of *Rhd* and *Rhag* do not increase RBC fragility (Goossens *et al.*, 2010).

Among RBCs from dKO mice, we find that pretreatment with pCMBS or DIDS—as was the case for RBCs isolated from WT mice—produce significant increases in hemolysis (Figure 6*G*). Moreover, pCMBS and DIDS produce somewhat greater degrees of hemolysis on the dKO background (Figure 6*G*) than on the WT background (Figure 6*E*). Note that we accommodate for hemolysis, as described immediately below.

---

[58] See Methods>Quantitation of hemolysis in SF reaction cell (workflow #4)

[59] See Results>Accommodation for hemolysis>Accommodation of raw-k_{HbO_2} …

Accommodation of raw-k_{HbO2} for hemolysis

We have developed two variants of a novel approach to accommodate for hemolysis in the SF reaction cell. The first variant applies to cells that are either not treated with a drug (i.e., controls) or those pretreated with an agent(s) that does not appreciably affect the rate of the extracellular reaction $HbO_2 \rightarrow Hb + O_2$. The second variant applies to experiments in which the agent(s) (e.g., DIDS) does significantly affect this reaction.

Control or pCMBS-treated RBCs. Figure 7*A* shows the result of applying this approach (as illustrated in Figure 6*A* and *B*) to a representative control experiment (i.e., no drugs) on RBCs from a WT mouse. In this figure, the blue x-axis is the apparent hemolysis, whereas the green x-axis is the actual hemolysis, measured as described in Methods[60]. One might unwittingly assume that the *Act%H* in SF reaction cell is 0% (i.e., 100% of RBCs are ostensibly intact), and thus believe that the measured raw-k_{HbO2} of 3.70 s^{-1} (the value in step #3 of Figure 1) in this experiment is in fact the actual k_{HbO2} (although not yet shape corrected). However, the hemolysis assay in this example shows that *Act%H* is in fact 4.4% (shown on the green x-axis). To determine the actual k_{HbO2} when *Act%H* truly is 0%, we mix 100% ostensibly intact RBCs (*Act%H* ≅ 4.4%) with 100% hemolyzed RBCs (*Act%H* = 100%) in increasing ratios, as shown by the blue points in Figure 7*A*. When we reference these blue points to the blue x-axis, we obtain a regression line that describes apparent raw-k_{HbO2} vs. *App%H*, with a slope of ~5.5256 s^{-1}/%*H* and a y-intercept (i.e., the raw-k_{HbO2}) of ~3.70 s^{-1} on the blue axes. To reference these same blue points to the green x-axis, we scale the x-axis and the slope of the regression line by the factor

$$scaling\ factor = \left(\frac{100\%}{100\% - (Act\%H)_{App\%H=0}}\right) \approx \left(\frac{100\%}{100\% - (\sim 4.4\%)}\right) \approx 1.04566\,.$$

[60] See Methods>Quantitation of hemolysis in SF reaction cell (workflow #4)

We also translate the green x-axis so that the measured *Act%H* (i.e., ~4.4%) lines up with the *App%H* of 0% on the blue x-axis. We calculate actual k_{HbO2} by back-extrapolating the regression line—now referenced to the scaled/translated green axes—to *Act%H* = 0. As illustrated in Figure 7*A*, here the y-intercept is ~3.45 s^{-1}, which represents the hemolysis-corrected k_{HbO2} (the value in step #5 of Figure 1). As we will see at the end of Results, the further correction of these RBCs for shape yields a SC-k_{HbO2} of 3.48 s^{-1} (the value in step #22 of Figure 1).

We apply the above approach to the pCMBS-treated cells as schematized in Figure 6*C*, and exemplified in Figure 7*B*. Indeed, we performed the hemolysis accommodation, as in Figure 7, for all experiments, except those for cells pretreated with DIDS—as discussed next.

DIDS-treated RBCs. As noted in Methods[61], for two reasons we must approach the accommodation for hemolysis somewhat differently in DIDS-pretreated RBCs than in control or pCMBS-treated cells. First, in 100%-hemolyzed RBCs, a 1-h pretreatment with DIDS markedly (~85%) reduces k_{HbO_2} (compare green and gray-blue bars in Figure 8*A*. The large difference in bar heights is relevant for RBCs as we load them into the SF device, when the fraction of hemolyzed cells is minute (i.e., *Act%H* ≅ 0.37%; see Zhao *et al.*, 2017), but the duration of drug exposure is sizeable. Second, during the actual SF experiment—and on a ms-to-s time scale—DIDS produces only a small (~4%) reduction in k_{HbO_2} (compare green and gray-blue open bars in Figure 8*B*). In this case, although the fractional inhibition is small, the fraction of Hb newly released in the SF reaction cell is much larger.

[61] See Methods>Accommodation for hemolysis (workflow #5)>DIDS-treated RBCs

In the control RBCs in Figure 8*C*, the approach for obtaining the regression line is the same as in Figure 7*A*. Figure 8*C* shows the $k_{\mathrm{HbO_2}}$ hemolysis correction for RBCs—from 1 mouse—studied under control conditions (i.e., no DIDS). Here, $Slope_{\mathrm{Ctrl,Act}}$ is 6.51 $\mathrm{s}^{-1}/Act\%H$.

For the DIDS-treated cells in Figure 8*D*, we use a novel approach to obtain the regression line. In Methods, Eqn (1) describes (without a numerical example) the actual slope of this regression line. For RBCs from the same mouse as in Figure 8*C*, but treated ×1 h with 200 μM DIDS before entry into the SF device, the *Act%H* is 12.7% in the SF reaction cell. Inserting these %*H* values for this mouse—and the average k_{HbO2} for 7 mice in Figure 8*A*–*B*—into Eqn (1) yields

$$Slope_{\mathrm{DIDS,Act}} = \underbrace{6.511\frac{\mathrm{s}^{-1}}{Act\%H}}_{Slope_{\mathrm{Ctrl,Act}}} \cdot \underbrace{\left[\underbrace{\underbrace{\frac{1.85\,\mathrm{s}^{-1}}{14.71\ \mathrm{s}^{-1}}}_{0.12576} \cdot \underbrace{\frac{0.37\%}{12.7\%}}_{0.031496}}_{0.00396} + \underbrace{\underbrace{\frac{13.52\ \mathrm{s}^{-1}}{14.03\ \mathrm{s}^{-1}}}_{0.96365} \cdot \underbrace{\frac{12.7\% - 0.37\%}{12.7\%}}_{0.96850}}_{0.933298}\right]}_{0.937259} = 6.114\frac{\mathrm{s}^{-1}}{Act\%H}.$$

Note that although this slope correction[62] amounts to only 100% – (~93.7%) = ~6%, it affords improved accuracy and shows that potential errors are not likely to be large. As summarized in Figure 8*D*, for this particular mouse[63]

$$k_{\mathrm{HbO_2DIDS,Act}} = 2.348\,\mathrm{s}^{-1} - \left(6.114\frac{\mathrm{s}^{-1}}{Act\%H}\right)\cdot\left(12.7\%\,Act\%H\right) = 1.57\,\mathrm{s}^{-1}.$$

---

[62] Evaluating the above equation, as written, yields 6.11538, as opposed to 6.114. The discrepancy is due to rounding errors in the written equation.

[63] Evaluating the above equation, as written, yields 1.56, as opposed to 1.57. The discrepancy is due to rounding errors in the written equation.

Hematological and related parameters

We present the details of the macroscopic mathematical model as well as simulations of O_2 offloading in paper #3. In the present paper, below[64], we summarize elements of this MMM that are of particular relevance to the present paper. It is perhaps intuitively obvious that k_{HbO_2} should decrease with (1) increases in MCV (due to increased diffusion distances) and (2) increases in MCHC (due to increased interactions between O_2 and Hb that slow effective O_2 diffusion), and (3) with decreased kinetics of HbO_2 dissociation. To evaluate potentially trivial explanations for the decreases in k_{HbO_2} observed in Figure 3, Figure 4, and Figure 5, we performed a series of hematological, morphometric, and HbO_2 kinetics studies.

Automated hematology

Effect of KOs. We performed a battery of assays (see Methods[65]) on the fresh blood of a large subset of mice used in the present study. In the largest group of such studies, we examined all four genotypes (Table 4). Because we observe no significant sex-related differences, we grouped the data from male and female mice (M+F). The only genotype-related differences that reach statistical significance are with RBCs from RhAG-KO and dKO mice, which for M+F exhibit slightly higher mean values for RDWa and MCV, but slightly lower values for MCHC.

The slightly higher RDWa values may correlate with the trend for KO mice, particularly RhAG-KO and dKO, to have higher percentages of reticulocytes (see paper #2[66]).

---

[64] See Results>Mathematical simulations

[65] See Methods>Automated hematological analyses (workflow #7 – #9)

[66] See (a) Paper #2>table 2 … & … (b) ..>figure 6*e*

Regarding the increased MCV but decreased MCHC values, our mathematical simulations indicate that these effects tend to cancel (paper #3[67]). The bar graphs in Figure 9 summarize the most pertinent automated hematology data, including those with statistically significant differences (see Figure 9*C*, *E*, *F*).

Effects of inhibitors. For hematological studies with inhibitors (see Methods[68]), we generated preparations of RBCs from WT and dKO mice, and then pretreated these with no drug, pCMBS, or DIDS—a total of six conditions ([WT vs. dKO] × [control vs. pCMBS vs. DIDS]). Most of the statistically significant effects (Table 5) involve white blood cells or platelets, which the drugs generally tend to reduce in number. The effects on RBCs mainly involve MCV and MCHC, and these effects—as noted in the previous paragraph—are almost always in the directions that would tend to cancel vis-à-vis k_{HbO_2}.

The RBCs summarized in Table 5 include those blood samples that we used for the IFC studies in paper #2[69].

Morphometry

Blood smears. In paper #2[70], we present two sets of blood-smear data. In the first, we examined control cells (i.e., those not exposed to pCMBS or DIDS) of all four genotypes. The pathologist read the RBC morphology (see paper #2[71]) as "unremarkable, demonstrating only

---

[67] Paper #3>Results>Mathematical simulations…>$Ø_{Sphere}$>Tendency of MCHC and MCV effects to cancel

[68] See Methods>Automated hematological analyses (workflow #7 – #9)>Use of inhibitors in automated hematological studies

[69] See Paper #2>table 6

[70] See Paper #2>Results>Morphometry>Blood smears

[71] See Paper #2>figure 2

occasional target cells and stomatocytes, with no differences noted among knockout strains and WT mice."

In the second set of blood-smear data, we examined blood from (1) WT or (2) dKO mice pretreated with (a) neither pCMBS (controls), (b) with pCMBS, or (c) with DIDS (i.e., a total of 2 × 3 = 6). The pathologist read the RBC morphology (see paper #2[72]) as showing "no significant differences in red cell morphology … under any of the [six] conditions." The absence of a comment about increased nBCDs prevalence in the drug-treated cells in the blood smears (where we plate, stain, and dry the cells after drug pretreatment) is interesting, inasmuch as nBCDs were apparent in images of living, tumbling RBCs or RBCs visualized by IFC. On the other hand, we made the blood smears immediately after drug treatment (e.g., <5 min), whereas the delays between drug treatment and live-cell imaging (see below[73]) were as long as 90 min.

Living RBCs tumbling through the focal plane of an inverted microscope. In paper #2, we also examine RBCs in suspension as we drop them onto a coverslip on the stage of an inverted microscope, and then image the cells as they fall through the focal plane (paper #2[74]). For control RBCs (no inhibitors present) of all four genotypes, the RBCs appear as normal biconcave disks, with occasional (~1.35%) poikilocytes, both in still images (see paper #2[75]) and video recordings (see paper #2[76]).

---

[72] See Paper #2>figure 3

[73] See (1) Results>Hematological and related parameters>Morphometry>Living RBCs tumbling through the focal plane of an inverted microscope … & … (2) ..> Living RBCs visualized using imaging flow cytometry (IFC)

[74] See Paper #2>Results>Morphometry>Imaging of living, tumbling RBCs

[75] See Paper #2>figure 4

[76] See Paper #2>Supporting Information

In a second set of studies, we similarly examined RBCs—untreated, pretreated with pCMBS, or pretreated with DIDS—from WT or dKO mice. Whereas the appearance of the control RBCs (no inhibitor) was again unremarkable, we observed spherical cells (sometimes with spicules)—"nBCDs"—in the pCMBS experiments, and more so in the DIDS experiments (see paper #2[77]).

Light-scattering flow cytometry. As presented in paper #2[78], these studies—which included the development of gating schemes (based on staining with fluorescent markers) to distinguish various cell types—showed that RhAG-KO and dKO mice tend to have slightly larger and more varied RBC sizes compared to WT and AQP1-KO mice. However, the overall differences in cell size and shape among the genotypes were not significant.

Living RBCs visualized using imaging flow cytometry (IFC). In a fourth and final approach for assessing RBC morphometry—and as presented in paper #2[79]—we establish gating schemes and then obtain photographs of single cells as they fly before a microscope objective.

Cell shape. We found that even control (not treated with inhibitors) RBCs from WT and dKO mice have ~2% nBCDs (see paper #2[80]). After pretreatment with pCMBS, the fraction increased significantly for the WT (~8.7%) but less so in the dKO (~5.7%). The pattern was the same following DIDS pretreatments, except that the fraction of nBCDs was far higher (41% for

---

[77] See Paper #2>figure 5

[78] See Paper #2>Results>Morphometry>Light-scattering flow cytometry

[79] See Paper #2>Results>Morphometry>Imaging flow cytometry

[80] See (a) Paper #2>figure 8*b–c* … & … (b) ..>table 5

WT vs. 21% for dKO). The presence of nBCDs, particularly after drug pretreatment, led us to develop a novel approach to accommodate for these effects, as summarized below[81].

As mentioned above, the time delays between completion of drug treatment and live-cell imaging (both DIC microscopy and IFC) were as long as 90 min, vs. the <5 min delay before either SF or preparation of blood smears.

The decrease in nBCD prevalence—both for samples pretreated with pCMBS or with DIDS (see previous paragraph)—in dKOs vs. WTs is consistent with the hypothesis that the drug-induced shape changes depend, at least in part, on interactions of the drugs with AQP1 and/or Rh_{Cx}.

Major RBC diameter ($Ø_{Major}$). The IFC experiments not only identify cell shape, but also provide—for cells with the proper orientation—the major diameter of BCDs and of nBCDs (see paper #2[82]). These values are an important input to the mathematical simulations (see below[83]).

Hb kinetics ($k_{HbO_2 \rightarrow Hb+O_2}$)

To examine the possibility that the knockout of one or both channels could affect the kinetics of HbO_2 dissociation per se, we determined the rate constant of the reaction $HbO_2 \rightarrow Hb + O_2$ in 100% hemolyzed RBCs. The approach was the same as for 100% ostensibly intact RBCs (see Figure 3 and Figure 4), or for various mixtures of 100% ostensibly intact and 100% hemolyzed RBCs (see Figure 7 and Figure 8). On the one hand, we find no significant differences among the mean $k_{HbO_2 \rightarrow Hb+O_2}$ values for WT, AQP1-KO, RhAG-KO mice (Figure 10). However, we are

---

[81] See Results>Accommodation for nBCDs

[82] See Paper #2>table 5

[83] See (a) Results>Mathematical simulations … & … (b) ..>Accommodation for nBCDs

somewhat surprised—inasmuch as the individual AQP1 and RhAG deletions were without effect—that the dKO produced a ~9% decrease of $k_{HbO2 \rightarrow Hb+O2}$ (i.e., 100% lysate).

Because the reaction $HbO_2 \rightarrow Hb + O_2$ is only one of several processes that contribute to k_{HbO2}, intuition tells us that the ~9% decrease in $k_{HbO2 \rightarrow Hb+O2}$ should account for even a smaller fraction of the ~30% decrease that we observed in dKO mice. Indeed, the sensitivity analysis in paper #3[84] indicates that a 9% decrease in $k_{HbO2 \rightarrow Hb+O2}$ would, by itself, lower k_{HbO2} by only 1.5%. Viewed differently, in order to account, by itself, for the 30% decrease in k_{HbO2} observed in physiological experiments, $k_{HbO2 \rightarrow Hb+O2}$ would have to fall by ~63%.

Mathematical simulations

Overview. Our goal in the macroscopic mathematical modeling and simulations is not to adjust simulation parameter values to produce a MMM-k_{HbO2} (i.e., the simulated value) that matches the observed raw-k_{HbO2} (e.g., the control curve for WT RBCs in Figure 3*C*), but rather to predict—from first principles—the time course of hemoglobin desaturation (see paper #3[85]). The numerical inputs for our simulations (see paper #3[86]) are physical constants and other values taken from the literature[87] as well as genotype-specific values[88] generated in the present paper and paper #2. Among the literature values, we took P_{M,O_2} to be 0.15 cm s^{-1} (Figure 1, workflow #13), the measured value of P_{M,CO_2} of Endeward *et al.* in human RBCs (Endeward *et al.*, 2006). For the thickness of the unconvected layer, we chose 1 μm, which (given the high level of NTD in our

---

[84] See Paper #3>figure 8

[85] See Paper #3>Introduction

[86] See Paper #3>Methods>Mathematical modeling and simulations>Parameter values

[87] See Paper #3>table 1

[88] See Paper #3>table 2

experiments) may be an overestimate (Holland *et al.*, 1985). Among genotype-specific values, the $Ø_{Major}$ (workflow #6 and #6′, from paper #2[89]) and MCV (workflow #8 from paper #2[90]) are inputs for computing BCD thickness (workflow #10). MCH (workflow #7) as well as MCV (workflow #8) together yield MCHC (workflow #9). In the next major section, we summarize accommodations for nBCDs that yield shape-corrected values for k_{HbO2}.

Summary. The result of our simulation for control WT RBCs (i.e, without inhibitors)—all cells assumed to be 100% intact BCDs—is an MMM-k_{HbO2} of ~3.99 s^{-1} (workflow #14; see paper #3[91]). For the data set summarized in Figure 3*E*, the mean SC-k_{HbO2} value underlying the control/WT value (darker green bar) is 3.45 s^{-1}. For the (different) data set summarized in Figure 4*E* (green bar), the comparable value is 3.24 s^{-1}, and for Figure 5*B* (green bar), the value is 4.09 s^{-1}. Thus, our MMM-k_{HbO2} value determined from first principles—3.99 s^{-1}—ranges from ~2.5% lower than the highest SC-k_{HbO2} value to ~23% higher than the lowest value. We conclude that the MMM simulation provides a reasonable estimate of HbO_2 desaturation under the conditions of our experiments.

---

[89] See Paper #3>table 5

[90] See Paper #3>table 4

[91] See Paper #3>Results>Simulations of O_2 efflux from a control RBC of WT mouse

Accommodation for nBCDs

Because it appears that all RBC preparations contain at least a small fraction of nBCDs, we developed a novel linear-combination method to accommodate for the presence of nBCDs (for summary, see Methods[92]; for detailed account, see paper #3[93]). This procedure, which corrects for the presence of "slower" nBCDs (lower k_{HbO_2}) amidst the "faster" BCDs (higher k_{HbO_2}), raises a hemolysis-corrected k_{HbO_2} value (e.g., our standard value of ~3.99 s^{-1}) to the corresponding shape-corrected value (i.e., ~4.04 s^{-1} in this example). We can then compute a shape-correction factor $\mathcal{F}_{SC}$ (i.e., ~ 4.04/3.99 ≅ 1.01), and apply it to any experiment on WT/Ctrl RBCs. Thus, if RBCs of the particular mouse exemplified in Figure 1 and Figure 7*A* have a raw-k_{HbO_2} of 3.70 s^{-1} (step #3 in Figure 1) and an HC-k_{HbO_2} of 3.45 s^{-1} (step #5), the linear-combination accommodation will yield an SC-k_{HbO_2} of ~3.48 s^{-1} (step #22). This shape-correction factors is small with control RBCs (WT or various KOs) but becomes larger with pCMBS and especially DIDS.

---

[92] See Methods>Accommodation for nBCDs (workflow #13, #14 & #14′, #16 – #22)

[93] See Paper #3>Results>Accommodation for non-BCDs

Discussion

Overview

The combined results of the present paper and its two companion papers show that two channel proteins—AQP1 and the Rh complex—contribute ~55% of the O_2 permeability to murine RBCs. On the background of the AQP1/Rh_{Cx}-dKO, we estimate that other protein(s) blocked by DIDS contribute an additional ~21% of P_{M,O_2}, whereas proteins blocked by pCMBS contribute ~36%. If the DIDS-sensitive proteins (~21%) are fully a subset of the pCMBS-sensitive ones (~36%), then at least ~91% of murine RBC O_2 traffic occurs via membrane channels under the conditions of our experiments. To the extent that a subset of DIDS-sensitive proteins in the dKO are not also pCMBS sensitive, the contribution of unidentified channels would be greater than ~36%, and the full collection of O_2 channels would account for even more than ~91% of O_2 traffic in mice under the conditions of our experiments.

Implications of O_2 and CO_2 channels. Together with earlier CO_2 studies, the present work shows that, of the O_2 and CO_2 traffic across mammalian RBC membranes, at least 90% occurs through protein channels. Our work raises questions that should trigger new lines of research: What is the molecular mechanism of O_2 diffusion through the channels? We suggest that the most likely routes are the hydrophobic central pores at the middle of the AQP1 tetramers and Rh trimers, and/or other hydrophobic pathways between monomers. Which other membrane proteins contribute to P_{M,O_2} in RBCs? And to what extent do AQPs, Rh proteins, and other membrane proteins contribute to O_2 permeability in other cell types? An important implication of our O_2-channel work is that it provides a mechanism for cellular regulation of O_2 permeability by controlling the synthesis/trafficking of these channels, or by using post-translational modifications or protein-protein interactions to modulate single-channel permeability. Our work raises the possibility of O_2-channelopathies in human disease. Finally, the O_2-channel paradigm offers the future physician the possibility of raising O_2 permeability (e.g., to enhance performance or wound

healing) or lowering O_2 permeability (e.g., to treat oxygen toxicity) by altering the (1) number or (2) intrinsic permeability of channels.

The Krogh cylinder. A century ago, Krogh (1919) performed a mathematical analysis of O_2 off-loading from RBCs, which included not only dissociation of O_2 from HbO_2, but also the diffusion of O_2—lumped as a single process—through RBC intracellular fluid, across the RBC membrane to the bulk extracellular fluid of systemic capillary blood plasma, and then across the capillary endothelium, ultimately to the ICF of O_2-metabolizing cells (see paper #3[94]).

At the time, Krogh's analysis was a *tour de force* that blended state-of-the-art experimental physiology with mathematics. This mathematical approach, in the days before digital computational methods, required numerous simplifying assumptions to yield equations amenable to analytical solutions. Without these simplifying assumptions, Krogh's quantitative model—with its demonstrated great value to physiology—would have been impossible. Sixty years after Krogh, Kreuzer (1982) enumerated 15 implicit assumptions in the Krogh analysis, one of which implies that the RBC membrane offers no resistance to O_2 diffusion (i.e., $R_{M,O_2} = 0$). Whether or not Krogh himself would have agreed that R_{M,O_2} is, in fact, greater than 0, we suggest that his implicit assumption (i.e., $R_{M,O_2} = 0$) was a reasonable first step inasmuch as it enabled a mathematical analysis that provided the first quantitative insights into the Krogh cylinder. Nevertheless, this implicit assumption became dogma for at least a subset of physiologists. The present work, as discussed below[95], proves that the implicit assumption is incorrect.

Overton's rule. A larger subset of physiologists have adhered to a very different idea: Overton's rule (a subset of the broader, previously proposed solubility-diffusion theory), which

---

[94] See Paper #3>Discussion>Krogh-Erlang Equation

[95] See Discussion>Implications of the macroscopic mathematical model> Predictions for effects on P_{M,O_2}

holds that the diffusion of substances across membranes depends exclusively on their solubility in the lipid phase of the membrane. At the time of Overton, the concept of a membrane protein's mediating transport across a membrane would have been entirely foreign. For most of the panoply of substances that cross cell membranes—water, inorganic ions, small molecules, and even large substances like fatty acids and prostaglandins—Overton's rule has long-since been abandoned in favor of channels and various transport proteins (for review, see Aronson *et al.*, 2017). The present work with the knockout and blockade of channels (see below[95])—together with previous work from this and other laboratories (Waisbren *et al.*, 1994; Nakhoul *et al.*, 1998; Cooper & Boron, 1998; Uehlein *et al.*, 2003, 2008, 2012*a*, 2012*b*; Endeward *et al.*, 2006, 2008; Musa-Aziz *et al.*, 2007*b*, 2025; Geyer *et al.*, 2013*b*, 2013*a*, 2013*c*; Nakhoul & Hamm, 2014; Wang *et al.*, 2016, 2025; Zwiazek *et al.*, 2017)—provides further evidence that the narrow view, attributed by others to Overton, does not hold universally for dissolved gases. Rather, P_{M,O_2} in murine RBCs depends largely (~90%) on the presence and activity of at least three membrane proteins: AQP1, Rh_{Cx}, and at least one unidentified protein.

Automated hematology experiments

Our hematology assays (see Table 4 and Figure 9) did not reveal substantial differences among RBCs from mice of different genotypes, or of RBCs from WT or dKO mice treated with drugs. The critical values from the present paper for the mathematical simulations are MCV, MCH, and the derived MCHC (MCHC = MCH/MCV), all of which we passed along to paper #3 for simulations. As mentioned above and discussed in detail below[96], the KO-specific changes in

[96] See Discussion>Implications of the macroscopic mathematical model>Effect of channel knockouts on MCV and MCHC

MCV and MCHC tend to cancel out, leading to the conclusion that automated-hematology data cannot account for the genotypic effects on k_{HbO_2}.

In parallel with the two critical hematological parameters (MCV and MCHC), major diameter and nBCD prevalence pass in parallel from paper #2 to paper #3, providing the final values required for the mathematical simulations and accommodations.

Stopped-flow experiments

Hemolysis. We developed our SF hemolysis assay (Zhao *et al.*, 2017), which is based on the release of CA from RBCs into the extracellular fluid, because we anticipated that some RBCs lyse within the SF reaction cell and thereby lead to an overestimate of k_{HbO_2}. In the present paper, we develop what we believe are the first approaches (Figure 7 and Figure 8) for accommodating for the hemolysis that must always be occurring during SF studies. In brief, we artificially create precise degrees of incremental hemolysis, measuring k_{HbO_2} at each. As predicted, k_{HbO_2} rises as apparent hemolysis rises. After a rescaling and translation to create an x-axis that represents actual hemolysis, a back-extrapolation yields the true k_{HbO_2} when actual hemolysis should be zero. Because this hemolysis-corrected k_{HbO_2} is always less than the raw-k_{HbO_2}, the fractional inhibition based on raw-k_{HbO_2} values will underestimate those based on HC-k_{HbO_2} values.

In the case of control RBCs (not treated with a drug), these hemolysis corrections are modest, in the range of 4.0% to 7.0% for WTs, ~3.4% for AQP1-KOs, ~5.3% for RhAG-KOs, and ~9.8% to ~10.7% for dKOs (see Table 3). For drug-treated cells, the hemolysis corrections are larger, ~17% (pCMBS) and ~25% (DIDS) for WTs and 41% (pCMBS) and 33% (DIDS) for dKOs. The drug values are larger than their control counterparts because (1) the actual % hemolysis is larger than for control cells (see Figure 6) so that the extrapolation is somewhat greater and (2) drug-treated cells have lower raw-k_{HbO_2} values so that even the same absolute hemolysis correction produces a greater fractional change.

Non-biconcave disks (nBCDs). We developed our accommodation for nBCDs because we observed them in DIC images of living drug-treated RBCs (see paper #2[97]). Imaging flow-cytometry confirms that nBCDs—a mixture of poikilocyte types (mainly echinocytes, acanthocytes, and spherocytes)—appear in all of our preparations (see paper #2[98])—at least after the prolonged times needed to execute these assays. The prevalence (see paper #2[99]) was very low in control RBCs from WT and dKO mice (~2%), larger with pCMBS pretreatment (~9% in WT, falling to ~6% in dKOs), and high in DIDS-treated cells (~41% in WT, falling to ~21% in dKOs). Because the delay between drug treatment and IFC experiments is greater (~30 to 90 min) than between drug treatment and SF experiments or preparation of blood smears (~5 min), the nBCD prevalence from IFC studies probably overestimates the actual prevalence in SF studies, and thus probably leads to underestimates of the true drug effects on P_{M,O_2}.

To our knowledge, our IFC study is the first quantitative search in physiological experiments for nBCDs, which nevertheless were presumably present in previous studies. In future studies, it would be valuable to determine the interrelationships among (1) drug concentration and exposure time, (2) decrease in P_{M,O_2}, and (3) nBCDs prevalence, with the goal of determining protocols that maximize inhibition while minimizing nBCDs formation.

In the present study, we accommodated for nBCDs by (1) using IFC data to obtain diameter and prevalence, (2) assuming that the nBCDs are spheres, (3) assuming that membrane properties (e.g., P_{M,O_2}) and MCH (i.e., total amount of Hb/cell) are the same in BCDs and nBCDs, (4) using our mathematical simulations to make a provisional estimate of the k_{HbO2} of nBCDs (always lower

---

[97] See Paper #2>figure 5

[98] See Paper #2>figure 8*b*–*c*

[99] See Paper #2>table 5

than for BCDs), and (5) applying our linear-combination approach (see paper #3[100]) to extract the k_{HbO_2} for BCDs (always higher than HC-k_{HbO_2}).

Note that although we assume that nBCDs are perfect spheres (minimal surface/volume ratio, slowest HbO_2 offloading), in fact nBCD surface geometry is often more complex (higher surface/volume, faster offloading). Thus, our k_{HbO_2} of nBCDs probably tends to be an underestimate, so that our linear-combination approach tends to over-correct and yield a deduced k_{HbO_2} of BCDs—the SC-k_{HbO_2}—that overestimates the true k_{HbO_2} of BCDs. As a result, when computing fractional inhibition, we tend to underestimate very slightly the effect of channel KOs under control (i.e., drug-free) conditions, and underestimate more substantially the inhibition produced by pCMBS and particularly DIDS.

In the case of control RBCs (not treated with a drug), both WT and KO, the shape-change correction factors—probably slight overestimates both because of the likelihood of our overestimating nBCD prevalence and underestimating nBCD surface-to-volume ratio of nBCDs—are small, $\mathcal{F}_{SC} \cong 1\%$. In the case of drug-treated cells, the $\mathcal{F}_{SC}$ values (probably greater overestimates) are larger, ~6% for pCMBS and ~35% for DIDS. To the extent that we overestimated $\mathcal{F}_{SC}$, we underestimated the inhibitory effects of the drugs, and underestimated the total fraction of transmembrane O_2 traffic attributable to membrane proteins under the conditions of our work. Thus, this fraction could well exceed our 91% estimate.

Overall assessment of accommodations. For control RBCs of all genotypes, the rate of hemolysis is small (*Act%H* ≅ 5%; see Figure 6*F*), the k_{HbO_2} correction for hemolysis is

[100] See Paper #3>Results>Accommodation for non-BCDs>Linear combination of hemoglobin-deoxygenation time courses

similarly small (~4% to ~6%; see Table 3*B*), nBCDs prevalence is low (~2%; see paper #2[101]), and the additional correction for nBCDs is similarly small ($\mathcal{F}_{SC} \cong 1\%$; see Table 3*B*). We regard both our hemolysis assay and hemolysis correction as robust. Even so, the correction is likely to be most reliable with low *Act%H*. The shape-change correction is likely most reliable with low nBCD prevalence. Thus, we have our highest degree of confidence in our control data on RBCs from WT, AQP1-KO, RhAG-KO, and dKO mice—that is, the dKO likely reduces P_{M,O_2} by a substantial amount (best estimate ≅ 55%; see paper #3[102]).

pCMBS. For WT and dKO cells pretreated with pCMBS, hemolysis is still modest (*Act%H* ≅ 8% and 11%, respectively; see Figure 6*E* and *G*), the k_{HbO2} hemolysis correction is modest to large (about –30% and –41%, respectively; see Table 3*A* and *C*), nBCDs prevalence is modest to small (~9% and ~6%, respectively; see paper #2[101] and the correction for nBCDs is small (about +6% for WT, +4% for dKO; see Table 3*A* and *C*). In our favor, the hemolysis and shape corrections are in opposite directions. Thus, we are confident that, in RBCs from WT mice, pCMBS substantially reduces both k_{HbO2} (best estimate ≅ 61%; see Figure 3*E* and paper #3[102]) and P_{M,O_2} (best estimate ≅ 82%; see paper #3[102]). On a dKO background, we have greater confidence (because of a smaller $\mathcal{F}_{SC}$) that pCMBS produces a further decrease in k_{HbO2} beyond the dKO effect (best estimate ≅ 68%; see Figure 5*D*). Thus, we are confident that the combination of dKO and pCMBS produces an even-larger total reduction in k_{HbO2} (best estimate ≅ 78%; see Figure 5*D* and paper #3[102]). This last value translates to a maximal reduction in P_{M,O_2} of ~91% (see paper #3[102]).

DIDS. WT and (to a lesser extent) dKO cells pretreated with DIDS are the most problematic in the present study. Hemolysis is rather high (*Act%H* ≅ 13% and 15%, respectively;

---

[101] See Paper #2>table 5

[102] See Paper #3>table 3

see Figure 6*E* and *G*), the k_{HbO2} hemolysis corrections are high (about –31% and –33%, respectively; see Table 3*A* and *C*), nBCD prevalences are high (~41% and ~21%, respectively; see paper #2[101]), and the correction for nBCDs is high (about +35% for WT, +16% for dKO; see Table 3*A* and *C*). The corrections are large, but they are similar in magnitude but opposite in direction. As a result, we are confident that, in RBCs from WT mice, DIDS reduces both k_{HbO2} (best estimate ≅ 31%; see Figure 4*E* and paper #3[102]) and P_{M,O_2} (best estimate ≅ 56%; see paper #3[102]). On a dKO background, we have somewhat greater confidence (again, because of a smaller $\mathcal{F}_{SC}$) that DIDS produces a further decrease in k_{HbO2} beyond the dKO effect (best estimate ≅ 32%; see Figure 5*F*). Thus, we are confident that the combination of dKO and DIDS produces an even-larger total reduction in k_{HbO2} (best estimate ≅ 53%; see Figure 5*F* and paper #3[102]). This last value translates to a maximal reduction in P_{M,O_2} of ~76% (see paper #3[102]).

Although we believe that our data show that DIDS blocks a major component of P_{M,O_2} in murine RBCs under the conditions of our experiments, we appreciate that one might be concerned that DIDS-treated RBCs have a rather high values for *Act%H* and a nBCD prevalence—even if we have attempted to accommodate for these effects. Nevertheless, even if we were to ignore the DIDS data in the present paper, we would still come to the conclusion that the dKO reduces P_{M,O_2} by ~55%, and that pCMBS blocks an additional ~36%, to take the total protein-mediated component of P_{M,O_2} to at least ~91%.

Mechanism of drug action. Our work shows that neither pCMBS (see Figure 3*E*) nor DIDS (Figure 4*E*) gains significant entry to the RBC cytosol. Thus, the effects of pCMBS (a sulfhydryl reagent) and DIDS (an amino-reactive agent) must be at the level of the exterior surface of the plasma membrane. Other authors have presumed that both drugs—neither of which is specific for one target—act on membrane proteins (Rothstein *et al.*, 1973; Cabantchik & Rothstein, 1974), and we know of no evidence that either interacts with membrane lipids (Vansteveninck *et al.*, 1965; Rothstein *et al.*, 1973; Cabantchik & Rothstein, 1974). Moreover, if either did interact

with membrane lipids, we expect that the result—if any—would be to decrease the barrier to O_2 diffusion. Thus, the inhibitor data led us to explore channel KOs.

Effects of KOs on drug susceptibility. Although neither pCMBS nor DIDS is specific for a single target, AQP1 and Rh_{Cx} appear to be targets of each. Macey and Farmer (1970) were the first to show that mercurials reduce the water permeability of RBCs (for early review, see Macey, 1984). After the identification of AQP1 as the first H_2O channel, Preston *et al.* (1993) created the C189S mutation and demonstrated that the inhibitory effect of mercury on the H_2O permeability of AQP1 depends specifically on the interaction with Cys-189 (Preston *et al.*, 1993). Moreover, the mutation AQP1-C189S eliminates the ability of pCMBS to reduce P_{M,CO_2} (Cooper & Boron, 1998). Preliminary work suggests that DIDS also reduces the CO_2 permeability AQP1, as expressed in oocytes (Musa-Aziz *et al.*, 2007*b*, 2007*a*, 2025).

In the present study, our mathematical simulations suggest that, on a WT background, pCMBS reduces P_{M,O_2} by ~82% (see paper #3[103]). On the other hand, on a dKO background, the drug decreases P_{M,O_2} only by ~91% – ~55% = ~36% (i.e., inhibition is reduced by 56% on dKO background). For DIDS, the two degrees of inhibition for SC-k_{HbO2} are ~56% on a WT background, and ~76% – ~55% = ~21% on a dKO background (i.e., inhibition is reduced by 63% on dKO background). Thus, the combined absence of AQP1 and Rh_{Cx} reduces the susceptibility of P_{M,O_2} to each drug by a substantial amount. We have already seen that (compared to a WT background) the dKO background reduces the susceptibility of RBCs to nBCD formation (see paper #2[104]). Thus, both from the perspective of P_{M,O_2} reduction and nBCD formation, both AQP1 and Rh_{Cx} appear to be major—although not the exclusive—targets of both pCMBS and DIDS.

---

[103] See Paper #3>table 3, data row #3

[104] See Paper #2>figure 8*b*–*c*

Implications of morphometry and proteomics experiments

Morphometry. We were relieved to see that, for all three KO genotypes, the control cells—as for the WTs—were overwhelmingly shaped as biconcave disks (see paper #2[105]). Therefore, on the basis of RBC morphology alone, we conclude that we have no reason to be suspicious of the genotype-dependent decreases in SC-k_{HbO2} and inferred P_{M,O_2} and the deduction—independent of any inhibitor data—that AQP1 and Rh_{Cx} can be conduits for O_2.

In the absence of inhibitors, nBCD prevalence detected by IFC in WTs and dKOs was <2% (see paper #2[101]); our linear-combination accommodations ought to be most reliable for these control cells (see paper #3[106]). For cells treated with pCMBS, nBCD prevalence is still modest and we believe that our accommodation (i.e., SC-k_{HbO2}) is likely to be nearly as reliable as for control cells. For cells treated with DIDS, which produces smaller k_{HbO2} inhibitory effects than does pCMBS but a much larger nBCD prevalence, we have a lesser degree of confidence in the accuracy of SC-k_{HbO2} and deduced the P_{M,O_2}. Nevertheless, even if we were to ignore the DIDS data, the overall conclusions of our three papers would be unchanged. That is, besides AQP1 and Rh_{Cx} (the support for which comes from KO data on control cells), we conclude that murine RBCs have at least one additional pCMBS-sensitive conduit accounts for ~36% of P_{M,O_2}. If we accept the DIDS SC-k_{HbO2} values at face value, murine RBCs have—in addition to AQP1 and Rh_{Cx}—at least one additional DIDS-sensitive conduit accounts for ~21%. As noted at the outset of the Discussion, the 21% could overlap completely or partially with the 36%.

---

[105] See (a) Paper #2>figures 2–5 and 8 … & … (b) Also see Suppl_Video_1--WT

[106] See Paper #3>Results>Accommodation for non-BCDs

Measurements of major diameter and nBCD prevalence flow from paper #2 paper #3 for mathematical simulations and accommodations. Because of the large number of cells on which we made measurements by IFC (paper #2[107]), we have high confidence in both measurements.

Proteomics. Our proteomics analysis shows that the genetic deletions of AQP1 and RhAG appropriately eliminated those proteins (plus RhD in the case of the RhAG-KO), but had no significant effect on the apparent abundance of any other proteins among those ranked in the top 100 of greatest inferred abundance (see paper #2[108]). Thus, the most straightforward explanation for our genotype-base data on RBCs is that it was the absence of AQP1 or RhCx per se that was responsible for the KO-induced decreases in SC-k_{HbO2} and deduced P_{M,O_2}.

Implications of the macroscopic mathematical model

Basic features of the model

The sphere. We model the RBC as a sphere, the diameter of which is the same as the calculated thickness of the RBCs used in physiological experiments. Thus, our approach emphasizes the free edge of the BCD, which contains most of the HbO_2. Others also have regarded BCD thickness as the dimension most relevant for diffusion (Roughton, 1932; Ponder, 1948; Forster, 1964; Endeward, 2012).

Simulated k_{HbO2} for WT/Ctrl RBCs. Our simulations—based on physical constants and values provided either by the literature or our own measurements on control RBCs from WT mice—produce an SC-k_{HbO2} value of 4.04 s^{-1}, which is within the range of our physiologically observed values obtained in different data sets (i.e., 3.24 s^{-1} in Figure 4*E*, 3.45 s^{-1} in Figure 3*E*,

[107] See Paper #2>tables 3 and 5

[108] See Paper #2>Results>Proteomics

4.09 s^{-1} in Figure 5*D*. We believe that this range of physiologically obtained SC-k_{HbO2} values reflects variations in the potency of the manufacturer-supplied NDT supply, with low potency (i.e., lower effective [NDT]) generating a greater effective unconvected layer around the RBCs (Vandegriff & Olson, 1984*b*), and thus a lower apparent k_{HbO2} value (see paper #3[109]). We presume that our highest-observed SC-k_{HbO2} value reflects our most potent batch of NDT[110] and thus our most reliable estimate of a reference SC-k_{HbO2} for WT/Ctrl RBCs of our C57BL/6_{Case} mouse strain. This value of 4.09 s^{-1} also is closest to our simulated value of 4.04 s^{-1}.

In our studies with pCMBS (e.g., see Figure 3) and with DIDS (e.g., see Figure 4), we always examined RBCs, ±inhibitor, from the same mouse on the same day, thereby minimizing effects of NDT potency.

Predictions for effects on P_{M,O_2}. Starting with the simulation in which we assumed a provisional P_{M,O_2} of 0.15 cm s^{-1}—this yielded the provisional MMM-k_{HbO2} value of 3.99 s^{-1} noted above (see also paper #3[111])—we systematically varied P_{M,O_2} in a series of nearly 75 simulations. The result is a sigmoidal dependence of k_{HbO2} on log(P_{M,O_2}), as shown in paper #3[112]. The highest simulated P_{M,O_2} is ~22.6 cm s^{-1}, which is near the asymptote of SC-k_{HbO2} ≅ 6 s^{-1}, corresponds to a situation in which we replace the membrane with an equivalent thickness of water. Thus, simulating a physiological SC-k_{HbO2} of 3.99 s^{-1} requires that we reduce the P_{M,O_2} of a "water

---

[109] See Paper #3>figure 11

[110] For our current SF experiments, we purchase several sealed glass bottles of NDT, and open them one at a time until we find one that has a powdery NDT-gas interface. The other bottles, which have a film or crust at the surface (due to NDT that has reacted with O_2 and H_2O), we discard. We store both new and open bottles in an evacuated desiccator.

[111] See Paper #3>table 4

[112] See Paper #3>figure 6

membrane" by a factor of (22.6/0.15) ≅ 150. These data are inconsistent with the implicit assumption of Krogh that membranes, including RBC membranes, offer no resistance to O_2 diffusion. In fact, RBC membrane, even with a full complement of O_2 channels, offer substantial resistance to O_2 diffusion, and this resistance increases even further with the genetic deletion of channels and/or treatment with inhibitors (paper #3[113]).

Ability of inhibition of P_{M,O_2} to decrease k_{HbO2}. Figure 11 is a transformation of the data in the aforementioned sigmoidal curve in paper #3[112]. Here in Figure 11 we show how the computed "% decrease of SC-k_{HbO2}" depends on the imposed "% decrease in P_{M,O_2}". At the lower left, the WT/Ctrl point confirms that 0% decrease in permeability (P_{M,O_2} = 0.1546 cm s^{-1}) yields 0% decrease of SC-k_{HbO2} (k_{HbO2} = 4.04 s^{-1}). The point at the upper right confirms that a 100% decrease in permeability (P_{M,O_2} = 0) fully blocks O_2 offloading (k_{HbO2} = 0). Between these two extremes are points that represent key results of the present paper. For example, simulating the ~30% decrease in SC-k_{HbO2} that we observe with dKO/Ctrl RBCs requires that we reduce the P_{M,O_2} from its reference value of 0.1546 cm s^{-1} by 55%. Replicating the ~78% decrease in SC-k_{HbO2} that we observed for dKO/pCMBS requires that we reduce P_{M,O_2} by 91%. If O_2 permeability depended only on O_2 solubility in the lipid phase of the membrane, as required by Overton's rule, then the seven experimental maneuvers (from AQP1-KO/Ctrl near the lower left to dKO/pCMBS near the upper right) would have been without effect on either P_{M,O_2} or k_{HbO2}, and all the points in Figure 11 would overlie one another at the origin. This is clearly not the case. Thus, Overton's rule, at least as applied to the O_2 permeability of our murine RBCs under our experimental conditions, must be false.

---

[113] See Paper #3>Discussion>Calculation of the contribution of the plasma membrane to total diffusive resistance to O_2>Potential contribution of channels to R_M and R_{Total}.

Additivity of P_{AQP1,O_2} and P_{RhCx,O_2}. One way of evaluating the internal consistency of our macroscopic mathematical model and resulting simulations is to ask whether the decreases in P_{M,O_2} predicted in Figure 11 for the individual channel knockouts sum to the same value as for the double knockout

$$\begin{array}{ccccc} (\Delta P_{M,O_2})_{\mathbf{AQP1\text{-}KO}} & + & (\Delta P_{M,O_2})_{\mathbf{RhAG\text{-}KO}} & \overset{?}{=} & (\Delta P_{M,O_2})_{\mathbf{dKO}} \\ \underbrace{(-22\%) \quad + \quad (-36\%)}_{58\%} & & & \cong & (-55\%) \end{array} . \tag{2}$$

The agreement is good, with the individual KOs summing to a predicted P_{M,O_2} decrease of ~58%, slightly above the observed dKOs value of ~55%. We conclude that the model, as tested by physiological data, is well behaved.

Sensitivity analysis

Paper #3[114] presents an analysis of the sensitivity of the simulated k_{HbO2} to changes in eight key kinetic and geometric parameters. Our general conclusion is that no reasonable change in any parameter could account for our k_{HbO2} data on control RBCs from KO mice, let alone from inhibitor-treated RBCs from dKO mice. More specifically, k_{HbO2} is: (1) only modestly sensitive to $k_{HbO2 \rightarrow Hb+O2}$, which we measure; (2) only mildly sensitive to changes in $[Hb_{Total}]_i$, which also is a measured parameter; (3) modestly sensitive to changes in O_2 diffusion constants and virtually insensitive to changes in HbO_2 and Hb diffusion constants; and (4) moderately sensitive to changes in either the thickness of the unconvected layer or (5) the diameter of the sphere that, in the MMM, emulates $Ø_{Major}$. Because the simulations deal with a single cell with no extracellular hemoglobin, the results are, by definition, both hemolysis- and shape-corrected.

[114] See Paper #3>Results>Mathematical simulations exploring the predicted sensitivity of k_{HbO2} to eight key kinetic and geometric parameter

Effect of channel knockouts on MCV and MCHC

In our broadest automated-hematology data set (see Table 4), the knockouts involving RhAG (RhAG-KO and dKO) were associated with a statistically significant increases in MCV and reciprocal decreases in MCHC; the AQP1-KO data trended in the same direction. In a narrower data subset restricted to mice used in IFC studies—and then in mathematical simulations—these patterns of MCV and MCHC persisted as trends but did not reach statistical significance (see paper #2[115]).

MCV. Our imaging–flow-cytometry studies indicate that the aforementioned increases in MCV are mainly attributable to an increased prevalence of immature cell types (see paper #2[116]), consistent with increased RBC production. Because both AQP1 and Rh_{Cx} are important components of the ankyrin complex (Vallese *et al.*, 2022), one might think that the deletion of one or both channels might impact RBC deformability, which in turn could lead to a decrease in average RBC lifespan, consistent with our observation of increased immature cell types. One might also think that the deletions could increase RBC fragility. However, we did not observe genotype-related differences in hemolysis within the SF reaction cell (see Figure 6*F*).

MCHC. Whereas the genetic deletion of one or both channels tends to raise MCV, the effect on MCH is virtually nil (see Table 4). As a result, MCHC—that is, the ratio MCH/MCV—tends to fall as MCV rises. The parameter-sensitivity analysis in paper #3[114] indicates that, all else (including $[Hb_{Total}]_i$) being equal, increases in the sphere diameter (a surrogate for RBC thickness, which is related to MCV) used in the mathematical model causes MMM-k_{HbO2} to fall rather

---

[115] See paper #2>table 4, which is a subset of the larger data set in Table 4 (in paper #1) and is restricted to the mice used in the experiments on imaging flow cytometry and the mathematical simulations. Although the numbers of observations are smaller, the trends are similar.

[116] See paper #2>table 2

steeply[117]. On the other hand, the sensitivity analysis also shows that decreases in $[Hb_{Total}]_i$, all else (including sphere diameter) being equal, causes MMM-k_{HbO_2} to rise rather steeply[118]. Intuitively, one might think that the two effects—↑MCV and ↓MCHC—would tend to cancel, a hypothesis that we address in the next paragraph.

Simulations based on genotype-specific data. To address the above hypothesis, in paper #3 of this series, we perform a set of mathematical simulations in which we mimic control cells (i.e., not pretreated with inhibitors) of all four genotypes. The input parameters are genotype-specific values of MCV, MCHC, $Ø_{Major}$. This analysis[119] predicts that the AQP1-KO would actually increase SC-k_{HbO_2} by ~1% to 3% (vs. the observed 9% decrease in Figure 5*B*). The simulated SC-k_{HbO_2} for the RhAG-KO is down by ~4% from WT vs. the observed ~17% decrease, and that for the dKO is down by ~4% to ~6% from WT vs. the observed ~30% decrease. We conclude that the effects of anti-parallel (1) increases in MCV and (2) decreases in MCHC do indeed tend to cancel, and that variations in RBC dimensions and $[Hb_{Total}]_i$ cannot account for our SC-k_{HbO_2} data among the four genotypes in the present study.

Reports on O_2 channels

Yeast expression system. In experiments on protoplasts from the yeast *Saccharomyces cerevisiae*, (Zwiazek *et al.*, 2017) used the absorbance spectrum of myoglobin (Mb) to assess O_2 influx. They found that expression of NtPIP1;3 from *Nicotiana tabacum*—but not that of several other plant AQPs, including AtPIP1;2 from *Arabidopsis thaliana*—substantially and significantly increased the rate of O_2 uptake (as reported by the Mb absorbance spectrum) vs.

---

[117] See paper #3>figure 12

[118] See paper #3>figure 9

[119] See paper #3> figure 5

mock transfection. Interestingly, the AtPIP1;2 rate trended below "mock", perhaps an example of a "blocking protein"—a non-conducting membrane protein that reduces available surface area of the lipid bilayer—or the result of reduced expression of other O_2 channels. The rate of human AQP1 was modestly but significantly greater than that of AtPIP1;2.

The authors did not translate changes in absorbance spectrum to changes in myoglobin O_2 saturation or O_2 fluxes, as in Figure 3*D*. Nor did they consider other components of the system that would have impacted rates of O_2 influx (the opposite direction of those shown in Figure 2): (1) depletion of O_2 in the EUF, especially in the absence of an extracellular O_2 donor; (2) diffusion of O_2, Mb, and MbO_2 through the intracellular fluid; or (3) the association-reaction rate constant $k_{Mb+O_2 \rightarrow MbO_2}$, analogous to our dissociation-reaction rate constant $k_{HbO_2 \rightarrow Hb+O_2}$, as measured in Figure 10.

Murine RBCs. In a preprint, Zhao *et al.* (2020) reported the essential elements and conclusions of the present paper, though without the accommodation for nBCDs that we implement in the present series of papers.

Human and murine RBCs. In a recent paper, Al-Samir *et al.* (2025) applied insights from the Zhao preprint to work on RBCs, ±DIDS, from both WT and AQP1-KO mice as well as normal and Colton-null (*Aqp1*–/–) humans. They also extended the temperature from 7 or 10 °C to 25 °C, and 37 °C. We note several differences between their study and ours:

Mouse strains. Al-Samir *et al.* used "C57BL/6" mice. Kelmenson (2016) has noted that BL/6 strains can differ substantially. We used "C57BL/6_{Case}", which we characterize (see Table 1).

Study design. Our murine study is more expansive in that we include the second inhibitor pCMBS, as well as the strains RhAG-KO and dKO. Whereas Al-Samir *et al.* used WT mice at ages from ~ 3 to ~18 months, and AQP1-KO mice at ages ~4 to ~16 months, in the present study,

we used mice (all genotypes) between ~2 and ~4 months of age. Although not a part of the present study, preliminary work shows that k_{HbO_2} values of WT/Ctrl RBCs are indistinguishable from ages 2 to 3 months through 12 months of age, but begins to fall at ~12 months, decreasing by ~13% at age 29 months (i.e., the lifespan of our C57BL/6_{Case} mice; Zhao & Boron, 2019, Zhao *et al.*, 2021). Thus, some of the data of Al-Samir *et al.* could have been confounded by aging.

Automated hematology. Al-Samir *et al.* reports MCV on four mice of each genotype/sex. We report a full hematological analysis on each mouse and used the results—along with $Ø_{Major}$ measured by imaging flow cytometry—to compute RBC thickness and $[Hb_{Total}]_i$, both of which we use in our simulations and estimation of P_{M,O_2}.

Hemolysis accommodation. Al-Samir *et al.* collected effluent from the reaction cell after multiple SF shots, centrifuged, estimated free [Hb], and applied a correction. This approach likely overestimated actual hemolysis because, after the k_{HbO_2} assay in the reaction cell, additional RBC lysis is likely to have occurred. Indeed, their reported % hemolysis levels were 3-fold greater than ours. Assuming that their actual % hemolysis values were similar to ours, their overestimates of *Act%H* would have led to an overcorrection and thus lower HC-k_{HbO_2} values. If we had applied such underestimated HC-k_{HbO_2} values to compute % inhibitions due to DIDS or AQP1-KO (see Figure 8 and Table 3), we would have generated large overestimates of % inhibition.

We use a CA-based assay (Zhao *et al.*, 2017) that reports *Act%H* within the SF reaction cell, based on single "shots". Although this approach is time consuming, it assesses hemolysis under the conditions of the k_{HbO_2} determinations. Moreover, our operationally defined correction (see Figure 8) is based on a series of k_{HbO_2}-like measurements over a range of imposed degrees of hemolysis and thus is free of theoretical assumptions.

Poikilocytes. Al-Samir *et al.* noted "highly irregular shaped" RBCs in their confocal observations of "almost all" DIDS-treated murine cells but neither quantitated nBCD prevalence nor accommodated for it.

In the present papers, we report the statistics of studies in which we used IFC to measure nBCD prevalence among hundreds of thousands of cells among various protocols (see paper #2[120]). Moreover, we used these prevalences to correct HC-k_{HbO_2} values (see paper #3[121]). If we had ignored the shape correction in the case of WT/DIDS, the result would have been a large underestimate of the true k_{HbO_2}, and thus a large-overestimate DIDS-induced inhibition (see Table 3*A*).

Proteomics. The study of Al-Samir *et al.* did not include a proteomic analysis. On a different strain of mice, we saw no major differences in AQP1-KOs except for the loss of AQP1 (see paper #2[122]). In the case of Colton-null human RBCs, no data are available to address the issue of whether the cells compensated for the absence of AQP1.

Murine data at low temperature. We chose to work at 10 °C to achieve: (1) maximal signal fidelity, like others[123] before us, and (2) minimal hemolysis (Gershfeld & Murayama, 1988).

We observed several differences vis-à-vis the murine data of Al-Samir *et al.* and ours.

(1) Their absolute $t_{½}$ at 7 °C appears to be ~2.5-fold faster[124] than in the present study at 10 °C (e.g., see Figure 3), even though we worked at a somewhat higher temperature. Although a difference in mouse strain could have contributed to this difference, this effect—based on our preliminary work (Zhao & Boron, 2023)—might have increased k_{HbO_2} by ~35%. As noted above,

---

[120] See Paper #2>table 5

[121] See Paper #3>Results>Accommodation for non-BCDs

[122] See Paper #2>table 7

[123] See Discussion>Reports on O_2 channels>Q_{10} estimates

[124] See Al-Samir *et al.*, figure 5

their reported hemolysis was ~3× ours. If this degree of hemolysis was accurate but unaccommodated, it would have led to an overestimate of k_{HbO_2}. However, based on our hemolysis accommodations (e.g., see Figure 7), the effect would have been an overestimation of only ~40%.

(2) DIDS seems to have a much larger effect in their study[125], increasing $t_{½}$ by ~3-fold (i.e., $1/(t_{½})$ falls by two-thirds). DIDS caused our k_{HbO_2} to fall by only about half as much, ~31% (see paper #3[126]). The omission of a shape correction would have led to an overestimated % inhibition by DIDS (see Table 3*A*).

(3) The data of Al-Samir *et al.* demonstrate a statistically significant effect of the AQP1-KO on $t_{½}$—an increase of ~26%, corresponding to a decrease of ~21% in $1/(t_{½})$[124]. We observed a decrease of only ~9% in SC-k_{HbO_2} (see Table 3*B*).

(4) The computed P_{M,O_2} of Al-Samir *et al.* is about the same as our value of ~0.155 cm s^{-1}. This is curious, inasmuch as their absolute rate constants were ~2.5× higher at a lower temperature. They also found that DIDS reduced P_{M,O_2} to nearly zero vs. the ~56% reduction in our studies (paper #3[126]). Thus the calculations—which for us incorporate MCV, MCHC, $Ø_{Major}$, and $k_{HbO_2 \rightarrow Hb+O_2}$ as well as sequential corrections for hemolysis (in the reaction cell) and shape corrections—must have been fundamentally different.

Human data at 10 ℃. Al-Samir *et al.* report substantially slower $t_{½}$ values for human than for mouse RBCs[124], consistent with a greater MCV. Compared to normal RBCs, Colton-nulls exhibit a statistically significant difference in $t_{½}$—an increase of ~13%, corresponding to a

[125] See Al-Samir *et al.*, figure 7

[126] Paper #3>table 3

decrease of ~12% in $1/(t_{½})$. DIDS produces a significant difference in $t_{½}$—an increase of ~22%, corresponding to a decrease of ~18% in $1/(t_{½})$.

Human and murine data at temperatures out to 37 °C. For the human data of Al-Samir *et al.*, the trend, as temperature increases from 10 °C to 37 °C is for the $t_{½}$ differences among (1) normal, (2) normal/DIDS, (3) Colton-null, and (4) Colton-null/DIDS—already small at 10 °C—to decrease even further[125]. The four mean $t_{½}$ values are indistinguishable at 25 °C. At 37 °C, the authors report a significant difference (i.e., a small increase in $t_{½}$) between normal/Ctrl and normal/DIDS, but no effect of the Colton-null mutation. A contributing factor, despite all the dots in the bar graphs, may be an N of 2 for the Colton-null blood donors.

The murine data, yield "faster" $t_{½}$ values at higher temperature, consistent with the smaller MCV of murine RBCs. As with human RBCs, the absolute differences in $t_{½}$ values tend to collapse with increasing temperature. Even so, at 25 °C, the authors reported a statistically significant difference in $t_{½}$ values (a small increase) between WT/Ctrl and WT/DIDS. At 37 °C, DIDS had no effect with WTs, but did produce a statistically significant effect in AQP1-KOs—a decrease in $t_{½}$ (i.e., "faster"). This last effect is paradoxical—DIDS, if anything, should have caused $t_{½}$ to rise.

The ability of Al-Samir *et al.* to measure $t_{½}$ values as short as ~0.018 s for murine WT/Ctrl, WT/DIDS, and AQP1-KO/Ctrl cells is impressive. On the other hand, one must ask, especially in light of the aforementioned paradoxical DIDS effect, if the hardware/software are capable of reporting with fidelity events with a $t_{½}$ values as brief as 0.018 s—and, more importantly, events that are substantially faster.

Q_{10} estimates. Physiological processes generally have Q_{10} values from 2 to 4. From the data of Al-Samir *et al.*[124], we calculate that $1/(t_{½})$ increased ~6.2-fold from 7 °C to 37 °C; this corresponds to a Q_{10} of ~1.8. In a study of glucose transport in human RBCs, Lowe and Walmsley (1986) found that the velocity of ^{14}C-glucose uptake increased ~10 fold between 10 °C and

37 °C[127] in their slower equilibrium-exchange conditions; this corresponds to a Q_{10} of ~2.4. In their faster zero-trans experiments, the influx increased >300-fold, with a Q_{10} of nearly 8.3. Based on values of K^+ influx on guinea-pig RBCs reported by Kimzey and Willis (1971), we calculate a Q_{10} of 3.0 for the "total" K^+ influx, and 5.5 for the "active" (i.e., ouabain-sensitive) component. Based on values for the rate constant of Cl-HCO_3 exchange in human RBCs by Chow *et al.* (1976), we calculate report a Q_{10} of 3.2. Studying the apparent Cl^- permeability mediated by AE1, Jensen *et al.* (2001) report a Q_{10} for human RBCs, based the data of Brahm (1977), of 7.2 below 15 °C but 3.44 above 15 °C.

O_2 offloading from RBCs includes at least one enzyme-like step (i.e., dissociation of HbO_2) and permeation of O_2 through at least three membrane proteins, which one can consider as transport enzymes. Thus, in the study of Al-Samir *et al.*, we would have anticipated a Q_{10} in the range of the other processes noted above. Given the exponential nature of Q_{10}, the Al-Samir velocity at 37 °C—already extremely fast by RBC SF standards—would have had to have been 2.2-fold greater to reach the lower of the two Q_{10} values (i.e., 2.4) of Lowe and Walmsley (1986), 4.6-fold greater to reach the lower of the two Q_{10} values (i.e., 3.0) of Kimzey and Willis (1971), 5.6-fold greater to reach the Q_{10} (i.e., 3.2) of Chow *et al.* (1976), 6.7-fold greater to reach the lower of the two values (i.e., 3.4) from Jensen *et al.* (2001)—and greater yet for the other cited RBC values. If the true Q_{10} for O_2 offloading from murine RBCs is even the lowest cited value of 2.4, the murine k_{HbO2} signal observed by Al-Samir *et al.* at 37 °C would have been clipped at a level far below the actual k_{HbO_2}, and they would not have been able to detect the effect of DIDS inhibition, and especially not the expected smaller effect of the AQP1-KO.

[127] Interpolated from their figure 2

We propose that the proper control experiment for ruling out clipping of the murine k_{HbO_2} signal at 37 °C is to demonstrate that one can detect a substantially faster O_2-offloading process. Absent that control, the present data do not support the conclusion of Al-Samir *et al.* (2025) that AQP1 and other DIDS-sensitive pathways, although they contribute to O_2 permeability at 10 °C, lose that property at 37 °C.

Aside from the technical issues raised above, we ask why, during evolution, organisms would have paid the high metabolic price of retaining AQP1 and Rh_{Cx} only so they could promote O_2 and CO_2 fluxes at 10 °C but not at physiological temperatures? Paper #2[128] shows that the combination of AQP1, RhAG, and RhD—which accounts for 55% of P_{M,O_2}—constitutes >13% of the murine RBC-ghost PMA proteome. We do not know the identity of the pathway responsible for the missing 36% of P_{M,O_2} in the dKO ±pCMBS. However, if the missing protein(s) has a unitary conductance and MW similar to those of AQP1 and Rh_{Cx}, we conclude that it would account for an additional >8% of the PMA proteome, for a total of ~22%. Considering that—in the human body—RBCs constitute 70% of total cell number and ~85% of the new cells created every day, this ~22% of the PMA proteome represents an enormous whole-body metabolic liability. Of course, AQP1 is a powerful H_2O channel (Preston & Agre, 1991; Preston *et al.*, 1992). However, the physiological role of RBCs is not to transport H_2O. Both AQP1 and Rh_{Cx} also conduct NH_3 (Nakhoul *et al.*, 2001; Nakhoul & Hamm, 2004). However, we suggest that an easier solution for NH_3 carriage would have been for RBCs to increase their expression of UT-B, which also conducts NH_3 (Geyer *et al.*, 2013*a*). Instead, human RBCs have evolved a multicomponent ankyrin-1 complex (Vallese *et al.*, 2022) that forms a metabolon that brings AE1, Rh_{Cx}, and AQP1 into extremely close proximity, presumably, we suggest, to promote CO_2 and O_2 carriage by RBCs—the main physiological role of these cells. And when the mouse attempts to evade the cat, it is to

[128] See Paper #2>Results>Proteomics

the benefit of the mouse that its RBC gas channels—for which it has paid such a dear metabolic price—make a meaningful contribution at 37 °C.

Acknowledgements

We thank Jean-Pierre Cartron for the gift of RhAG-KO mice. We thank him and Gerolf Gros and for extremely helpful discussions at the outset of the project. We thank Seong-Ki Lee for developing an improved approach for genotyping the RhAG-KO mice. The authors gratefully acknowledge Daniela Calvetti and Erkki Somersalo for having developed the engine of an earlier version of the CO_2/pH reaction-diffusion model of an oocyte, which in part served as the starting point for the RBC model. We thank Thomas Radford for organizing the husbandry of the mouse colonies; Gerald Babcock for his role as laboratory manager; James W. Jacobberger and Philip G. Woost of the CWRU Flow Cytometry and Imaging Microscopy Core (FCIMC) for their assistance with flow cytometry; and Daniela Schlatzer of the CWRU Center for Proteomics and Bioinformatics for their assistance with mass spectrometry. This work was supported by Office of Naval Research (ONR) grant N00014-11-1-0889, N00014-14-1-0716, and N00014-15-1-2060; a Multidisciplinary University Research Initiative (MURI) grant N00014-16-1-2535 from the DoD, NIH grant multi-scale modeling grant 5U01GM111251 (to WFB), and NIH grant R01HL160857 (to WFB). R.O. and the modeling were supported in part by NIH grant K01-DK107787. R.R.G was supported by a fellowship grant from the ONR (N00014-12-1-0326). W.F.B. gratefully acknowledges the support of the Myers/Scarpa endowed chair.

Tables

Table 1. Genetic background analysis of C57BL/6$_{Case}$ mice, based on ~10,000 single-nucleotide polymorphisms*

Character / Genotype	C57BL/6J	C57BL/6N	C57BL/6Group	Total
Aqp1+/+Rhag+/+	17.60 ± 0.89 %	18.85 ± 1.35 %	23.80 ± 0.00 %	60.25 %
Aqp1–/–	16.57 ± 1.49 %	19.40 ± 0.00 %	28.60 ± 0.00 %	64.57 %
Rhag–/–	22.77 ± 1.43 %	19.40 ± 0.00 %	28.60 ± 0.00 %	70.77 %
Aqp1–/–Rhag–/–	21.38 ± 3.20 %	24.73 ± 2.61 %	21.42 ± 5.85 %	67.53 %
Average	19.58 %	20.60 %	25.60 %	65.78 %

*N is 6 for each genotype, values represent mean ± SD.

Table 2. Physiological solutions*

Solution / Component or parameter	Oxygenated solution (also, RBC washing)	De-oxygenated solution	Components for OOE Hemolysis assay			Solutions for preparation of mouse erythrocyte ghosts		
			$\mathcal{A}$	$\mathcal{B}$	Mix†	Sedimentation Buffer	Wash Buffer	Lysis Buffer ‡
NaCl (mM)	92.5	15	140	116	128	150	150	0
KCl (mM)	0§	0§	3	3	3	0	0	0
$CaCl_2$ (mM)	0.01	0.01	2	0	1	0	0	0
Na_2HPO_4 / NaH_2PO_4 (mM)‖	44.89/13.11	44.89/13.11	0	0	0	4.06/0.94	0	0
HEPES (mM)	0	0	16	0	8	0	0	0
$NaHCO_3$ (mM)¶	0	0	~0	44	22	0	0	0
CO_2 (%)	0	0	~0	~1	0.5	0	0	0
pH	~7.40‖	~7.40‖	7.03#	8.41¶	~7.25	~7. 5‖	~7.0	~8.0
Pyranine (μM)Δ	0	0	0	2◊	1◊	0	0	0
RBCs or lysate	++	0	++▽	0	+▽	+	+	+
NDT♦	0	50	0	0		0	0	0
Tris-HCl (mM)	0	0	0	0	0	0	0	5
Dextran500(w/v)	0	0	0	0	0	0.75%	0	0
Temperature (°C)	RT	RT	10	10	10	RT	RT	RT
Osmolality (mOsm)	~300	~300	~295	~300	~298	_	~290	_

*This table shows the compositions of all the solutions used in either the present paper (1st in the series of 3) or the following paper (2nd of 3). The only solution in common with the two papers is the "Oxygenated solution". The "Deoxygenated solution" and the three "OOE" solutions ("$\mathcal{A}$", "$\mathcal{B}$", and "Mix") were used only in the present paper. The three "Solutions for the preparation of mouse erythrocyte ghosts" were used only in the following paper.

[†]The values in this "Mix" column are those at the instant of mixing solutions $\mathcal{A}$ and $\mathcal{B}$ (Zhao *et al.*, 2017). The solution is out of equilibrium because the pH of 7.25 is far too low for the system to be in equilibrium, given [HCO_3^-] = 22 mM and CO_2 = 0.5%. Note that both solutions "$\mathcal{A}$" and "$\mathcal{B}$" were equilibrated with room air and are thus oxygenated.

[‡]Complete protease inhibitor tablet (Roche) – only for lysis and first wash following lysis step.

[§](Coin & Olson, 1979) previously used 0 mM KCl in this solution.

[‖]The ratio [$HPO_4^=$]/[$H_2PO_4^-$] determines the pH at RT (~22°C).

[¶]The addition of HCO_3^- generates a trivial amount of CO_2 and also some $CO_3^=$, and spontaneously yields a pH of 8.41 at 10°C.

[#]We titrated HEPES free acid (pK ~7.41) to pH 7.03 with NaOH at 10°C.

[Δ][Pyranine] in the reaction cell was either 1 μM (to obtain pH data) or 0 μM (to obtain background data).

[◊]In the hemolysis assay, when determining the background for the fluorescence signal, we omitted the pyranine dye.

[▽]In the hemolysis assay, when determining the uncatalyzed rate constant (k_{uncat}) of the reaction $HCO_3^- + H^+ \rightarrow CO_2 + H_2O$, we omitted RBCs and lysate.

[♦]NDT is freshly added and used within ~1 h. Final [NDT] in SF reaction cell is 25 mM.

Table 3. Summary of raw, hemolysis-corrected, and shape-corrected k_{HbO_2} values

A. k_{HbO_2} of RBCs from WT mice, ±inhibitors

Condition / Parameter	Ctrl	pCMBS	*P*-value	Ctrl	DIDS	*P*-value
Raw-k_{HbO_2} (s^{-1})	3.74 ± 0.31	1.81 ± 0.39	5.89×10^{-8}	3.56 ± 0.30	2.38 ± 0.12	1.08×10^{-6}
HC-k_{HbO_2} (s^{-1})	3.42 ± 0.25	1.26 ± 0.19	4.97×10^{-7}	3.21 ± 0.27	1.65 ± 0.19	3.84×10^{-8}
SC-k_{HbO_2} (s^{-1})	3.45 ± 0.25	1.34 ± 0.20	7.03×10^{-7}	3.24 ± 0.27	2.23 ± 0.26	1.07×10^{-6}
N	8			8		

Values represent mean ± SD. HC- k_{HbO_2}, hemolysis-corrected k_{HbO_2}; SC- k_{HbO_2}, shape-corrected k_{HbO_2}. For each comparison we use paired two-tailed t-test.

B. k_{HbO_2} of RBCs from WT and knockout mice

Condition / Parameter	WT	*Aqp1–/–*	*Rhag–/–*	*Aqp1–/–Rhag–/–*
Raw-k_{HbO_2} (s^{-1})	4.22 ± 0.51	3.81 ± 0.32	3.56 ± 0.21	2.99 ± 0.23
HC-k_{HbO_2} (s^{-1})	4.05 ± 0.48	3.68 ± 0.29	3.37 ± 0.15	2.80 ± 0.23
SC-k_{HbO_2} (s^{-1})	4.09 ± 0.49	3.73 ± 0.30	3.41 ± 0.15	2.84 ± 0.24
N	10	12	10	11

Values represent mean ± SD. For statistical analysis, we use one-way ANOVA with Holm-Bonferroni post-hoc means comparison for the mean Raw-k_{HbO2} values, the mean hemolysis-corrected k_{HbO2} (HC-k_{HbO2}) values and the mean shape-corrected k_{HbO2} (SC-k_{HbO2}) values of all four mouse strains (shown in Statistics Table 1).

C. k_{HbO_2} of RBCs from double-knockout mice, ±inhibitors

Condition / Parameter	Ctrl	pCMBS	*P* value	Ctrl	DIDS	*P*-value
Raw-k_{HbO_2} (s^{-1})	2.90 ± 0.13	1.37 ± 0.06	3.47×10^{-10}	2.75 ± 0.30	2.20 ± 0.12	3.24×10^{-4}
HC-k_{HbO_2} (s^{-1})	2.59 ± 0.18	0.81 ± 0.23	3.99×10^{-9}	2.48 ± 0.33	1.47 ± 0.23	3.44×10^{-5}
SC-k_{HbO_2} (s^{-1})	2.63 ± 0.18	0.84 ± 0.24	4.96×10^{-9}	2.52 ± 0.34	1.70 ± 0.27	2.30×10^{-4}
N	8			9		

Values represent mean ± SD. For each comparison we use paired two-tailed t-test.

Table 4. Summary of all hematological data obtained from four strains of mice†

Mouse / Parameter	WT			AQP1-KO			RhAG-KO			dKO		
Sex	**M**	**F**	**M+F**	**M**	**F**	**M+F**	**M**	**F**	**M+F**	**M**	**F**	**M+F**
N	9	15	24	14	8	22	17	12	29	10	7	17
Age weeks	12.2 ± 2.5	13.8 ± 3.0	13.2 ± 2.9	12.1 ± 2.5	14.0 ± 2.9	12.8 ± 2.7	14.1 ± 3.0	14.4 ± 4.0	14.2 ± 3.4	12.6 ± 2.9	15.0 ± 0.6	13.6 ± 2.5
WBC $10^3/\mu l$	12.1 ± 4.7	10.2 ± 2.6	10.9 ± 3.6	12.9 ± 3.8	14.5 ± 4.1	13.5 ± 3.9	13.6 ± 4.2	10.7 ± 4.4	12.4 ± 4.4	12.0 ± 3.6	10.7 ± 2.5	11.5 ± 3.2
LYM $10^3/\mu l$	9.8 ± 3.8	8.5 ± 2.2	9.0 ± 2.9	11.0 ± 3.4	12.3 ± 3.0	11.5 ± 3.2	11.4 ± 3.6	9.0 ± 3.8	10.4 ± 3.8	10.1 ± 3.3	9.1 ± 2.4	9.7 ± 2.9
MONO $10^3/\mu l$	0.6 ± 0.2	0.4 ± 0.2	0.5 ± 0.2	0.5 ± 0.2	0.6 ± 0.2	0.5 ± 0.2	0.5 ± 0.2	0.5 ± 0.2	0.5 ± 0.2	0.5 ± 0.1	0.5 ± 0.1	0.5 ± 0.1
GRAN $10^3/\mu l$	1.7 ± 1.0	1.2 ± 0.4	1.4 ± 0.7	1.4 ± 0.6	1.6 ± 1.1	1.5 ± 0.8	1.7 ± 1.0	1.2 ± 0.6	1.5 ± 0.9	1.4 ± 0.4	1.2 ± 0.2	1.3 ± 0.4
LYM %	81.9 ± 5.3	83.8 ± 4.2	83.1 ± 4.7	84.8 ± 5.7	85.7 ± 4.2	85.1 ± 5.1	83.4 ± 7.1	83.5 ± 4.2	83.4 ± 6.0	83.8 ± 3.3	84.1 ± 3.5	83.9 ± 3.3
MONO %	4.4 ± 1.2	3.9 ± 0.6	4.1 ± 0.9	3.7 ± 1.0	3.4 ± 0.8	3.6 ± 0.9	3.8 ± 0.8	4.0 ± 0.8	3.9 ± 0.8	3.6 ± 0.8	4.2 ± 1.1	3.8 ± 0.9
GRAN %	13.7 ± 4.7	12.3 ± 3.7	12.8 ± 4.1	11.6 ± 4.8	10.9 ± 3.5	11.3 ± 4.3	12.8 ± 6.7	12.6 ± 3.5	12.7 ± 5.5	12.6 ± 2.8	11.7 ± 2.6	12.2 ± 2.7
Hct %	49.0 ± 6.1	49.0 ± 7.5	49.0 ± 6.9	48.8 ± 6.9	51.6 ± 4.3	49.8 ± 6.1	50.2 ± 7.8	50.6 ± 9.9	50.3 ± 8.6	54.4 ± 6.9	49.6 ± 4.2	52.4 ± 6.3
HGB g/dl	15.5 ± 1.2	15.5 ± 2.3	15.5 ± 1.9	15.2 ± 1.7	16.1 ± 0.5	15.5 ± 1.5	14.6 ± 2.0	14.7 ± 2.4	14.6 ± 2.1	16.0 ± 1.3	14.8 ± 0.9	15.5 ± 1.3
RDWa fl	33.0 ± 3.7	31.8 ± 2.3	32.3 ± 2.9	32.7 ± 2.3	32.4 ± 2.6	32.6 ± 2.3	35.1 ± 2.1	34.6 ± 1.9	34.9 ± 2.0*	35.3 ± 2.8	34.0 ± 1.5	34.7 ± 2.4*
RDW %	18.4 ± 1.6	17.5 ± 1.0	17.9 ± 1.3	17.6 ± 0.5	17.4 ± 0.6	17.6 ± 0.6	17.5 ± 0.6	17.2 ± 0.4	17.4 ± 0.5	18.2 ± 0.8	17.5 ± 0.6	17.9 ± 0.8
MCH pg	14.8 ± 0.9	14.7 ± 0.4	14.7 ± 0.6	14.8 ± 0.8	14.9 ± 0.4	14.8 ± 0.7	14.7 ± 0.5	14.8 ± 0.5	14.7 ± 0.5	14.5 ± 0.4	14.8 ± 0.4	14.6 ± 0.4
MCV fl	46.6 ± 2.8	46.6 ± 3.6	46.6 ± 3.2	47.3 ± 2.6	47.5 ± 3.6	47.3 ± 2.9	50.3 ± 1.5	50.5 ± 1.4	50.4 ± 1.5*	49.1 ± 3.4	49.4 ± 1.1	49.2 ± 2.7*
MCHC g/dl	31.7 ± 2.0	31.6 ± 1.9	31.7 ± 1.9	31.4 ± 3.1	31.5 ± 2.2	31.4 ± 2.7	29.2 ± 1.1	29.3 ± 1.3	29.2 ± 1.1*	29.6 ± 2.2	30.0 ± 0.9	29.8 ± 1.8*
RBC $10^6/\mu l$	10.5 ± 1.0	10.6 ± 1.6	10.5 ± 1.4	10.3 ± 1.3	10.8 ± 0.5	10.5 ± 1.1	10.0 ± 1.5	10.0 ± 1.8	10.0 ± 1.6	11.1 ± 1.0	10.0 ± 0.7	10.6 ± 1.0
PLT $10^3/\mu l$	294.1 ± 152.1	320.9 ± 180.8	310.8 ± 167.7	303.6 ± 146.6	325.9 ± 117.7	311.7 ± 134.3	377.6 ± 179.6	261.4 ± 141.1	329.6 ± 172.2	353.2 ± 158.9	255.9 ± 118.7	313.1 ± 148.1
MPV fl	6.4 ± 0.5	6.4 ± 0.7	6.4 ± 0.6	6.4 ± 0.6	6.6 ± 0.6	6.5 ± 0.6	6.6 ± 0.5	6.5 ± 0.4	6.5 ± 0.5	6.4 ± 0.6	6.3 ± 0.5	6.4 ± 0.5

†These data include only control RBCs (i.e., those not treated with drugs), including control RBCs used in imaging flow cytometry and mathematical simulations. Paper #2 in table 4 is a subset of the data in Table 4

of the present paper, but restricted to mice that we used in imaging flow cytometry and mathematical simulations.

Results are presented as mean ± SD. Each "N" represents an analysis of the blood from 1 mouse. We performed full hematology screens on fresh blood from WT and KO mice. We analyzed data using a one-way ANOVA, followed by the Holm-Bonferroni (Holm, 1979) correction (see Methods[129]). For each parameter (e.g., MCV), we made all possible comparisons within a row. The only 6 significant differences (indicated by *) involved RhAG-KO vs. WT or dKO vs. WT, and none was sex related. See Supporting file 1 for access to *P*-values for all comparisons.

M, male; F, female; dKO, double knockout; WBC, white blood cells; LYM, lymphocytes; MONO, monocytes; GRAN, granulocytes; Hct, hematocrit; HGB, hemoglobin; RDWa, RBC distribution width–absolute; RDW %; RBC distribution width–percentage; MCH, mean corpuscular hemoglobin; MCV, mean corpuscular volume; MCHC, mean corpuscular hemoglobin concentration; RBC, red blood cells; PLT, platelet; MPV, mean platelet volume.

[129] See Methods>Statistical analysis

Table 5. Summary of automated hematology data obtained from mice used in Inhibitor study†

Parameter \ Mouse	WT			dKO		
N	13			13		
Age weeks	11.9 ± 1.0			11.2 ± 0.7		
groups	Ctrl	pCMBS	DIDS	Ctrl	pCMBS	DIDS
WBC $10^3/\mu l$	3.3 ± 2.8	1.6 ± 0.6	2.2 ± 4.1	6.0 ± 4.6	2.3 ± 1.9*	3.3 ± 1.8
LYM $10^3/\mu l$	2.6 ± 2.3	1.0 ± 0.4	1.7 ± 3.5	4.6 ± 3.9	1.6 ± 1.4*	2.5 ± 1.4
MONO $10^3/\mu l$	0.2 ± 0.2	0.2 ± 0.1	0.2 ± 0.2	0.3 ± 0.2	0.2 ± 0.2	0.1 ± 0.1
GRAN $10^3/\mu l$	0.5 ± 0.4	0.4 ± 0.2	0.3 ± 0.4	1.0 ± 0.9	0.5 ± 0.4	0.6 ± 0.8
LYM %	77.0 ± 3.9	62.4 ± 6.4*	70.4 ± 8.4*	78.0 ± 11.4	65.9 ± 12.0*	77.1 ± 11.9
MONO %	4.0 ± 1.1	9.7 ± 2.1*	4.4 ± 0.7	3.9 ± 1.2	8.2 ± 2.7*	3.5 ± 1.2
GRAN %	19.0 ± 4.0	27.9 ± 5.4*	25.2 ± 8.4*	18.2 ± 11.4	25.8 ± 12.2	19.4 ± 11.2
Hct %	33.1 ± 4.5	34.9 ± 3.4	35.4 ± 3.7	37.0 ± 6.0	39.1 ± 4.5	40.0 ± 4.0
HGB g/dl	10.5 ± 1.1	11.8 ± 0.7*	11.1 ± 0.9	11.3 ± 1.8	12.5 ± 1.3	12.1 ± 1.0
RDWa fl	29.7 ± 2.3	28.7 ± 1.9	31.7 ± 2.4	32.6 ± 1.4	31.8 ± 1.5	35.2 ± 1.7*
RDW %	16.8 ± 0.7	17.6 ± 1.1*	17.3 ± 0.5	16.5 ± 0.5	17.1 ± 0.4*	16.9 ± 0.5*
MCH pg	14.8 ± 0.4	15.0 ± 0.5	15.0 ± 0.5	15.3 ± 0.2	15.4 ± 0.3	15.6 ± 0.4
MCV fl	46.4 ± 3.2	44.3 ± 3.0	47.5 ± 2.8	50.2 ± 0.8	48.2 ± 1.0*	51.8 ± 1.3*
MCHC g/dl	32.1 ± 2.1	34.0 ± 2.1*	31.6 ± 1.6	30.6 ± 0.4	32.0 ± 0.6*	30.2 ± 1.0
RBC $10^6/\mu l$	7.1 ± 0.8	7.9 ± 0.6*	7.4 ± 0.6	7.4 ± 1.2	8.1 ± 0.9	7.7 ± 0.7
PLT $10^3/\mu l$	91.7 ± 87.3	64.7 ± 18.3	85.9 ± 111.5	127.5 ± 113.2	68.0 ± 45.4	84.3 ± 56.0
MPV fl (N)	6.4 ± 1.2 (9)	6.1 ± 0.4 (12)	6.2 ± 0.6 (11)	6.2 ± 1.0 (13)	6.1 ± 0.5 (11)	7.7 ± 1.2* (9)

†These data on 13×2 = 26 mice are the hematology data obtained from mice used in the Inhibitor study, including those used in the imaging flow-cytometry inhibitor studies (see paper #2 in table 6). Because we observed no statistically significant differences between sexes in Table 4, we grouped a males and females (same gender for one pair of WT and dKO mice on that day) for this study.

Results are presented as mean ± SD. Each "N" represents an analysis of the blood from 1 mouse. Samples are tested at ostensibly 50% hematocrit (see Methods[130]). We analyzed data using a one-way ANOVA, followed by the Holm-Bonferroni (Holm, 1979) correction (see Methods[131]). For each parameter (e.g., MCV) from either WT or dKO, we made all possible comparisons between Ctrl, pCMBS and DIDS treatment. * denotes a significant difference compared with Ctrl for the same genotype. See Supporting file 1 for access to *P*-values for all comparisons.

dKO, double knockout; WBC, white blood cells; LYM, lymphocytes; MONO, monocytes; GRAN, granulocytes; Hct, hematocrit; HGB, hemoglobin; RDWa, RBC distribution width–absolute; RDW%; RBC distribution width –percentage; MCH, mean corpuscular hemoglobin; MCV, mean corpuscular volume; MCHC, mean corpuscular hemoglobin concentration; RBC, red blood cells; PLT, platelet; MPV, mean platelet volume.

[130] See Methods>Automated hematological analyses (workflow #7 – #9)>Use of inhibitors in automated hematological studies

[131] See Methods>Statistical analysis

Figure Legends

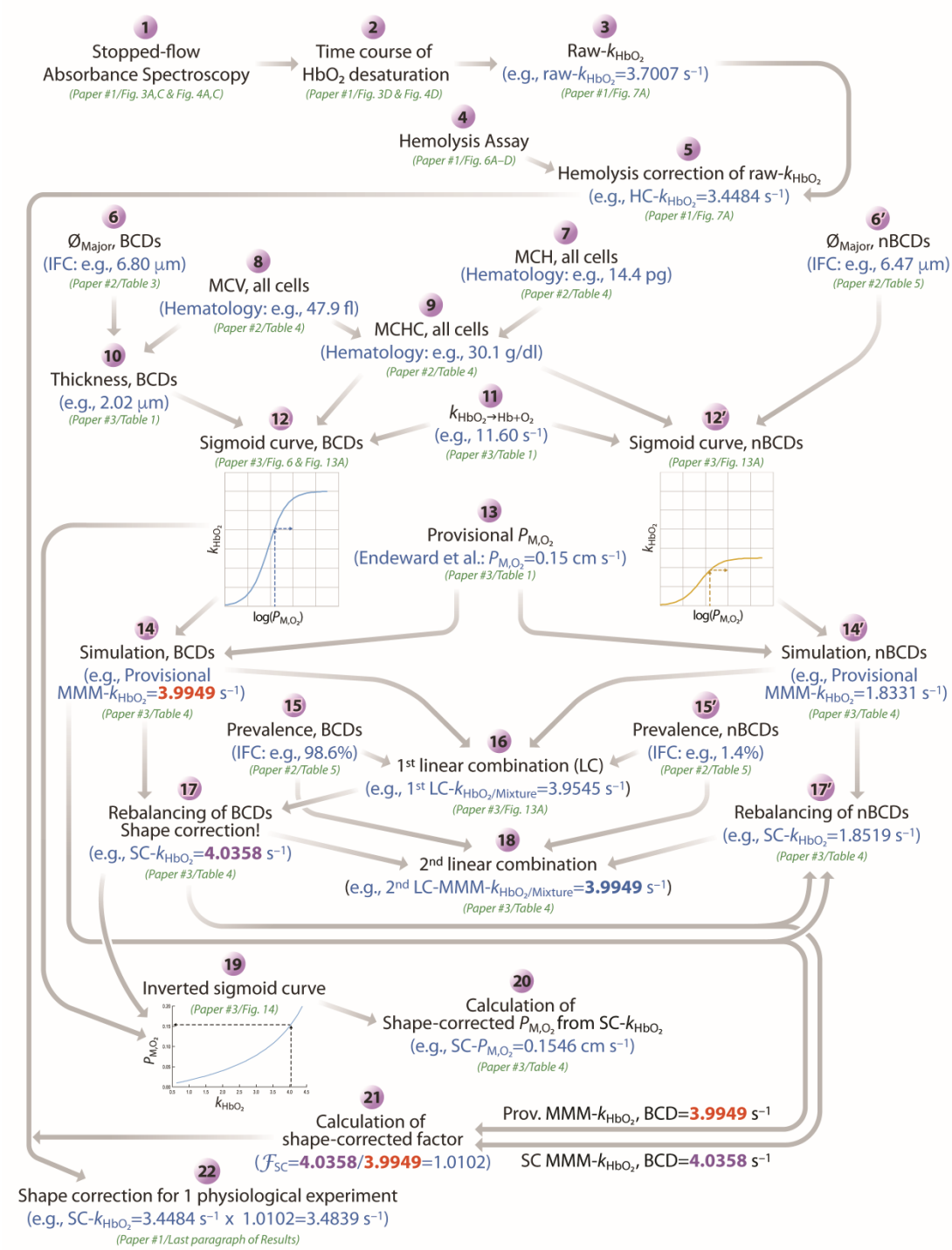

Figure 1. Workflow to obtain hemolysis-corrected and shape-corrected values of P_{M,O_2}

The numerals 1 through 22 indicate the steps summarized in the present paper—and presented in detail, as

appropriate, in the present paper (paper #1), paper #2, or paper #3—to arrive, first, at a hemolysis-corrected (HC) k_{HbO_2} and, ultimately, at a shape-corrected (SC) k_{HbO_2}. At each step, we provide example values, if possible, and example figure/table numbers referenced to the present paper, paper #2, or paper #3.

We repeat workflow steps 1–5 for each mouse, ultimately arriving at an HC-k_{HbO_2} value for each. Step 6 applies to biconcave disks (BCDs), whereas step 6′ applies to non-biconcave disks (nBCDs). The same is true for steps 12 vs. 12′, 14 vs. 14′, 15 vs. 15′, and for 17 vs. 17′.

$\mathcal{F}_{SC}$, shape-correction factor; Hb, hemoglobin; IFC, imaging flow cytometry; MCH, mean corpuscular hemoglobin; k_{HbO_2}, rate constant for deoxygenation of HbO_2 within intact RBCs; $k_{HbO_2 \rightarrow Hb+O_2}$, rate constant for deoxygenation of HbO_2 in free solution; LC, linear combination; MCH, mean corpuscular hemoglobin; MCHC, mean corpuscular hemoglobin concentration; MCV, mean corpuscular volume; MMM-k_{HbO_2}, macroscopic mathematically modeled rate constant for deoxygenation of intracellular HbO_2; P_{M,O_2}, membrane permeability to O_2; Prov., provisional; $Ø_{Major}$, major diameter (of BCD or nBCD); SC-k_{HbO_2}, shape-corrected rate constant for deoxygenation of intracellular HbO_2.

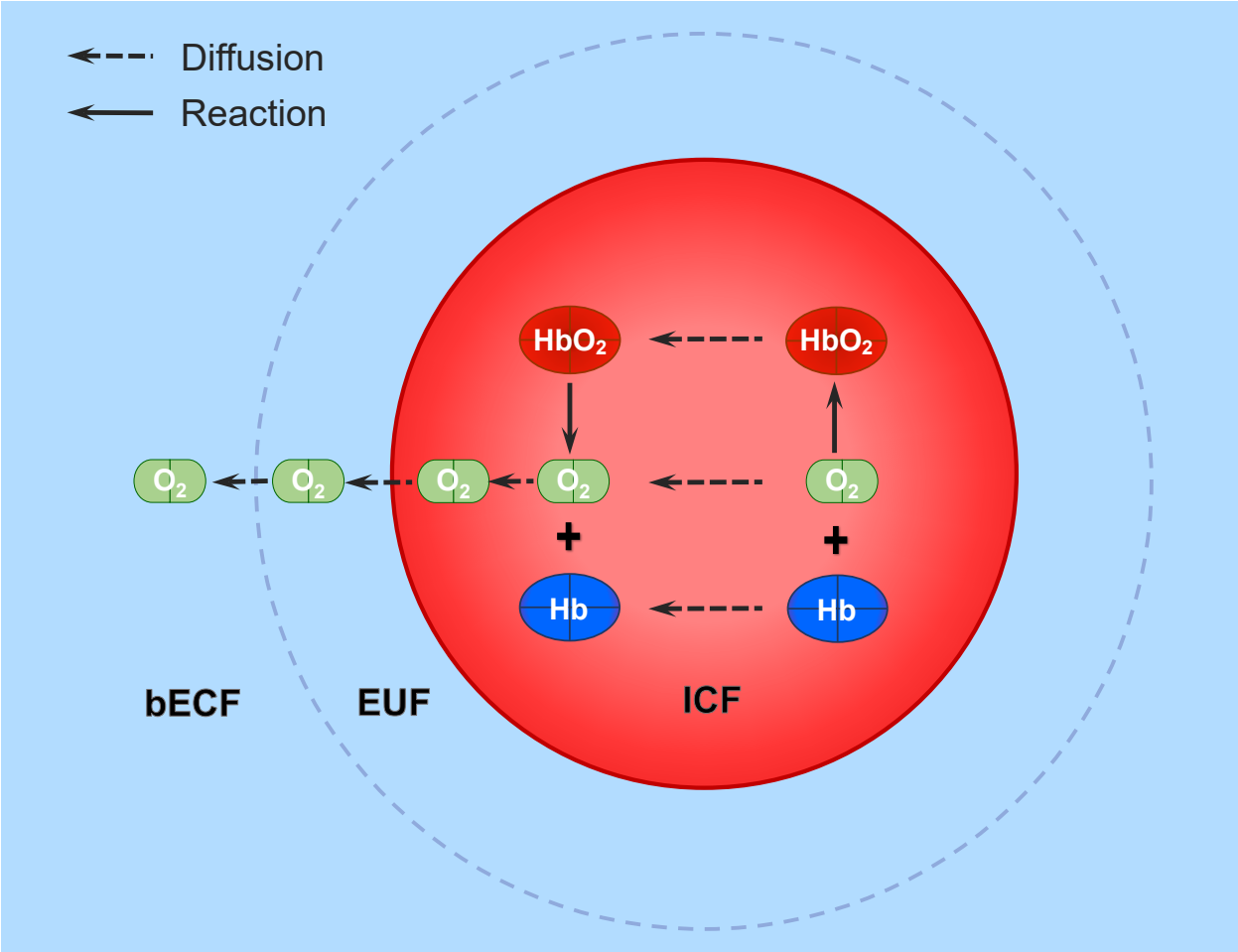

Figure 2. Model of O_2 offloading from an RBC

The model system comprises (1) a spherical RBC, (2) a plasma membrane (red circle), (3) intracellular fluid (ICF), (4) Hb and HbO_2 within the ICF, (5) a thin layer of extracellular unconvected fluid (EUF) just external to the PM, (6) an infinite reservoir of bulk extracellular fluid (bECF) that surrounds the EUF and is indicated by grey dashed circle, and (7) O_2 throughout the system. Arrows: solid black line represents reaction; dashed black line represents diffusion.

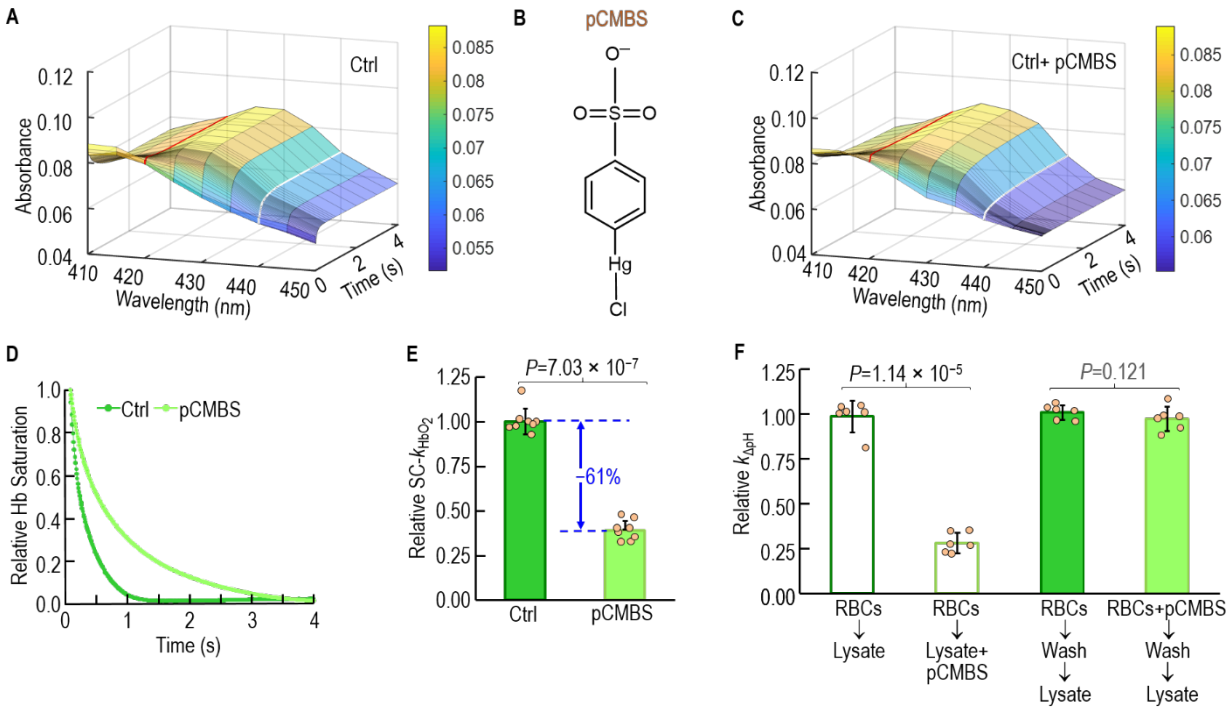

Figure 3. Effect of extracellular pCMBS on rate constant of deoxygenation of intracellular hemoglobin (k_{HbO_2}) during O_2 efflux from RBCs

A, Representative time course of hemoglobin absorbance spectra during deoxygenation of ostensibly intact wild-type (WT) RBCs under control conditions (Ctrl; absence of drugs). It is from a collection of spectra such as these that we compute raw-k_{HbO_2}.

B, Structural formula of p-chloromercuribenzenesulfonate (pCMBS).

C, Representative collection of absorbance spectra, as in panel *A*, except from WT cells treated with p-chloromercuribenzenesulfonate (pCMBS).

D, Time courses of relative hemoglobin desaturation (see Methods[132]) for the same two data sets in the previous panels.

E, Summary of effect of pCMBS on relative k_{HbO_2} in intact RBCs, corrected for both hemolysis (see Methods

[132] See Methods>Calculation of time course of HbO_2 desaturation (workflow #2)>Apply weighting factors

[133]) and shape changes (see Methods[134]). The absolute SC-k_{HbO2} underlying the Ctrl bar for this data set is $3.45 \pm 0.25\ s^{-1}$. Bars represent mean ± SD, N=8.

F, Exclusion of pCMBS from RBC cytosol. Wash solution contained 0.2% bovine serum albumin. Bars represent mean ± SD, N=6.

For *E & F,* each bar-associated point represents RBCs from 1 WT mouse. Bars represent mean ± SD. We performed paired t-tests (see Methods[135]).

---

[133] See Methods>Accommodation for hemolysis (workflow #5)

[134] See Methods>Accommodation for nBCDs (workflow #13 – #22)

[135] See Methods>Statistical analysis

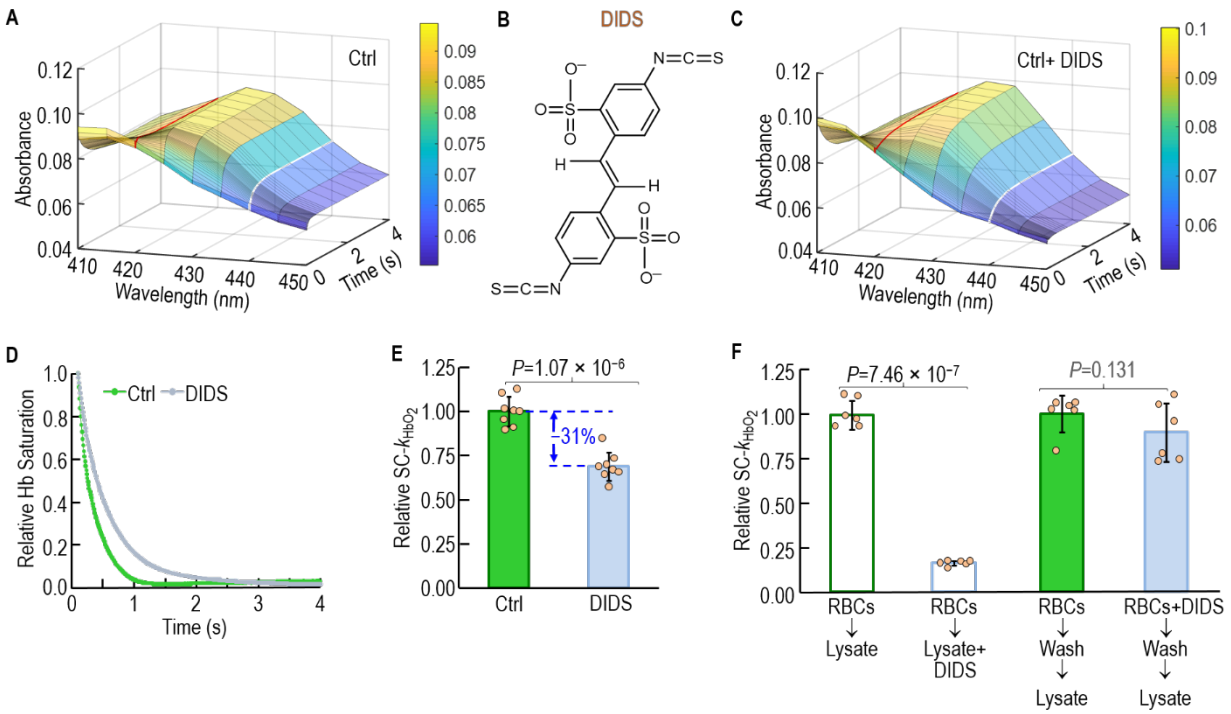

Figure 4. Effect of extracellular DIDS on rate constant of deoxygenation of intracellular hemoglobin (k_{HbO_2}) during O_2 efflux from RBCs

A , Representative time courses of hemoglobin absorbance spectra during deoxygenation of ostensibly intact control wild-type RBCs. We compute raw-k_{HbO_2} from a collection of spectra such as these.

B, Structural formula of DIDS.

C, Representative collection of absorbance spectra, as in panel *A*, except from WT cells treated with 4,4'-diisothiocyanatostilbene-2,2'-disulfonate (DIDS).

D, Time courses of relative hemoglobin saturation (see Methods[132]) for the same two data sets in the previous panels.

E, Summary of effect of DIDS on relative k_{HbO_2} in intact RBCs, corrected for both hemolysis (see Methods[133]) and shape changes (see Methods[134]). The absolute SC-k_{HbO2} underlying the Ctrl bar for this data set is 3.24 ± 0.27 s^{-1}. Bars represent mean ± SD, N=8.

F, Exclusion of DIDS from RBC cytosol. For the data underlying the two open bars, after preparing an osmotic

lysate (see Methods[136]), we pretreated the hemoglobin (Hb) ± 200 μM DIDS for 60 min (see Methods[137]), and determined the rate constant (k_{HbO_2}) for hemoglobin deoxygenation as described in Methods[138]. For the experiments underlying the two filled bars, the wash solution contained 0.2% bovine serum albumin. Bars represent mean ± SD, N=6.

For *E & F,* each bar-associated point represents RBCs from 1 WT mouse. Bars represent mean ± SD. We performed paired t-tests (see Methods[135]).

---

[136] See Methods>Preparation of RBCs>Processing of RBCs for stopped-flow studies>"osmotic lysis" in text

[137] See Methods>Preparation of RBCs>Use of inhibitors in stopped-flow studies

[138] See Methods>Calculation of raw-k_{HbO_2} (workflow #3)

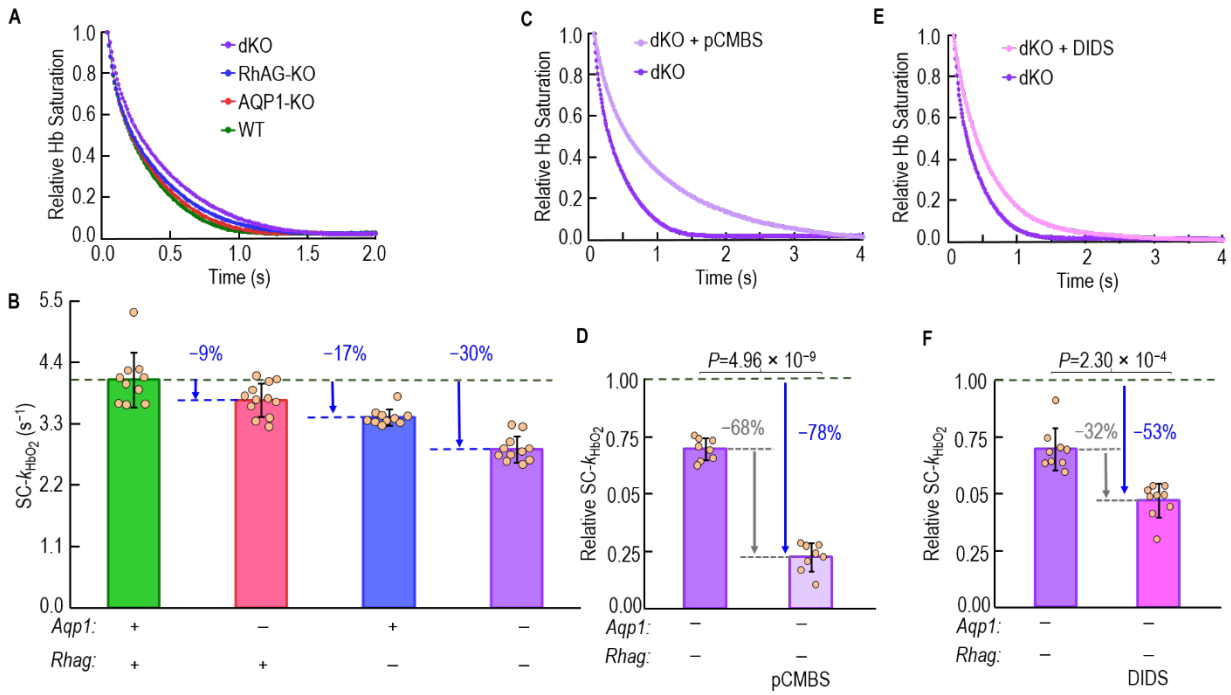

Figure 5. Effect of genetic deletions of *Aqp1*, *Rhag*, or both on rate constant of deoxygenation of intracellular hemoglobin (k_{HbO_2}) during O_2 efflux from RBCs

A, Representative time courses of hemoglobin desaturation of ostensibly intact RBCs from WT mice and those with genetic deletions of *Aqp1*, *Rhag* or both. It is from these time courses that we compute raw-k_{HbO_2}.

B, Summary of mean shape-corrected k_{HbO2} (SC-k_{HbO2}) values for the full data set of which panel *A is* representative. The absolute SC-k_{HbO2} underlying the +/+ green bar for the data set in panels *B* is 4.09 ± 0.49 s^{-1}. Bars represent mean ± SD, N=10 for green bar, N=12 for red bar, N=10 for blue bar and N=11 for purple bar. We present *P*-values for all the comparisons of SC-k_{HbO2} in Figure 5*B* (same data sets shown in Table 3*B* of SC-k_{HbO2}) in Statistics Table 1.

C & E, Representative time courses of hemoglobin desaturation of ostensibly intact RBCs, untreated or pretreated with either pCMBS (panel *C*) or DIDS (panel *E*) from dKO mice. It is from these time courses that we compute raw-k_{HbO_2}.

D & F, Summary of mean SC-k_{HbO2} for two full data sets of which panels *C & E* are representative. We normalize each of the two purple bars to the height of the purple bar in panel *B*, and appropriately scale the pCMBS and DIDS bars. The three purple bars in panels *B, D, and F* are from three different data sets. The absolute SC-k_{HbO2} for the +/+ control RBCs (not shown here), to which we reference the two purple bars are 2.63 ± 0.18 s^{-1} for panel *D*, and 2.52 ± 0.34 s^{-1} for panel *F*. These reference data are in paper #3>table 4. Bars represent mean ± SD, N=8 for panel *D*, N=9 for panel *F*.

For panels *B*, *D*, and *F*, each bar-associated point represents RBCs from 1 mouse, with an independent hemolysis correction (see Methods[133]). For *B,* we performed a one-way ANOVA, followed by a Holm-Bonferroni correction (see Methods[135]). For *D & F,* we performed paired t-tests (see Methods[135]).

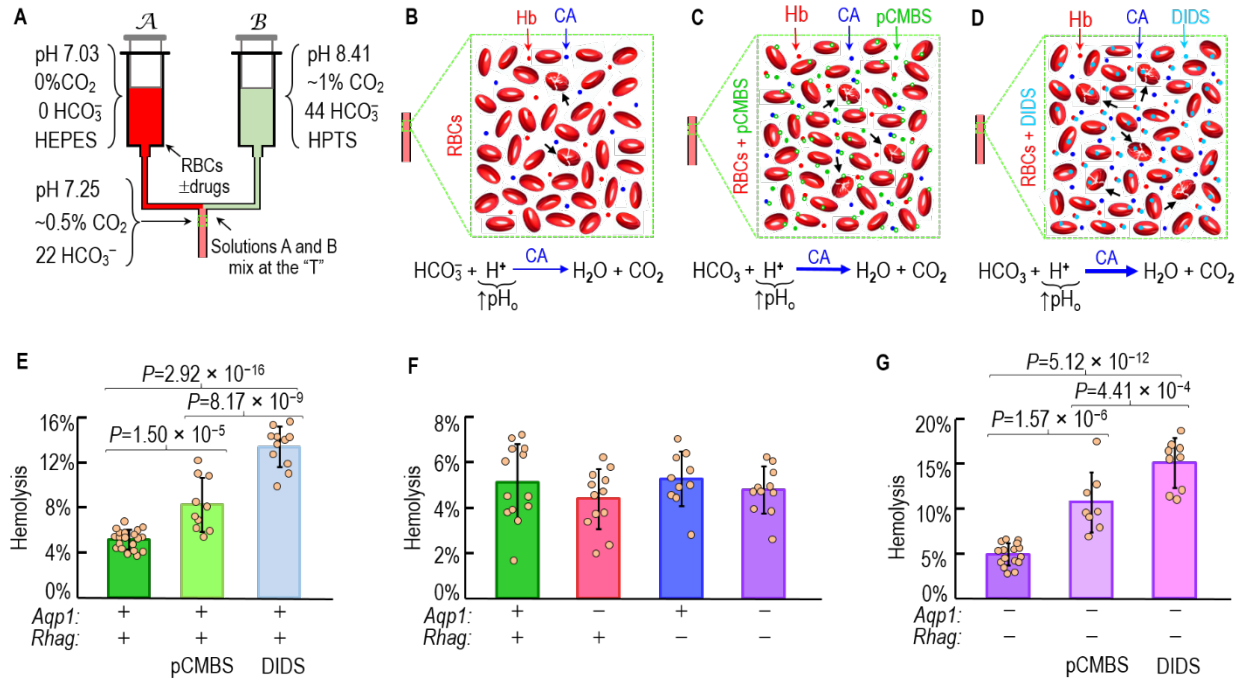

Figure 6. Degree of hemolysis in experiments on ostensibly intact RBCs

A, Schematic diagram of CO_2/HCO_3^- out-of-equilibrium (OOE) studies in stopped-flow (SF) apparatus. Solutions $\mathcal{A}$ and $\mathcal{B}$ mix at the "T" and thereby create, in the SF cell, a new solution that is out of equilibrium with ~0% CO_2/22 mM HCO_3^-/pH 7.25 at 10°C.

B, Control cells (without drugs). Upper panel, schematic diagram of Ctrl RBCs in an SF cell. Hemolysis is typically 0.4% as we load RBCs into the SF machine. However, in the SF reaction cell, actual hemolysis rises to ~5%. The lysed cells (black Arrows) release both hemoglobin (Hb, red dots) and carbonic anhydrases (CAs, blue dots).

Lower panel, CO_2/HCO_3^- reaction. Starting from the OOE state, HCO_3^- and H^+ combine to form CO_2 and H_2O. Overall reaction is greatly accelerated by the CAs released along with Hb from the lysed RBCs. Our hemolysis assay (Zhao *et al.*, 2017) is based on the rate constant of the pH increase ($k_{\Delta pH}$) caused by this reaction.

C, pCMBS-treated cells. Upper panel, schematic diagram of pCMBS-treated RBCs in an SF cell. Actual hemolysis in the SF reaction cell is ~8% for pCMBS-treated RBCs from WT mice. The small amount of lysis that occurs during the 15-min pCMBS preincubation period, before the cells enter the SF reaction cell (~0.4%), releases CA that reacts extensively with pCMBS, markedly reducing that enzymatic activity (see Figure 3*F*, open pair of bars). Later, free pCMBS enters the SF reaction cell and is exposed to a much higher levels of CA from RBCs that lyse in the SF reaction cell (~7.5%), but only for a very brief period (100's of ms). Thus, pCMBS reacts with only a tiny fraction of the newly released CA, so that extracellular CA activity is high in the SF reaction cell. The filled green color dots indicate free pCMBS, whereas the open green dots represent Hg that has reacted with the cell surface, released CA (blue dots), or released Hb (red dots).

Lower panel, CO_2/HCO_3^- reaction. Elevated extracellular CA activity from the increased hemolysis speeds

the reaction and increases $k_{\Delta pH}$, and reports the elevated hemolysis.

D, DIDS-treated cells. Upper panel, schematic diagram of DIDS-treated RBCs in an SF cell. Actual hemolysis in the SF reaction cell is ~13.4% for DIDS-treated RBCs from WT mice. Unlike pCMBS (panel *C*), DIDS has little effect on CA activity, so that the chemistry of the hemolysis assay is basically the same as in panel *B*. (Note that DIDS does react with Hb as shown in Figure 4*F* but HbO_2 deoxygenation is not part of our hemolysis assay). The filled teal-colored dots indicate DIDS, some of which remains free, and some of which has reacted with the cell surface and released Hb, but not released CA.

Lower panel, CO_2/HCO_3^- reaction. Because hemolysis is greater than with pCMBS in panel *C*, $k_{\Delta pH}$ is greater.

E, Summary of hemolysis in experiments on WT-mouse RBCs, either controls or cells treated with pCMBS or DIDS. RBCs were treated with 1 mM pCMBS for 15 min or 200 μM DIDS for 60 min. N=20 for green bar, N=10 for light green bar and N=11 for gray-blue bar.

F, Summary of hemolysis in experiments on control mouse RBCs of all four genotypes used in the present study. Note the compressed scale of the y-axis, compared to panel *A*, which has bars for pCMBS- or DIDS-treated cells. The RBCs from WT-mice here in panel *F* represent a different data set than in panel *E*. N=13 for green bar, N=12 for red bar, N=10 for blue bar and N=11 for purple bar. We present *P*-values for all statistical comparisons in Statistics Table 2.

G, Summary of hemolysis in experiments on RBCs from double-knockout mice, either controls or cells treated with pCMBS or DIDS. N=17 for purple bar, N=8 for light purple bar and N=9 for pink bar.

In panels *E*, *F*, and *G*, each bar-associated point represents 1 mouse. Bars represent mean ± SD. We performed a one-way ANOVA, followed by the Holm-Bonferroni correction (see Methods[135]).

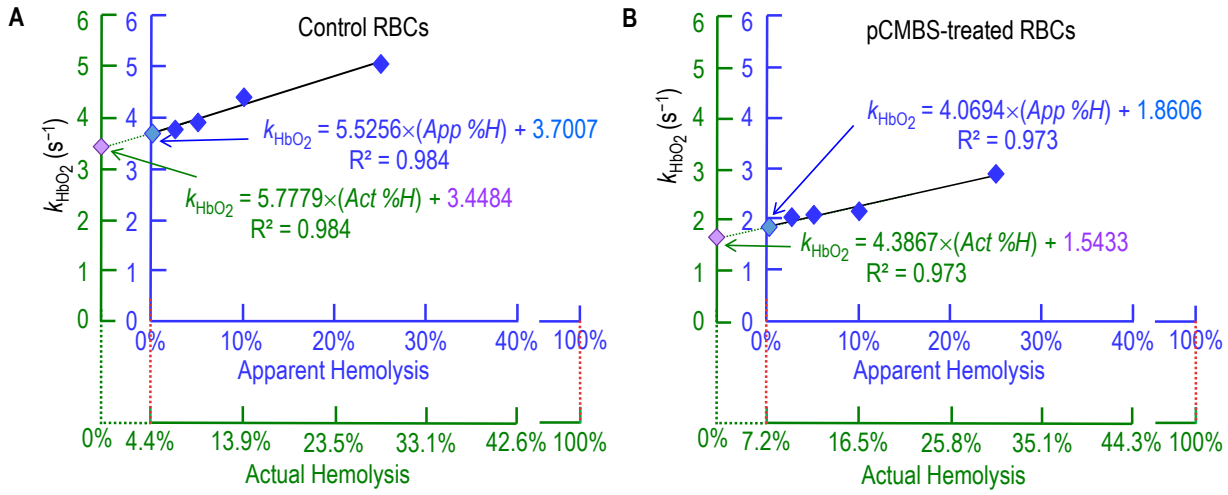

Figure 7. Accommodation of raw-k_{HbO_2} for hemolysis in experiments on ostensibly intact RBCs, either without inhibitors (*A*), or pretreated with pCMBS (*B*) on blood from the same WT mouse

The raw rate constant (k_{HbO_2}) is a mixture of contributions from (1) the relatively slow deoxygenation of cytosolic HbO_2 in truly intact RBCs and (2) the relatively rapid deoxygenation of extracellular HbO_2 released from hemolyzed RBCs. Here, we use a novel approach to correct raw-k_{HbO_2} for hemolysis in a series of five steps:

(1) Use the assays in Figure 6 to determine actual percent hemolysis (*Act%H*) of ostensibly 100%-intact RBCs as described in Methods[139] for control RBCs (4.4% on green x-axis for mouse in panel *A*) and pCMBS-treated RBCs (7.2% on green x-axis for mouse in panel *B*).

(2) Determine k_{HbO_2} for ostensibly 100%-intact RBCs—that is, apparent percent hemolysis [*App%H*] = 0%—as described in Methods[140]. These are the light-blue diamonds with the black perimeters in panels *A* and *B* (on the blue y-axes).

(3) Determine k_{HbO_2} for mixtures of ostensibly intact RBCs (97.5%, 95%, 90%, and 75%) and fully hemolyzed RBCs (2.5%, 5%, 10%, and 25%) to keep total [Hb] = 2.5 μM in the SF reaction cell. The *App%H* values are on the blue x-axes.

(4) Rescale and translate the blue *App%H* axes to obtain the green *Act%H* axes for mixtures of ostensibly 100%-intact RBCs and 100% hemolysate: (*Act%H*) = (*App%H*) + ($Act\%H_{App\%H=0\%}$)*(100% – *App%H*).

---

[139] See Methods> Quantitation of hemolysis in SF reaction cell (workflow #4)

[140] See Methods>Calculation of raw-k_{HbO_2} (workflow #3)

(5) Back-extrapolate k_{HbO_2} to *Act%H* = 0% to obtain hemolysis-corrected k_{HbO2} values (lavender diamonds), which for the sample in panel *A* was 3.45 s^{-1} for control RBCs and, for the sample in panel *B*, 1.54 s^{-1} for pCMBS-treated RBCs. We repeat this analysis for each mouse.

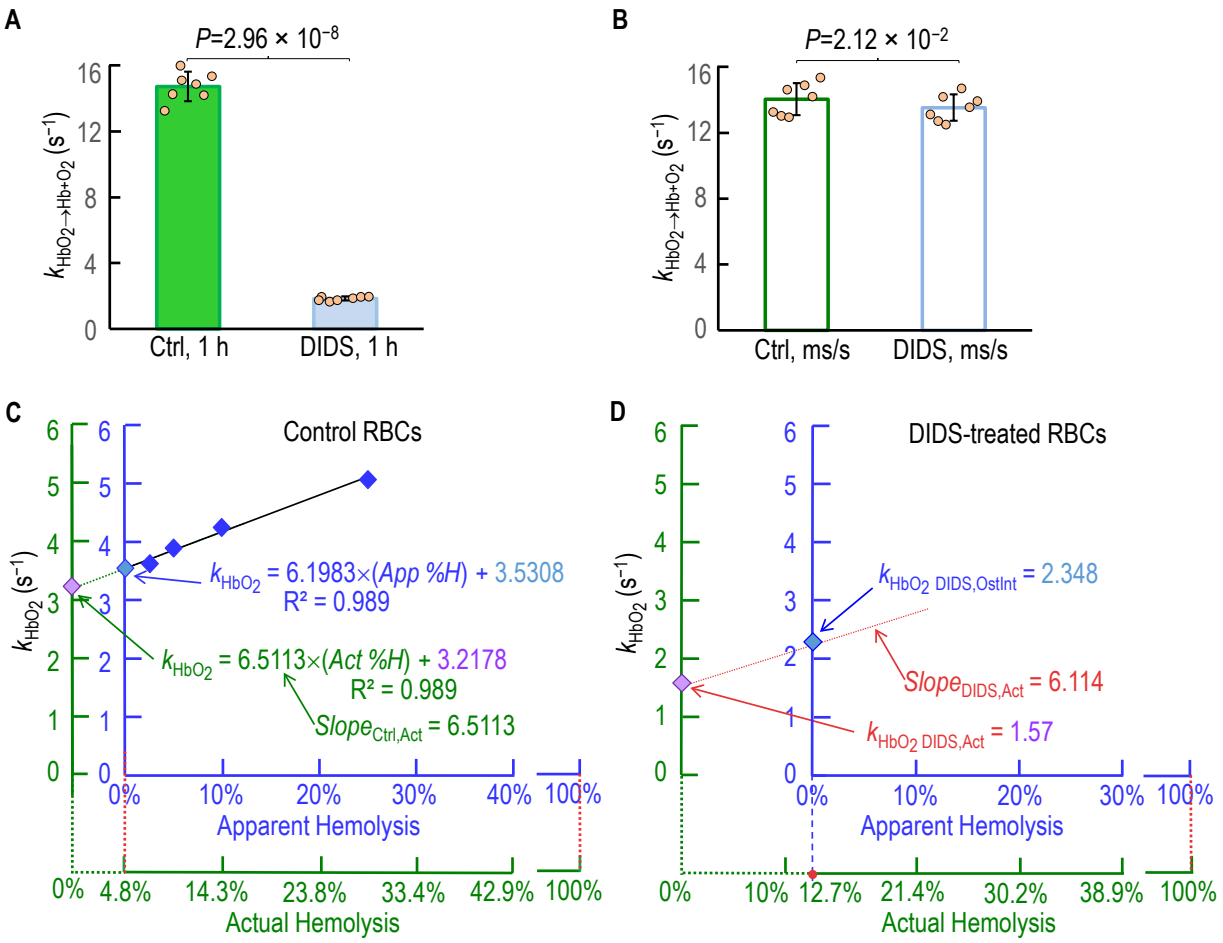

Figure 8. Correction of k_{HbO_2} for hemolysis in experiments on RBCs treated with DIDS

A, Effect of DIDS on k_{HbO_2} in a 100% hemolysate over a 1-hour time frame. This experiment is basically the same as the one summarized by the two open bars in Figure 4*F*, but on a different data set. After preparing an osmotic lysate (see Methods[136]), we pretreated the hemoglobin (Hb) ±200 μM DIDS for 60 min (see Methods[137], and determined the rate constant (k_{HbO_2}) for hemoglobin deoxygenation as described in Methods[138].

B, Effect of DIDS on k_{HbO_2} in a 100% hemolysate over millisecond-to-second timeframe. After (1) preparing an osmotic lysate as in panel *A*, we (2) diluted the hemolysate in our oxygenated solution and the DIDS (200 μM final concentration) in our deoxygenated solution (see Table 2) as described in Methods[141], and (3)

[141] See Methods>Preparation of RBCs>Use of inhibitors in stopped-flow studies>"millisecond-to-second DIDS exposures" in text

after rapid mixing of hemolysate and DIDS in the SF reaction cell, (4) determined k_{HbO2} as in panel *A*.

For *A* & *B,* each bar-associated point represents RBCs from 1 WT mouse. Bars represent mean ± SD. Ctrl, control (i.e., no drugs). N=7 for each group. We performed paired t-tests.

C, Determination of control slope ($Slope_{Ctrl,Act}$) in plot of k_{HbO_2} vs. actual percent hemolysis (*Act%H*, green) for RBCs without inhibitors. This is the same protocol as in Figure 7*A*, though on a different data set. The Extrapolation of the k_{HbO_2} data back to *Act%H* = 0% yields an actual k_{HbO_2} (lavender diamond on green y-axis), which in this example was 3.22 s^{-1} for control RBCs.

D, Correction of k_{HbO_2} for hemolysis in experiments on RBCs pretreated with DIDS. We determined raw-k_{HbO_2} values for ostensibly "100%-intact" RBCs as described for panel *C*. For the sample here in panel *D* (from same mouse as in panel *C*), this uncorrected value (blue diamond on blue y-axis) was ~2.35 s^{-1} for DIDS-treated RBCs. We calculate the slope ($Slope_{DIDS,Act}$) of the regression line (red dashed line) using the data in panel *C*, as described in Methods[142]. Extrapolation of this line yields a hemolysis-corrected k_{HbO_2} (indicated as lavender diamond (on green y-axis) for $k_{HbO_2\ DIDS,Act}$) of ~1.57 s^{-1}.

[142] See Methods>Accommodation for hemolysis (workflow #5)>DIDS-treated RBCs

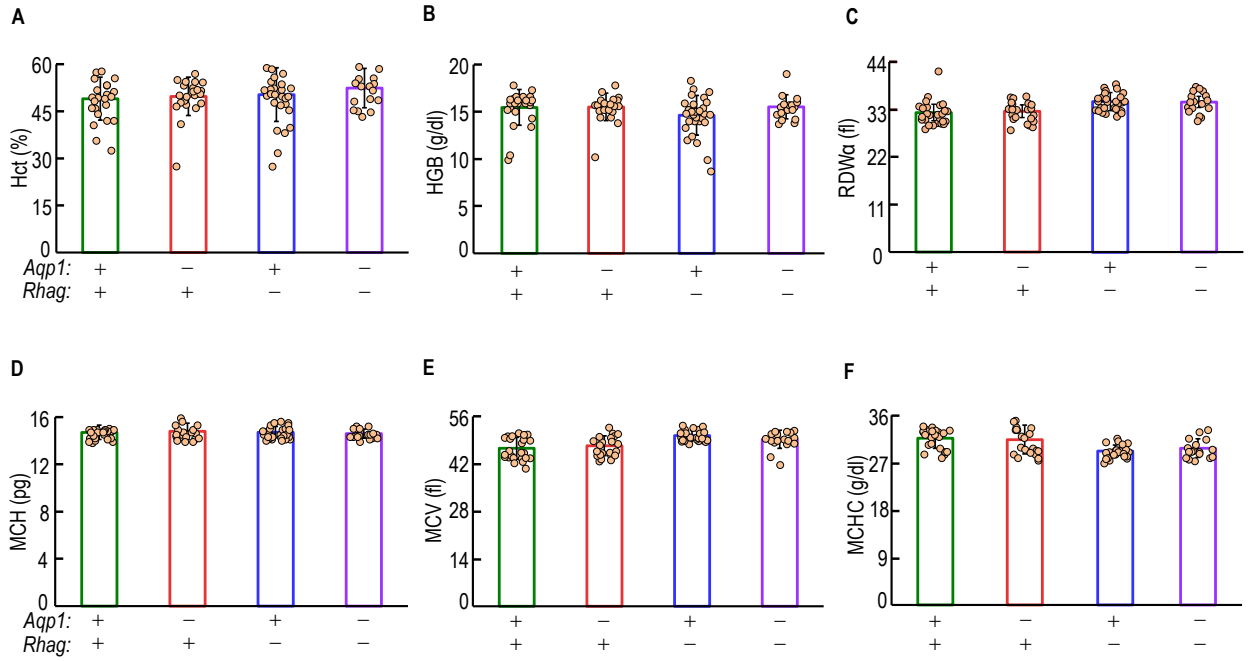

Figure 9. Effect of genetic deletions of *Aqp1*, *Rhag*, or both on key hematological parameters

The bar graphs summarize key parameter values—with data from both sexes combined—from automated hematological analyses. See Table 4 for the detailed data, separated by sexes, on WT, *Aqp1*–/–, *Rhag*–/–, and dKO mice).

A, Hematocrit (Hct).

B, Hemoglobin (HGB).

C, RBC distribution width—absolute (RDWa).

D, Mean corpuscular hemoglobin content (MCH).

E, Mean corpuscular volume (MCV).

F, Mean corpuscular hemoglobin concentration (MCHC).

Each bar-associated point represents RBCs from 1 mouse. Bars represent mean ± SD. N=24 for green open bar, N=22 for red open bar, N=29 for blue open bar and N=17 for purple open bar. We performed a one-way ANOVA, followed by the Holm-Bonferroni correction (see Methods[135]). We present *P*-values for all statistical comparisons in for panels *A*-*F* in Statistics Table 3.

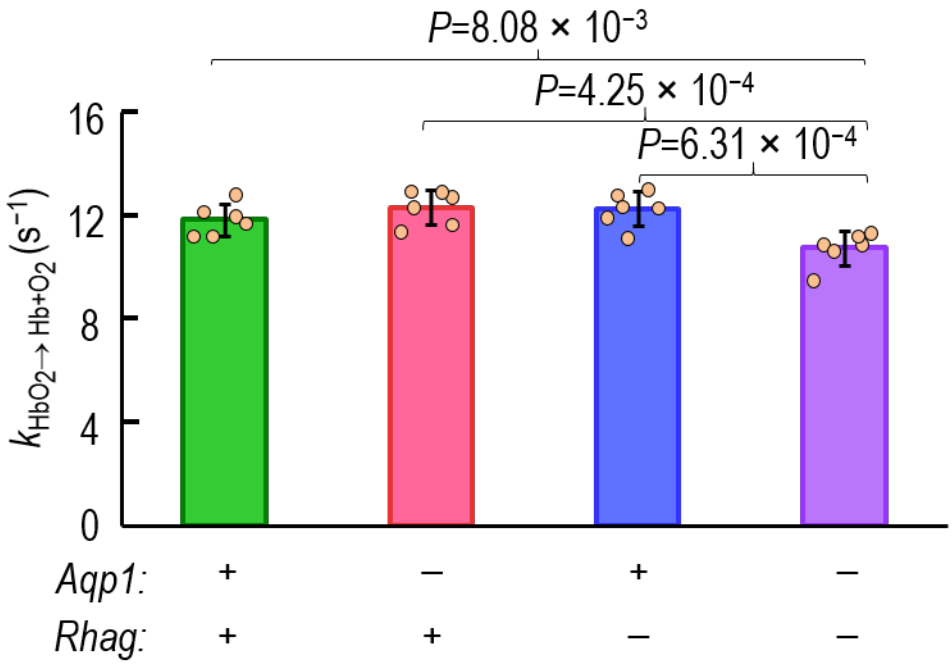

Figure 10. Effect of genetic deletions of *Aqp1*, *Rhag*, or both on rate constant of the reaction $HbO_2 \rightarrow Hb + O_2$ ($k_{HbO_2 \rightarrow Hb+O_2}$) in RBC lysates

See Methods[143] for a description of how we measure k_{HbO_2}. The approach here was similar, except that we worked with 100% hemolysates (see Methods[136]). Each bar-associated point represents RBCs from 1 mouse. Bars represent mean ± SD. N=6 for each bar. We performed a one-way ANOVA, followed by a Holm-Bonferroni correction (see Methods[135]). We present *P*-values for all statistical comparisons in Statistics Table 4.

[143] See (a) Methods>Calculation of time course of HbO_2 desaturation (workflow #2) & (b) ..>Calculation of raw-k_{HbO_2} (workflow #3)

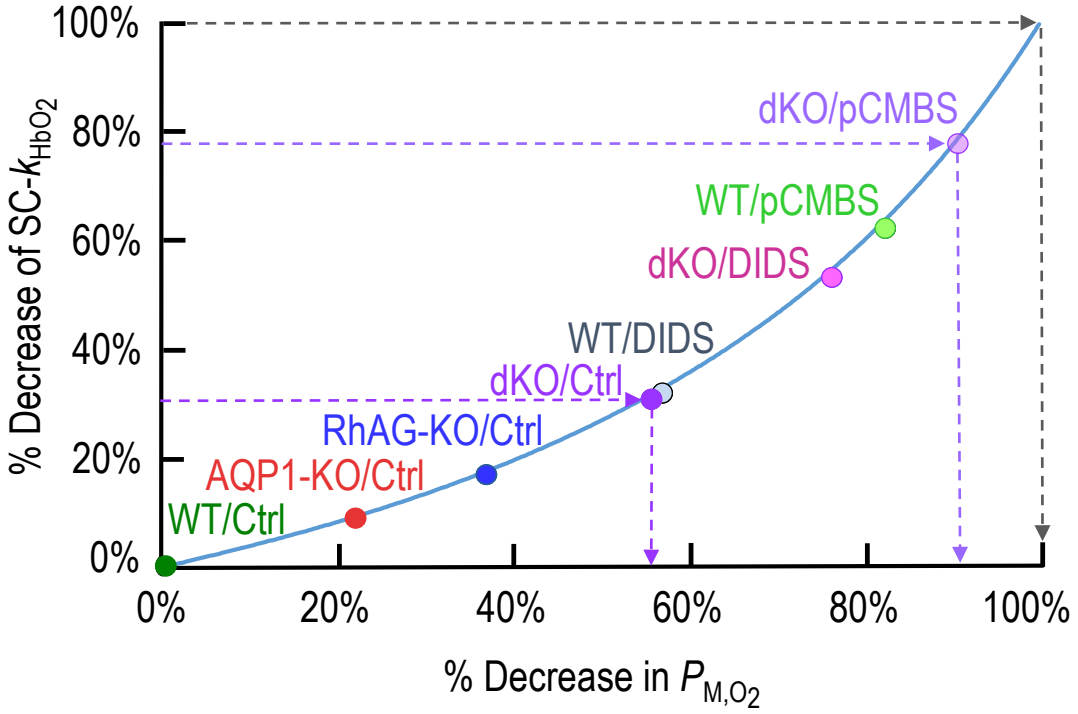

Figure 11. Dependence of percent decrease of k_{HbO_2} on percent decrease of P_{M,O_2} from macroscopic mathematical modeling and simulations

Effect of decreasing the O_2 permeability of the RBC membrane (P_{M,O_2}) on the predicted shape-corrected (SC) k_{HbO_2}. We reference both the % decrease in k_{HbO_2} (equivalent to the shape-corrected value of a physiological experiment) and the % decrease in P_{M,O_2} (equivalent to the inhibition produced by a KO and/or drug) to their respective values for control (Ctrl; i.e., without inhibitors) RBCs from a wild-type (WT) mouse. Note: this plot is a transformation of the sigmoidal MMM-k_{HbO_2} vs. log(P_{M,O_2}) modeling/simulation data in figure 6 in paper #3. Using our reaction-diffusion model (see paper #3[144]), we simulate the time course of HbO_2 desaturation, employing hematological and morphological data gathered for RBCs from WT mice. We then systematically decrease P_{M,O_2} (x-axis), and compute the predicted % decrease in k_{HbO_2} (y-axis; blue curve). For each of our 8 experimental conditions (labeled points), we use experimentally determined SC-k_{HbO_2} values to determine position on the y-axis, and then place the point on the blue curve. Dropping a perpendicular to the x-axis reveals the % decrease in P_{M,O_2}. Thus, the observed ~78% decrease in SC-k_{HbO_2} for dKO/pCMBS (middle horizontal arrow) corresponds to a ~91% decrease in P_{M,O_2} (middle downward arrow).

[144] Paper #3>Methods>Mathematical modeling and simulations

Statistics Tables

We use one-way ANOVA with Holm-Bonferroni post-hoc means comparison for the mean Raw k_{HbO2} values, the mean hemolysis-corrected k_{HbO2} (HC-k_{HbO2}) values and the mean shape-corrected k_{HbO2} (SC-k_{HbO2}) values of all four mouse strains. Each table is split in two halves, with FWER set at 0.05, the upper half shows the adjusted α-value for each comparison and the lower half the *P*-value. Significant *P*-values are highlighted bold.

Statistics Table 1: *P*-values for Table 3*B*

Comparison of Raw-k_{HbO2}

Mouse		WT	AQP1-KO	RhAG-KO	dKO
	P \ α		α	α	α
WT			0.0250	0.0125	0.00833
AQP1-KO	*P*	**6.57×10^{-3}**		0.0500	0.0100
RhAG-KO	*P*	**7.94×10^{-5}**	0.0912		0.0167
dKO	*P*	**3.32×10^{-10}**	**1.02×10^{-6}**	**4.52×10^{-4}**	

Comparison of HC-k_{HbO2}

Mouse		WT	AQP1-KO	RhAG-KO	dKO
	P \ α		α	α	α
WT			0.0250	0.0125	0.00833
AQP1-KO	*P*	**8.36×10^{-3}**		0.0500	0.0100
RhAG-KO	*P*	**1.83×10^{-5}**	**2.58×10^{-2}**		0.0167
dKO	*P*	**2.72×10^{-11}**	**4.59×10^{-8}**	**1.56×10^{-4}**	

Comparison of SC-k_{HbO2} (same for Fig 5*B*)

Mouse		WT	AQP1-KO	RhAG-KO	dKO
	P \ α		α	α	α
WT			0.0250	0.0167	0.00833
AQP1-KO	*P*	**5.22×10^{-5}**		0.0500	0.0100
RhAG-KO	*P*	**2.92×10^{-7}**	**0.0481**		0.0125
dKO	*P*	**1.37×10^{-15}**	**1.01×10^{-11}**	**1.21×10^{-8}**	

Statistics Table 2: *P*-values for Figure 6*F*

Comparison of hemolysis

Mouse		WT	AQP1-KO	RhAG-KO	dKO
	P \ α		α	α	α
WT			0.0100	0.0500	0.0250
AQP1-KO	*P*	0.199		0.00833	0.0167
RhAG-KO	*P*	0.761	0.136		0.0125
dKO	*P*	0.575	0.489	0.415	

Statistics Table 3: *P*-values for Figure 9

Comparison of panel *A* for Hct

Mouse		WT	AQP1-KO	RhAG-KO	dKO
	P \ α		α	α	α
WT			0.0250	0.0167	0.00833
AQP1-KO	*P*	0.716		0.0500	0.0100
RhAG-KO	*P*	0.512	0.795		0.0125
dKO	*P*	0.135	0.255	0.335	

Comparison of panel *B* for HGB

Mouse		WT	AQP1-KO	RhAG-KO	dKO
	P \ α		α	α	α
WT			0.0250	0.01	0.0167
AQP1-KO	*P*	0.929		0.00833	0.0500
RhAG-KO	*P*	0.0903	0.0813		0.0125
dKO	*P*	0.916	0.981	0.101	

Comparison of panel *C* for RDWα

Mouse		WT	AQP1-KO	RhAG-KO	dKO
	P \ α		α	α	α
WT			0.0250	0.00833	0.0125
AQP1-KO	*P*	0.666		0.0100	0.0167
RhAG-KO	*P*	**1.60×10^{-4}**	**1.02×10^{-2}**		0.0500
dKO	*P*	**1.72×10^{-3}**	**6.67×10^{-3}**	0.835	

Comparison of panel *D* for MCH

Mouse		WT	AQP1-KO	RhAG-KO	dKO
	P \ α		α	α	α
WT			0.0125	0.05	0.0167
AQP1-KO	*P*	0.556		0.0250	0.00833
RhAG-KO	*P*	0.953	0.577		0.0100
dKO	*P*	0.559	0.267	0.510	

Comparison of panel *E* for MCV

Mouse		WT	AQP1-KO	RhAG-KO	dKO
	P \ α		α	α	α
WT			0.0500	0.00833	0.0125
AQP1-KO	*P*	0.342		0.0100	0.0167
RhAG-KO	*P*	**9.05×10^{-7}**	**7.32×10^{-5}**		0.0250
dKO	*P*	**1.89×10^{-3}**	0.0254	0.151	

Comparison of panel *F* for MCHC

Mouse		WT	AQP1-KO	RhAG-KO	dKO
	P \ α		α	α	α
WT			0.0500	0.00833	0.0125
AQP1-KO	*P*	0.642		0.0100	0.0167
RhAG-KO	*P*	**1.53×10^{-5}**	**1.40×10^{-4}**		0.0250
dKO	*P*	**2.48×10^{-3}**	**1.00×10^{-2}**	0.368	

Statistics Table 4: *P*-values for Figure 10

Comparison of rate constant of the reaction $HbO_2 \rightarrow Hb + O_2$ ($k_{HbO_2>Hb}$) in RBC lysates

Mouse		WT	AQP1-KO	RhAG-KO	dKO
	P \ α		α	α	α
WT			0.0167	0.0250	0.0125
AQP1-KO	*P*	0.217		0.0500	0.00833
RhAG-KO	*P*	0.282	0.868		0.0100
dKO	*P*	**8.08×10^{-3}**	**4.25×10^{-4}**	**6.31×10^{-4}**	

References

Al-Samir S, Kyriazi D, Yool AJ, Moser I, Kyriazi K, Gros G, Tsiavaliaris G & Endeward V (2025). Aquaporin-1 acts as an O_2 channel. The permeability of human and mouse red cell membranes for oxygen. *Am J Physiol Cell Physiol*; DOI: 10.1152/ajpcell.00858.2024.

Aronson PS, Boron WF & Boulpaep E (2017). Transport of solutes and water. In *Medical Physiology: A Cellular and Molecular Approach*, 3rd Edition., ed. Boron WF & Boulpaep EL, pp. 102–141. Saunders Elsevier, Philadelphia, PA.

Blank M & Roughton FJW (1960). The permeability of monolayers to carbon dioxide. *Trans Faraday Soc* **56,** 1832–1841.

Boron WF (2010). Sharpey-Schafer lecture: Gas channels. *Exp Physiol* **95,** 1107–1130.

Brahm J (1977). Temperature-dependent changes of chloride transport kinetics in human red cells. *Journal of General Physiology* **70,** 283–306.

Cabantchik ZI & Rothstein A (1974). Membrane proteins related to anion permeability of human red blood cells. I. Localization of disulfonic stilbene binding sites in proteins involved in permeation. *J Membr Biol* **15,** 207–226.

Chow EI, Crandall ED & Forster RE (1976). Kinetics of bicarbonate-chloride exchange across the human red blood cell membrane. *J Gen Physiol* **68,** 633–652.

Coin JT & Olson JS (1979). The rate of oxygen uptake by human red blood cells. *J Biol Chem* **254,** 1178–1190.

Cooper GJ & Boron WF (1998). Effect of pCMBS on CO_2 permeability of *Xenopus* oocytes expressing aquaporin 1 or its C189S mutant. *Am J Physiol* **275,** C1481-1486.

Cooper GJ, Occhipinti R & Boron WF (2015). CrossTalk proposal: Physiological CO_2 exchange can depend on membrane channels. *J Physiol*; DOI: 10.1113/JP270059.

Deonikar P, Abu-Soud HM & Kavdia M (2014). Computational analysis of nitric oxide biotransport to red blood cell in the presence of free hemoglobin and NO donor. *Microvasc Res* **95,** 15–25.

Deonikar P & Kavdia M (2013). Contribution of membrane permeability and unstirred layer diffusion to nitric oxide-red blood cell interaction. *J Theor Biol* **317,** 321–330.

Endeward V (2012). The rate of the deoxygenation reaction limits myoglobin- and hemoglobin-facilitated O_2 diffusion in cells. *J Appl Physiol* **112,** 1466–1473.

Endeward V, Cartron J-P, Ripoche P & Gros G (2008). RhAG protein of the Rhesus complex is a CO_2 channel in the human red cell membrane. *FASEB J* **22,** 64–73.

Endeward V, Musa-Aziz R, Cooper GJ, Chen L-M, Pelletier MF, Virkki LV, Supuran CT, King LS, Boron WF & Gros G (2006). Evidence that aquaporin 1 is a major pathway for CO_2 transport across the human erythrocyte membrane. *FASEB J* **20,** 1974–1981.

Fick A (1855*a*). V. On liquid diffusion. *Lond Edinb Dubl Phil Mag* **10,** 30–39.

Fick A (1855*b*). Ueber Diffusion. *Ann Phys* **170,** 59–86.

Forster RE (1964). Rate of gas uptake by red cells. In *Handbook of Physiology*, pp. 827–837. American Physiological Society.

Gershfeld NL & Murayama M (1988). Thermal instability of red blood cell membrane bilayers: temperature dependence of hemolysis. *J Membr Biol* **101,** 67–72.

Geyer RR, Musa-Aziz R, Enkavi G, Mahinthichaichan P, Tajkhorshid E & Boron WF (2013*a*). Movement of NH_3 through the human urea transporter B: a new gas channel. *Am J Physiol Renal Physiol* **304,** F1447-1457.

Geyer RR, Musa-Aziz R, Qin X & Boron WF (2013*b*). Relative CO_2/NH_3 selectivities of mammalian aquaporins 0-9. *Am J Physiol, Cell Physiol* **304,** C985-994.

Geyer RR, Parker MD, Toye AM, Boron WF & Musa-Aziz R (2013*c*). Relative CO_2/NH_3 permeabilities of human RhAG, RhBG and RhCG. *J Membr Biol* **246,** 915–926.

Golde WT, Gollobin P & Rodriguez LL (2005). A rapid, simple, and humane method for submandibular bleeding of mice using a lancet. *Lab Anim (NY)* **34,** 39–43.

Goossens D, Trinh-Trang-Tan M-M, Debbia M, Ripoche P, Vilela-Lamego C, Louache F, Vainchenker W, Colin Y & Cartron J-P (2010). Generation and characterisation of Rhd and Rhag null mice. *Br J Haematol* **148,** 161–172.

Graham T (1829). Notice of the singular inflation of a bladder. *Quart J Sci* **II,** 88–89.

Graham T (1833). XXVII. On the law of the diffusion of gases. *Lond Edinb Dubl Phil Mag* **2,** 175–190.

Gutknecht J, Bisson MA & Tosteson FC (1977). Diffusion of carbon dioxide through lipid bilayer membranes: effects of carbonic anhydrase, bicarbonate, and unstirred layers. *J Gen Physiol* **69,** 779–794.

Hartridge H & Roughton FJ (1927). The rate of distribution of dissolved gases between the red blood corpuscle and its fluid environment: Part I. Preliminary experiments on the rate of uptake of oxygen and carbon monoxide by sheep's corpuscles. *J Physiol (Lond)* **62,** 232–242.

Henry W (1803). Experiments on the quantity of gases absorbed by water, at different temperatures, and under different pressures. *Phil Trans R Soc B* **93,** 29–276.

Holland RA, Shibata H, Scheid P & Piiper J (1985). Kinetics of O_2 uptake and release by red cells in stopped-flow apparatus: effects of unstirred layer. *Respir Physiol* **59,** 71–91.

Holm S (1979). A simple sequentially rejective multiple test procedure. *Scandinavian Journal of Statistics* **6,** 65–70.

Huffman DE, Occhipinti R, Somersalo E, Calvetti D & Boron WF (2025). A graphical user interface for "Role of channels in the O_2 permeability of murine red blood cells III. Mathematical modeling." Available at: https://doi.org/10.5281/zenodo.14932553.

Jensen FB, Wang T & Brahm J (2001). Acute and chronic influence of temperature on red blood cell anion exchange. *J Exp Biol* **204,** 39–45.

Kelmenson P (2016). There is no such thing as a C57BL/6 mouse! *The Jackson Laboratory*. Available at: https://www.jax.org/news-and-insights/jax-blog/2016/june/there-is-no-such-thing-as-a-b6-mouse [Accessed February 29, 2024].

Kimzey SL & Willis JS (1971). Temperature adaptation of active sodium-potassium transport and of passive permeability in erythrocytes of ground squirrels. *J Gen Physiol* **58,** 634–649.

Kreuzer F (1982). Oxygen supply to tissues: the Krogh model and its assumptions. *Experientia* **38,** 1415–1426.

Krogh A (1919). The number and distribution of capillaries in muscles with calculations of the oxygen pressure head necessary for supplying the tissue. *J Physiol (Lond)* **52,** 409–415.

Lowe AG & Walmsley AR (1986). The kinetics of glucose transport in human red blood cells. *Biochim Biophys Acta* **857,** 146–154.

Ma T, Yang B, Gillespie A, Carlson EJ, Epstein CJ & Verkman AS (1998). Severely impaired urinary concentrating ability in transgenic mice lacking aquaporin-1 water channels. *J Biol Chem* **273,** 4296–4299.

Macey RI (1984). Transport of water and urea in red blood cells. *Am J Physiol* **246,** C195-203.

Macey RI & Farmer RE (1970). Inhibition of water and solute permeability in human red cells. *Biochim Biophys Acta* **211,** 104–106.

Michenkova M, Taki S, Blosser MC, Hwang HJ, Kowatz T, Moss FJ, Occhipinti R, Qin X, Sen S, Shinn E, Wang D-K, Zeise B, Zhao P, Malmstadt N, Vahedi-Faridi A, Tajkhorshid E & Boron WF (2021). Carbon dioxide transport across membranes. *Interface Focus* **11,** 2.

Mitchell JK (1830). On the penetrativeness of fluids. *Am J Med Sci* **7,** 36–67.

Mitchell JK (1831*a*). On the penetrativeness of fluids. *J Roy Inst Gr Brit* **IV,** 101–118.

Mitchell JK (1831*b*). On the penetrativeness of fluids. *J Roy Inst Gr Brit* **V,** 307–321.

Mitchell JK (1833). Art. IX. On the penetration of gases. *Am J Med Sci* **13,** 100–112.

Moll W (1968). The influence of hemoglobin diffusion on oxygen uptake and release by red cells. *Respir Physiol* **6,** 1–15.

Moriyama A, Katagiri N, Nishimura S, Takahashi N & Kakeya H (2015). *In vivo* linking of membrane lipids and the anion transporter band 3 with thiourea-modified amphiphilic lipid probes. *Sci Rep* **5,** 17427.

Moss FJ, Zhao, Pan, Salameh Ahlam I., Taki, Sara, Wass, Amanda B., Huffman DE, Meyerson, Howard J., Occhipinti, Rossana, & Boron, Walter F. (2025). Role of channels in the O_2 permeability of murine red blood cells II. Morphological and proteomic studies. *Journal of Physiology*.

Musa-Aziz R, Chen L & Boron WF (2007*a*). The CO_2/NH_3 Selectivity of AQP1, AQP4, and AQP5 and How It is Affected by DIDS. *J Am Soc Nephrol* **18,** P6A.

Musa-Aziz R, Chen L-M & Boron WF (2007*b*). Differential effects of DIDS on the CO_2 vs NH_3 permeability of AQP1, AmtB, and RhAG. *Proceedings of the International Congress of Nephrology, Rio de Janeiro, Brazil*.

Musa-Aziz R, Chen L-M, Pelletier MF & Boron WF (2009). Relative CO_2/NH_3 selectivities of AQP1, AQP4, AQP5, AmtB, and RhAG. *Proc Natl Acad Sci USA* **106,** 5406–5411.

Musa-Aziz R, Geyer RR, Moss FJ & Boron WF (2025). Mechanism of CO_2 and NH_3 transport through human aquaporin 1: Evidence for parallel CO_2 pathways. *bioRxiv*; DOI: 10.1101/2025.02.28.640247.

Nakhoul NL, Davis BA, Romero MF & Boron WF (1998). Effect of expressing the water channel aquaporin-1 on the CO_2 permeability of *Xenopus* oocytes. *Am J Physiol* **274,** C543-548.

Nakhoul NL & Hamm LL (2004). Non-erythroid Rh glycoproteins: a putative new family of mammalian ammonium transporters. *Pflugers Arch* **447,** 807–812.

Nakhoul NL & Hamm LL (2014). The challenge of determining the role of Rh glycoproteins in transport of NH_3 and NH_4^+. *Wiley Interdisciplinary Reviews: Membrane Transport and Signaling* **3,** 53–61.

Nakhoul NL, Hering-Smith KS, Abdulnour-Nakhoul SM & Hamm LL (2001). Transport of NH_3/NH_4^+ in oocytes expressing aquaporin-1. *Am J Physiol Renal Physiol* **281,** F255-263.

Occhipinti R, Zhao P, Huffman DE, Moss FJ & Boron WF (2025). Role of channels in the O_2 permeability of murine red blood cells. III. Mathematical modeling and simulations. *J Physiol*.

Overton E (1895). Über die osmotischen Eigenschaften der Zelle in ihrer Bedeutung für die Toxikologie und Pharmacologie. *Z Phys Chem* **22,** 189–209.

Overton E (1899). Ueber die allgemeinen osmotischen Eigenschaften der Zelle, ihre vermutlichen Ursachen und ihre Bedeutung für die Physiologie. *Vierteljahrsschr Naturforsch Ges Zürich* **44,** 88–135.

Parasuraman S, Raveendran R & Kesavan R (2010). Blood sample collection in small laboratory animals. *J Pharmacol Pharmacother* **1,** 87–93.

Ponder E (1948). *Hemolysis and Related Phenomena*. New York : Grune & Stratton. Available at: http://hdl.handle.net/2027/wu.89047892849.

Preston GM & Agre P (1991). Isolation of the cDNA for erythrocyte integral membrane protein of 28 kilodaltons: member of an ancient channel family. *Proc Natl Acad Sci USA* **88,** 11110–11114.

Preston GM, Carroll TP, Guggino WB & Agre P (1992). Appearance of water channels in *Xenopus* oocytes expressing red cell CHIP28 protein. *Science* **256,** 385–387.

Preston GM, Jung JS, Guggino WB & Agre P (1993). The mercury-sensitive residue at cysteine 189 in the CHIP28 water channel. *J Biol Chem* **268,** 17–20.

Rothstein A, Knauf PA, Cabantchik ZI & Balshin M (1973). The location and chemical nature of drug 'targets' within the human erythrocyte membrane. In *Drugs and Transport Processes:*

A Symposium, ed. Callingham BA, pp. 53–72. Macmillan Education UK, London. Available at: https://doi.org/10.1007/978-1-349-02273-1_4.

Roughton FJW (1932). Diffusion and chemical reaction velocity as joint factors in determining the rate of uptake of oxygen and carbon monoxide by the red blood corpuscle. *Proc R Soc Lond B* **111,** 1–36.

Simon SA & Gutknecht J (1980). Solubility of carbon dioxide in lipid bilayer membranes and organic solvents. *Biochim Biophys Acta* **596,** 352–358.

Somersalo E, Occhipinti R, Boron WF & Calvetti D (2012). A reaction-diffusion model of CO_2 influx into an oocyte. *J Theor Biol* **309,** 185–203.

Stannett V (1978). The transport of gases in synthetic polymeric membranes—an historic perspective. *J Membrane Sci* **3,** 97–115.

Uehlein N, Lovisolo C, Siefritz F & Kaldenhoff R (2003). The tobacco aquaporin NtAQP1 is a membrane CO_2 pore with physiological functions. *Nature* **425,** 734–737.

Uehlein N, Otto B, Eilingsfeld A, Itel F, Meier W & Kaldenhoff R (2012*a*). Gas-tight triblock-copolymer membranes are converted to CO_2 permeable by insertion of plant aquaporins. *Sci Rep* **2,** 538.

Uehlein N, Otto B, Hanson DT, Fischer M, McDowell N & Kaldenhoff R (2008). Function of Nicotiana tabacum aquaporins as chloroplast gas pores challenges the concept of membrane CO_2 permeability. *Plant Cell* **20,** 648–657.

Uehlein N, Sperling H, Heckwolf M & Kaldenhoff R (2012*b*). The Arabidopsis aquaporin PIP1;2 rules cellular CO_2 uptake. *Plant Cell Environ* **35,** 1077–1083.

Vallese F, Kim K, Yen LY, Johnston JD, Noble AJ, Calì T & Clarke OB (2022). Architecture of the human erythrocyte ankyrin-1 complex. *Nat Struct Mol Biol* **29,** 706–718.

Vandegriff KD & Olson JS (1984*a*). A quantitative description in three dimensions of oxygen uptake by human red blood cells. *Biophys J* **45,** 825–835.

Vandegriff KD & Olson JS (1984*b*). The kinetics of O_2 release by human red blood cells in the presence of external sodium dithionite. *J Biol Chem* **259,** 12609–12618.

Vansteveninck J, Weed RI & Rothstein A (1965). Localization of Erythrocyte Membrane Sulfhydryl Groups Essential for Glucose Transport. *Journal of General Physiology* **48,** 617–632.

Waisbren SJ, Geibel JP, Modlin IM & Boron WF (1994). Unusual permeability properties of gastric gland cells. *Nature* **368,** 332–335.

Wang C, Hu H, Qin X, Zeise B, Xu D, Rappel W-J, Boron WF & Schroeder JI (2016). Reconstitution of CO_2 regulation of SLAC1 anion channel and function of CO_2-permeable PIP2;1 aquaporin as carbonic anhydrase 4 interactor. *Plant Cell* **28,** 568–582.

Wang D-K, Moss FJ & Boron WF (2025). Synergistic roles of Aquaporin 5 and Intra- and Extracellular Carbonic Anhydrases In promoting CO_2 Diffusion across the *Xenopus* Oocyte Plasma Membrane. *bioRxiv*; DOI: 10.1101/2025.04.08.647833.

Williams JB & Kutchai H (1986). Use of a membrane-bound fluorophore to characterize diffusion boundary layers around human erythrocytes. *Biophys J* **49,** 453–458.

Wroblewski S (1879). On the nature of the absorption of gases. *Nature* **21,** 190–192.

Zhao P & Boron WF (2019). Effect of aging on oxygen permeability of wild type (WT) and AQP1-RhAG double knockout (dKO) mouse red blood cells. *The FASEB Journal* **33,** 823.4-823.4.

Zhao P & Boron WF (2023). Oxygen-offloading rate from mouse red blood cells of genetically diverse strains. *Physiology* **38,** 5735109.

Zhao P, Geyer RR & Boron WF (2017). A novel stopped-flow assay for quantitating carbonic-anhydrase activity and assessing red-blood-cell hemolysis. *Front Physiol* **8,** 169.

Zhao P, Geyer RR, Salameh AI, Wass AB, Taki S, Huffman, Dale E, Meyerson HJ, Gros G, Occhipinti R, Moss FJ & Boron WF (2020). Role of channels in the oxygen permeability of red blood cells. *bioRxiv*; DOI: 10.1101/2020.08.28.265066.

Zhao P, Taki S, Babcock GT, Radford TS, Moss FJ, Occhipinti R & Boron WF (2021). AQP1 and RhAG proteins play roles on oxygen offloading from murine red blood cells during aging. *FASEB J*; DOI: https://doi.org/10.1096/fasebj.2021.35.S1.04289.

Zwiazek JJ, Xu H, Tan X, Navarro-Ródenas A & Morte A (2017). Significance of oxygen transport through aquaporins. *Sci Rep* **7,** 40411.

Additional Information

Data availability statement

The data that support the findings of this study are available from the corresponding authors, W.F.B., upon reasonable request.

Competing interests

The authors declare that they have no competing interests.

Author contributions

P.Z., F.J.M., R.O., R.R.G., & W.F.B. designed the study; P.Z. performed the majority of the stopped-flow experiments, and the automated hematology and analyzed the data; R.R.G. performed preliminary stopped-flow experiments; P.Z. also made the blood smears analyzed by H.J.M.; P.Z. coordinated the microvideography experiments of red blood cells treated with inhibitors; F.J.M. performed mass spectrometry and flow cytometry experiments and analyzed the data. R.O. performed the mathematical modeling and simulations and programming; D.E.H. created a program to do data analysis on raw HbSat data to produce raw-k_{HbO_2} values; P.Z. and F.J.M. performed statistical analysis; P.Z., F.J.M., R.O., & W.F.B. worked on flow-chart and artist optimized the finalized version. P.Z. prepared figures; P.Z., F.J.M., R.O., & W.F.B. wrote the manuscript.

Supporting Information

Supporting Files

Supporting file 1: 1--Suppl_Tables_SF_Statistics_For_Table_4_&_Table_5.xlsx

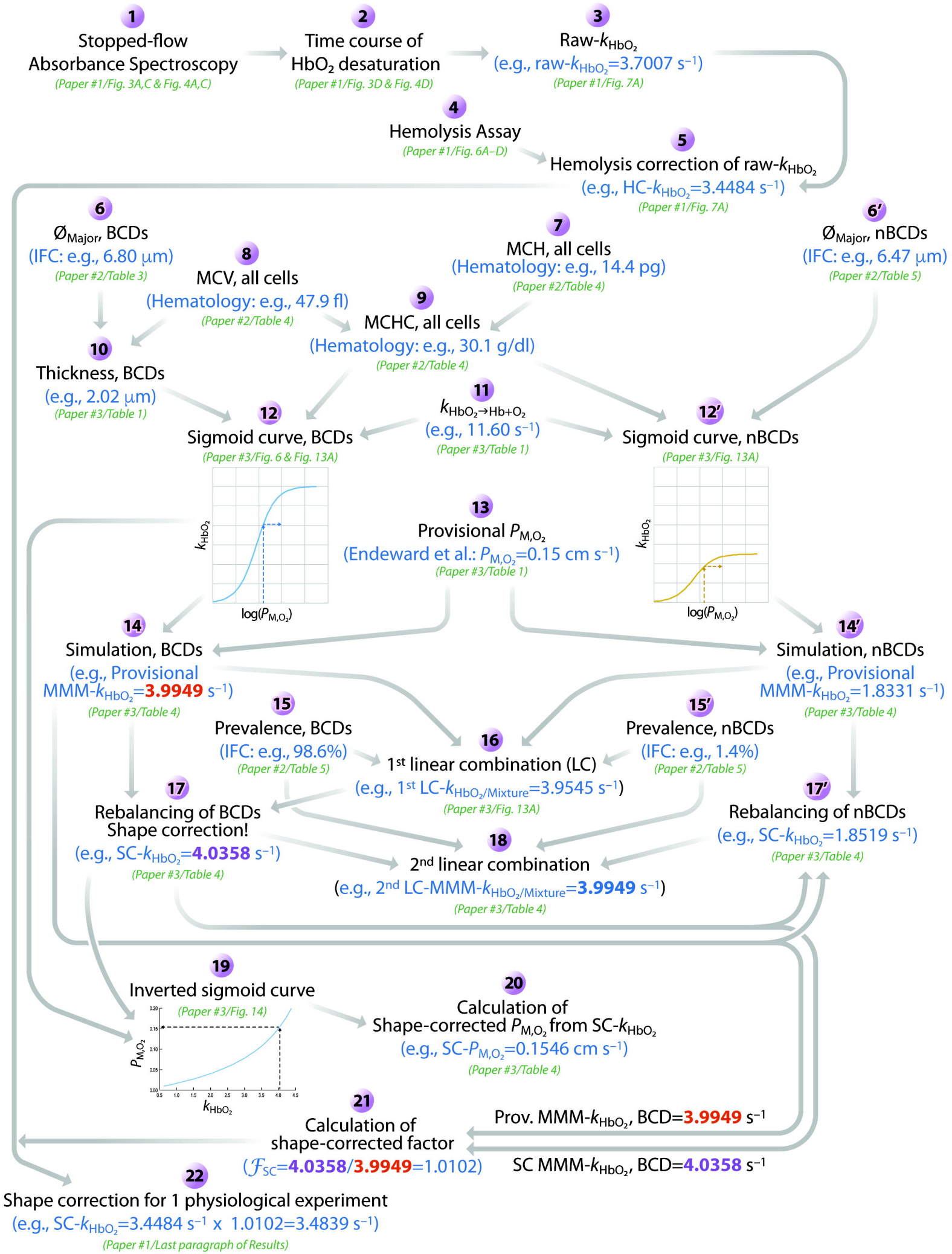
1
Stopped-flow Absorbance Spectroscopy
(Paper #1/Fig. 3A,C & Fig. 4A,C)
2
Time course of HbO_2 desaturation
(Paper #1/Fig. 3D & Fig. 4D)
3
Raw-k_{HbO_2}
(e.g., raw-k_{HbO_2}=3.7007 s^{-1})
(Paper #1/Fig. 7A)
4
Hemolysis Assay
(Paper #1/Fig. 6A–D)
5
Hemolysis correction of raw-k_{HbO_2}
(e.g., HC-k_{HbO_2}=3.4484 s^{-1})
(Paper #1/Fig. 7A)
6
$Ø_{Major}$, BCDs
(IFC: e.g., 6.80 μm)
(Paper #2/Table 3)
6′
$Ø_{Major}$, nBCDs
(IFC: e.g., 6.47 μm)
(Paper #2/Table 5)
7
MCH, all cells
(Hematology: e.g., 14.4 pg)
(Paper #2/Table 4)
8
MCV, all cells
(Hematology: e.g., 47.9 fl)
(Paper #2/Table 4)
9
MCHC, all cells
(Hematology: e.g., 30.1 g/dl)
(Paper #2/Table 4)
10
Thickness, BCDs
(e.g., 2.02 μm)
(Paper #3/Table 1)
11
$k_{HbO_2 \rightarrow Hb+O_2}$
(e.g., 11.60 s^{-1})
(Paper #3/Table 1)
12
Sigmoid curve, BCDs
(Paper #3/Fig. 6 & Fig. 13A)
12′
Sigmoid curve, nBCDs
(Paper #3/Fig. 13A)
k_{HbO_2}
$\log(P_{M,O_2})$
13
Provisional P_{M,O_2}
(Endeward et al.: P_{M,O_2}=0.15 cm s^{-1})
(Paper #3/Table 1)
14
Simulation, BCDs
(e.g., Provisional MMM-k_{HbO_2}=3.9949 s^{-1})
(Paper #3/Table 4)
14′
Simulation, nBCDs
(e.g., Provisional MMM-k_{HbO_2}=1.8331 s^{-1})
(Paper #3/Table 4)
15
Prevalence, BCDs
(IFC: e.g., 98.6%)
(Paper #2/Table 5)
15′
Prevalence, nBCDs
(IFC: e.g., 1.4%)
(Paper #2/Table 5)
16
1st linear combination (LC)
(e.g., 1st LC-$k_{HbO_2/Mixture}$=3.9545 s^{-1})
(Paper #3/Fig. 13A)
17
Rebalancing of BCDs
Shape correction!
(e.g., SC-k_{HbO_2}=4.0358 s^{-1})
(Paper #3/Table 4)
17′
Rebalancing of nBCDs
(e.g., SC-k_{HbO_2}=1.8519 s^{-1})
(Paper #3/Table 4)
18
2nd linear combination
(e.g., 2nd LC-MMM-$k_{HbO_2/Mixture}$=3.9949 s^{-1})
(Paper #3/Table 4)
19
Inverted sigmoid curve
(Paper #3/Fig. 14)
P_{M,O_2}
k_{HbO_2}
20
Calculation of Shape-corrected P_{M,O_2} from SC-k_{HbO_2}
(e.g., SC-P_{M,O_2}=0.1546 cm s^{-1})
(Paper #3/Table 4)
21
Calculation of shape-corrected factor
($\mathcal{F}_{SC}$=4.0358/3.9949=1.0102)
Prov. MMM-k_{HbO_2}, BCD=3.9949 s^{-1}
SC MMM-k_{HbO_2}, BCD=4.0358 s^{-1}
22
Shape correction for 1 physiological experiment
(e.g., SC-k_{HbO_2}=3.4484 s^{-1} x 1.0102=3.4839 s^{-1})
(Paper #1/Last paragraph of Results)

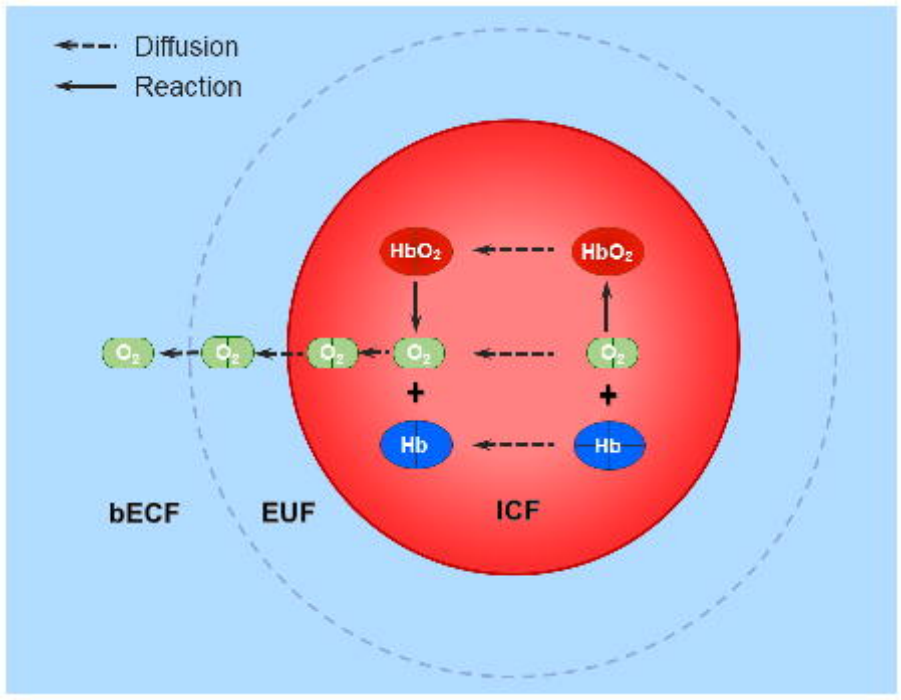
Diffusion
Reaction
HbO2
HbO2
O2
O2
O2
O2
O2
+
+
Hb
Hb
bECF
EUF
ICF

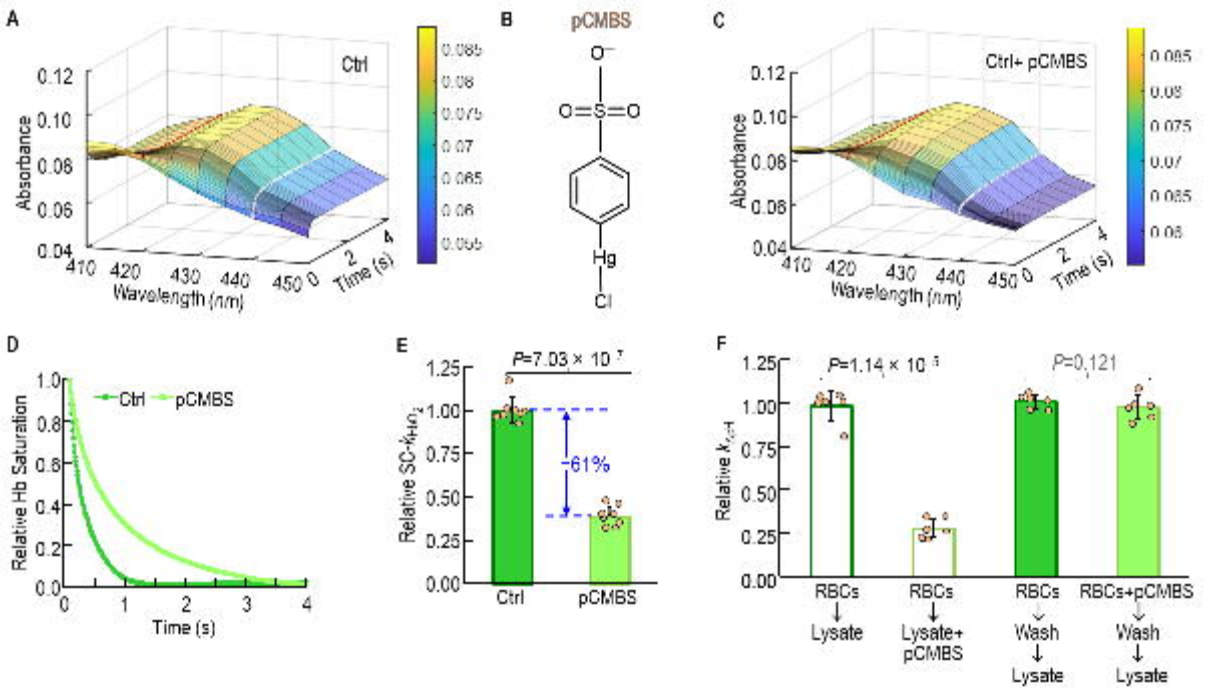
A
Ctrl
Absorbance
Wavelength (nm)
Time (s)
B
pCMBS
O⁻
O=S=O
Hg
Cl
C
Ctrl+ pCMBS
Absorbance
Wavelength (nm)
Time (s)
D
Ctrl
pCMBS
Relative Hb Saturation
Time (s)
E
P=7.03 × 10⁻⁷
61%
Relative SC-kHb
Ctrl
pCMBS
F
P=1.14 × 10⁻⁵
P=0.121
Relative kcat
RBCs
Lysate
RBCs
Lysate+ pCMBS
RBCs
Wash
Lysate
RBCs+pCMBS
Wash
Lysate

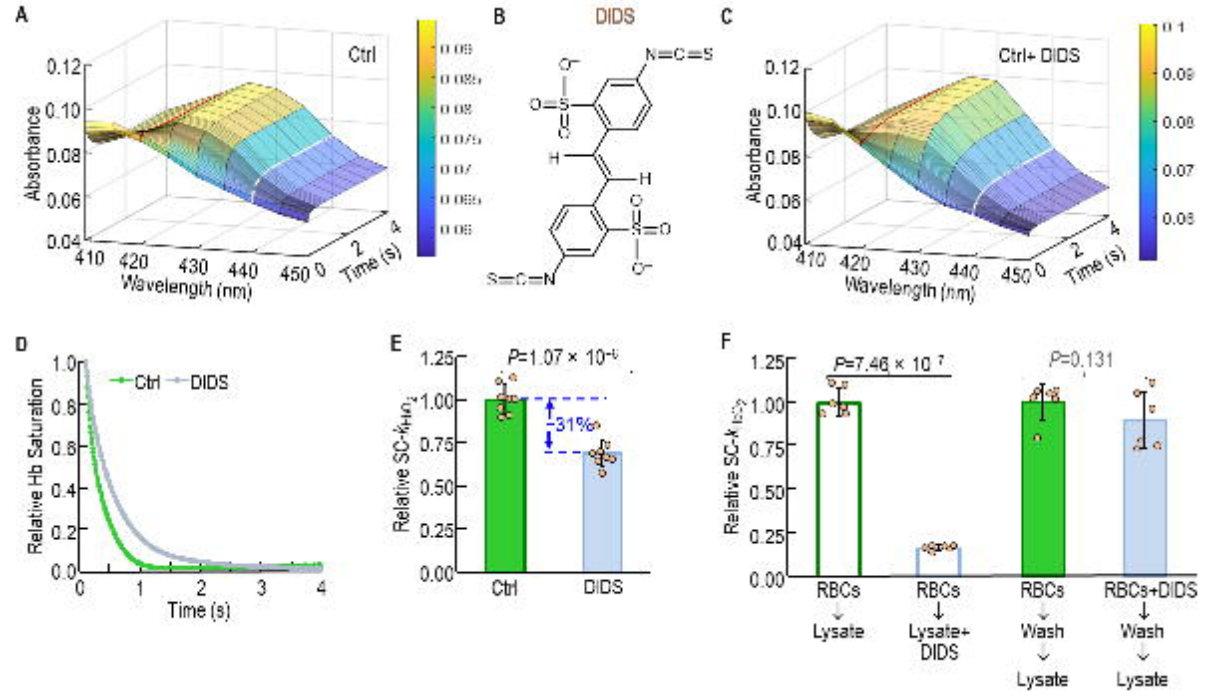
A
Ctrl
Absorbance
Wavelength (nm)
Time (s)
B
DIDS
C
Ctrl+ DIDS
D
Ctrl
DIDS
Relative Hb Saturation
Time (s)
E
P=1.07 × 10⁻⁶
31%
Relative SC-k
Ctrl
DIDS
F
P=7.46 × 10⁻⁷
P=0.131
Relative SC-k
RBCs
Lysate
RBCs
Lysate+ DIDS
RBCs
Wash
Lysate
RBCs+DIDS
Wash
Lysate

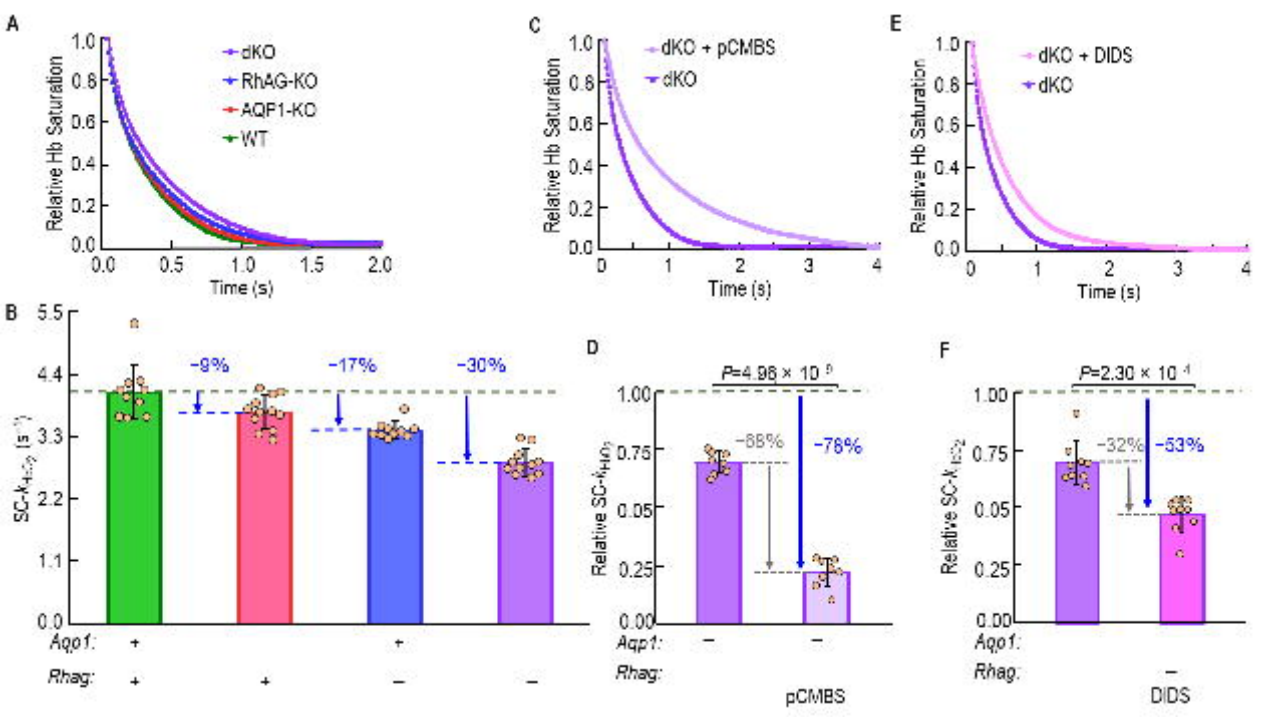
A
Relative Hb Saturation
Time (s)
dKO
RhAG-KO
AQP1-KO
WT
C
dKO + pCMBS
dKO
E
dKO + DIDS
dKO
B
−9%
−17%
−30%
Aqp1:
Rhag:
D
P=4.96 × 10 5
−68%
−78%
Relative SC-kH2O
pCMBS
F
P=2.30 × 10 4
−32%
−53%
DIDS

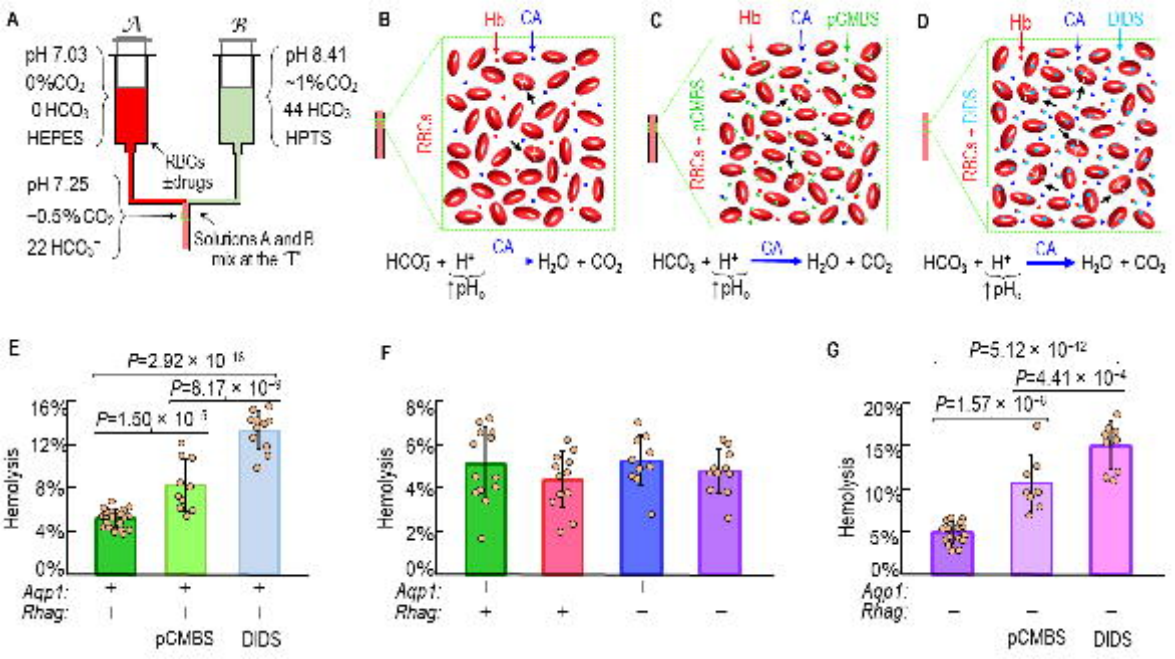
A
A
B
pH 7.03
0%CO2
0 HCO3
HEPES
pH 8.41
~1%CO2
44 HCO3
HPTS
RBCs
±drugs
pH 7.25
~0.5%CO2
22 HCO3-
Solutions A and B
mix at the 'T'
B
Hb
CA
RBCs
HCO3 + H+ CA H2O + CO2
↑pHo
C
Hb
CA
pCMBS
RBCs + pCMBS
HCO3 + H+ CA H2O + CO2
↑pHo
D
Hb
CA
DIDS
RBCs + DIDS
HCO3 + H+ CA H2O + CO2
↑pHi
E
P=2.92 × 10-16
P=8.17 × 10-9
P=1.50 × 10-3
Hemolysis
16%
12%
8%
4%
0%
Aqp1:
Rhag:
pCMBS
DIDS
F
Hemolysis
8%
6%
4%
2%
0%
Aqp1:
Rhag:
G
P=5.12 × 10-12
P=4.41 × 10-4
P=1.57 × 10-6
Hemolysis
20%
15%
10%
5%
0%
Aqp1:
Rhag:
pCMBS
DIDS

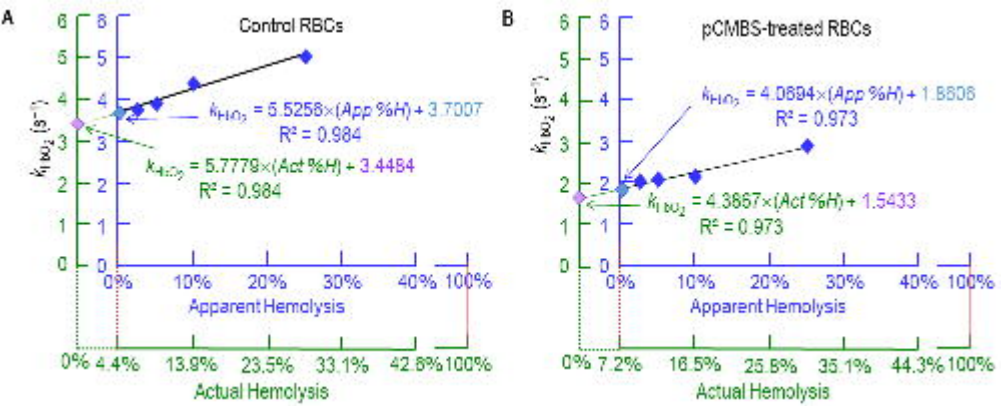
A
Control RBCs
k_{HbO_2} [s⁻¹]
k_{HbO_2} = 5.5258×(App %H) + 3.7007
R² = 0.984
k_{HbO_2} = 5.7779×(Act %H) + 3.4484
R² = 0.984
0% 10% 20% 30% 40% 100%
Apparent Hemolysis
0% 4.4% 13.9% 23.5% 33.1% 42.8% 100%
Actual Hemolysis
B
pCMBS-treated RBCs
k_{HbO_2} [s⁻¹]
k_{HbO_2} = 4.0694×(App %H) + 1.8806
R² = 0.973
k_{HbO_2} = 4.3867×(Act %H) + 1.5433
R² = 0.973
0% 10% 20% 30% 40% 100%
Apparent Hemolysis
0% 7.2% 16.5% 25.8% 35.1% 44.3% 100%
Actual Hemolysis

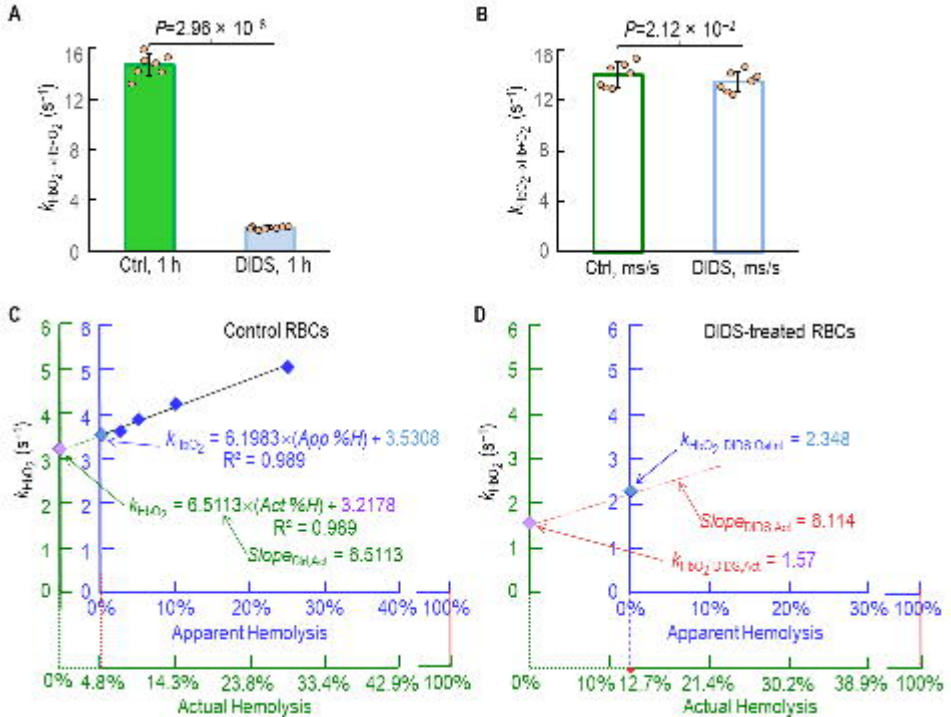
A
P=2.96 × 10⁻⁸
Ctrl, 1 h
DIDS, 1 h
B
P=2.12 × 10⁻²
Ctrl, ms/s
DIDS, ms/s
C
Control RBCs
k_HbO2 = 6.1983×(App %H) + 3.5308
R² = 0.989
k_HbO2 = 6.5113×(Act %H) + 3.2178
R² = 0.969
Slope_Ctrl,Act = 6.5113
Apparent Hemolysis
Actual Hemolysis
D
DIDS-treated RBCs
k_HbO2 DIDS,App = 2.348
Slope_DIDS,Act = 8.114
k_HbO2 DIDS,Act = 1.57
Apparent Hemolysis
Actual Hemolysis

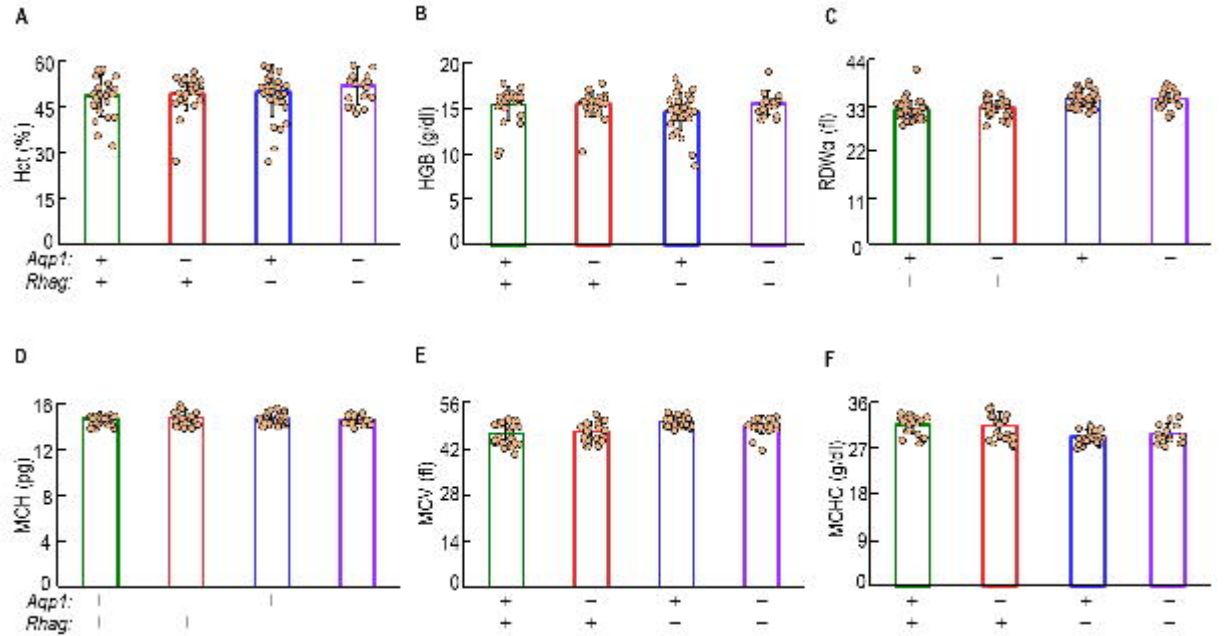
A
Hct (%)
60
45
30
15
0
Aqp1:
Rhag:
B
HGB (g/dl)
20
15
10
5
0
C
RDWa (fl)
44
33
22
11
0
D
MCH (pg)
16
12
8
4
0
Aqp1:
Rhag:
E
MCV (fl)
56
42
28
14
0
F
MCHC (g/dl)
36
27
18
9
0

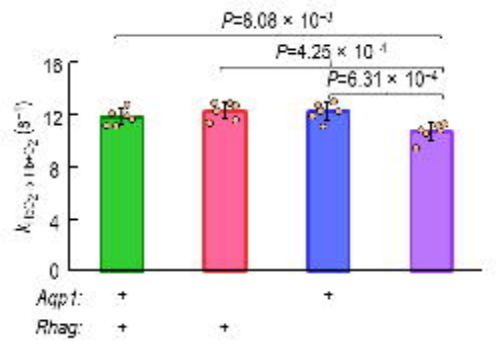
P=8.08 × 10⁻⁴
P=4.25 × 10⁻⁴
P=6.31 × 10⁻⁴
18
12
8
4
0
Aqp1:
Rhag:

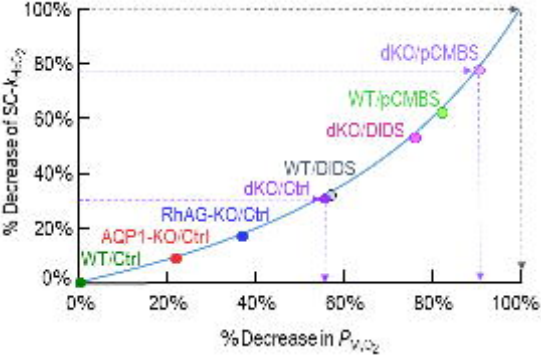
100%
80%
60%
40%
20%
0%
% Decrease of SC-k_{H_2O}
dKC/pCMBS
WT/pCMBS
dKC/DIDS
WT/DIDS
dKC/Ctrl
RhAG-KO/Ctrl
AQP1-KO/Ctrl
WT/Ctrl
0%
20%
40%
60%
80%
100%
% Decrease in P_{H_2O}